Experimental Investigation of the Prefilming Airblast Atomization Process under Periodically Oscillating Airflows

Zur Erlangung des akademischen Grades eines

Doktors der Ingenieurwissenschaften (Dr.-Ing.)

von der KIT-Fakultät für Chemieingenieurwesen und Verfahrenstechnik des
Karlsruher Instituts für Technologie (KIT)

genehmigte

Dissertation

von

Dipl.-Ing. Thomas Christou

aus Athen (Griechenland)

Dedicated to my family and friends

Acknowledgements

Abstract

The inlet air velocity is prone to perturbations in the context of thermoacoustic instabilities that frequently occur in the combustion chamber of low-emission jet engines. These thermoacoustic instabilities develop when the heat released by the combustion process is unstable, and the pressure waves created in the chamber are connected to the inlet air velocity, further enhancing the instability of the heat release. Prefilming airblast atomizers are used in most contemporary jet engines to disintegrate the liquid fuel into a spray of droplets. The atomization process is affected by these uncontrolled instabilities of the inlet air velocity since the operating concept of this type of atomizer is based on a high relative velocity between the air and the liquid fuel. The spray quality has a direct impact on critical operational parameters such as the local and temporal air-to-fuel ratio in the combustor, flame stability limits, combustion efficiency, as well as NO_x emission levels. As a result, anticipating the performance of the atomization process under unstable airflow conditions is still to this day necessary.

A test setup and a model prefilmer were designed for an extended investigation of the spray in a two-dimensional flow in order to evaluate the response of the airblast atomization process under unstable flow conditions. The spray was thoroughly investigated under various conditions and the influence of the oscillating airflow on the droplets was quantified. Predictions for flame stability and engine hardware safety may be derived in thermoacoustic models by utilizing the experimental data of the spray response under different frequencies.

Kurzfassung

Die Luftgeschwindigkeit an dem Brennkammereintritt eines Flugzeugtriebwerks ist anfällig für Störungen im Rahmen von thermoakustischen Instabilitäten, die häufig auftreten. Diese thermoakustischen Instabilitäten entstehen, wenn die durch den Verbrennungsprozess freigesetzte Wärme instabil ist und die in der Kammer erzeugten Druckwellen mit der Eintrittsluftgeschwindigkeit verbunden sind, was die Instabilität der Wärmefreisetzung noch verstärkt. In den meisten modernen Flugzeugtriebwerken werden Prefilm-Zerstäuber eingesetzt, um den flüssigen Brennstoff in einen Sprühnebel aus Tröpfchen zu zerstäuben. Der Zerstäubungsprozess wird durch diese unkontrollierten Instabilitäten der Eintrittsluftgeschwindigkeit beeinträchtigt, da das Funktionsprinzip dieses Typs von Zerstäuber auf einer hohen Relativgeschwindigkeit zwischen der Luft und dem flüssigen Brennstoff basiert. Die Zerstäubungsqualität hat einen direkten Einfluss auf kritische Betriebsparameter wie das Luft-Brennstoff-Verhältnis in der Brennkammer, die Flammenstabilitätsgrenzen, die Verbrennungseffizienz sowie die NO_x-Emissionen. Daher ist es auch heutzutage noch notwendig, die Leistung des Zerstäubungsprozesses unter instabilen Luftströmungsbedingungen vorherzusehen.

Für eine erweiterte Untersuchung des Sprays in einer zweidimensionalen Strömung wurden ein Versuchsaufbau und ein Modell-Prefilmer entwickelt und aufgebaut, um das Verhalten des Airblast-Zerstäubungsprozesses unter instabilen Strömungsbedingungen zu ermitteln. Das Spray wurde unter verschiedenen Bedingungen eingehend untersucht und der Einfluss der

oszillierenden Luftströmung auf die Tröpfchen wurde quantifiziert. Aus den experimentellen Daten des Sprayverhaltens bei verschiedenen Frequenzen lassen sich in thermoakustischen Modellen Vorhersagen für die Flammenstabilität und die Sicherheit der Triebwerke ableiten.

Contents

List of Figures

List of Tables

Nomenclature

A	Area	m²
b	Film width	mm
b	Scattered light term	-
c	Constant	
c	Speed of light	m s^{-1}
c	Speed of wave propagation	m s^{-1}
c_D	Drag/Discharge coefficient	-
C_P	Specific heat capacity	J kg^{-1} K^{-1}
D, d	Diameter	μm
D_{10}	Mean Diameter	μm
D_{32}	Sauter Mean Diameter	μm
$D_{63.2\%}$	Diameter constant (Rosin-Rammler model)	μm
d_e	Effective measurement volume diameter	μm
d_f	Beam waist diameter	m
d_L	Laser beam diameter at origin	m
$\Delta p/p$	Pressure drop	%
E	Acoustic energy	J
E	Bridge voltage	V

E	Expansion factor	-
$\vec{e}$	Laser beam	
F	Acoustic flux	$J\ s^{-1}$
f	Focal length	m
f	Frequency	Hz
f, g	Travelling waves	
F_B	Buoyancy force	N
f_D	Doppler frequency	Hz
F_D	Drag force	N
F_P	Pressure force	N
f_{shift}	Shift frequency	MHz
F_W	Weight force	N
F_σ	Surface tension force	N
g	Gravitational acceleration	$m\ s^{-1}$
h	Height	m
k	Wave number	m^{-1}
L	Breakup length	mm
L_S	Width of slit aperture	μm
$\dot{m}$	Mass flow rate	$kg\ s^{-1}$
$\dot{m}''$	Mass flux	$kg\ m^{-2}\ s^{-1}$

m	Mass	kg
N	Number	-
n	Refractive index	-
N	Rotational speed	RPM
N_f	Number of fringes	-
n_{rel}	Relative refraction index	-
Oh	Ohnesorge number	-
p	Pressure	Pa, bar
p_i	Inner pressure	Pa
p_o	Outer pressure	Pa
p_σ	Surface tension pressure	Pa
$\dot{Q}$	Heat release	$J\ s^{-1}$
Q	Liquid volume fraction (Rosin-Rammler model)	-
q	Spread parameter (Rosin-Rammler model)	-
R	Radius	m
R	Specific gas constant	$J\ kg^{-1}\ K^{-1}$
Re	Reynolds number	-
R_V	Bridge resistance	Ω
sw	Statistical weight	-
t	Film thickness	μm

T	Period	s
T	Temperature	°C, K
t	Time	s, ms, µs
T_F	Fluid temperature	°C
T_S	Wire temperature	°C
u, v	Velocity	m s^{-1}
u_R	Relative velocity	m s^{-1}
V	Volume	m^3
$\dot{V}/b$	Film load	mm^2 s^{-1}
w	Width	m
We	Weber number	-
x	Distance	m
X, Y, Z	Coordinates	mm

Greek

γ	Incidence beam angle	°
γ	Particle trajectory angle	°
γ	Specific heat capacity ratio	-
δ	Reference beam phase difference	rad
Δ( )	Difference	

δ_f	Fringe spacing	m
δ_x	Measurements volume length	m
$\delta_{x,e}$	Boundary layer thickness at atomization edge	μm
δ_y	Measurements volume width	m
δ_z	Measurements volume height	m
θ	Intersection angle	°
λ	Wavelength	m
μ	Dynamic viscosity	Pa s
ρ	Density	kg m^{-3}
σ	Surface tension	N m^{-1}
φ	Phase angle	°, rad
Φ	Phase	°
φ	Scattering angle	°
ψ	Elevation angle	°
ω	Angular frequency	rad s^{-1}

Acronyms

ADC	Analog to Digital Converter
AFR	Air-to-Fuel Ratio
ALR	Air-to-Liquid Ratio

BNC	Bayonet Neill-Concelman
CAEP	Committee on Aviation Environmental Protection
CO	Carbon Monoxide
CO_2	Carbon Dioxide
$CO_{2,eq}$	Carbon Dioxide equivalents
CTA	Constant Temperature Anemometry
DLN	Dry Low NO_x
DOF	Depth of Field
DPSS	Diode-Pumped Solid-State
FFT	Fast Fourier Transform
FTF	Flame Transfer Function
GALR	Global Air-to-Liquid Ratio
LDA	Laser Doppler Anemometry
LDI	Lean Direct Injection
LPP	Lean Premixed Prevaporized
NACA	National Advisory Committee for Aeronautics
Nd: YAG	Neodymium-doped Yttrium Aluminum Garnet
NO	Nitric Oxide
NO_2	Nitrogen Dioxide
NO_x	Nitrogen Oxides

P&ID	Piping and Instrumentation Diagram
PDA	Phase Doppler Anemometry
PIV	Particle Image Velocimetry
PTU	Programmable Timing Unit
RQL	Rich-Quench-Lean
sCMOS	Scientific Complementary Metal-Oxide-Semiconductor
SMD	Sauter Mean Diameter
UHC	Unburned Hydrocarbons

Subscripts

$A_\perp$	Perpendicular
A_0	Initial condition, Reference
A_A	Air
A_b	Laser beam
A_{crit}	Critical
A_d	Droplet
A_g	Gas
A_L	Liquid
A_M	Medium
A_{max}	Maximum

A_p Particle

A_r Receiving optic

A_{ref} Reference

Superscripts

$\overline{A}$ Average

A' Perturbation

$\dot{A}$ Rate

$\hat{A}$ Real component

1 Introduction

1.1 Aviation and Emissions

The rising aviation traffic volumes over the last few decades [1], as well as the increased public environmental awareness, created a market for a substantial decrease in harmful emissions from jet engine combustors [2]. Innovations in the technological field and emission regulations imposed have resulted in a gradual improvement of the combustion processes in the context of jet engine operation [3,4].

The impact of the aviation industry on the environment is rather small compared to the rest of the human-induced risks enhancing the climate crisis [2]. The aviation sector accounts for just 1.9% of the global anthropogenic greenhouse gas emissions, measured in carbon dioxide equivalents ($CO_{2,eq}$) [5]. However, in contrast to other major sectors of greenhouse gas emissions such as electricity and heat production [5], aircraft engines at high altitudes emit large amounts of species directly into the lower stratosphere and upper troposphere, which are alleged to affect atmospheric ozone levels. The most harmful of these emissions are nitric oxide (NO), nitrogen dioxide (NO_2), and soot particles. Figures indicate that such airplane-related emission levels during the decade of the 1990s had increased the NO_x concentrations by about 6% at cruise altitudes in the northern mid-latitudes [6], a problem still relevant in the past decade [7]. These NO_x emissions contribute to the formation of ozone in the troposphere, which is associated with a variety of symptoms for humans when exposed to high concentrations for an extended period of time [8,9]. On the contrary, NO_x emissions at supersonic aircraft's

higher altitudes deplete the stratosphere's ozone layer. This enhances the penetration of solar radiation, elevating the risk of skin cancer in more people [10].

1.2   Motivation

In order to achieve high standards concerning clean combustion technology in aircraft engines, especially regarding NO_x emissions, the major jet engine manufacturers are developing lean premixed prevaporized (LPP) combustors that operate at high pressure of up to 45 bar [11–13]. In this context, thermoacoustic instabilities often occur inside the combustion chamber; pressure waves generated by the unsteady released heat are linked to the inlet air velocity via a feedback loop, further enhancing the instabilities of the heat release [14,15]. These high-pressure waves present a hazard to the engine's robustness and life span [16]. Despite the fact that intense investigations into thermoacoustics date back to the 1960s and the Saturn V rocket of the Apollo program [17], these instabilities remain to this day extremely challenging to predict [18].

Most modern jet engines employ prefilming airblast atomizers to disintegrate the liquid fuel in a spray of droplets [8]. Since the operating principle for this type of atomizer is based on the high relative velocity between the air and the fuel [19], uncontrolled instabilities on the inlet air velocity affect the atomization process [20–23]. The spray quality affects crucial operating characteristics such as the air-to-fuel ratio (AFR) inside the chamber, the flame's stability limits, the combustion efficiency, and the NO_x emission levels [8]. Thus, predicting the performance of the atomization process under unsteady airflow conditions has a significant value.

To investigate the response of the airblast atomization process under unsteady conditions, a spray test facility was designed and set up. A novel model prefilmer was designed for extended analysis of the spray in a two-dimensional flow without swirl. A few studies have employed a similar planar model prefilmer in a variety of targets for investigation; either for similar to this work purposes in investigating the response of the spray on an acoustically forced airflow, or for fundamental atomization studies regarding the film thickness and the primary breakup phenomena [24–29]. However, in most previous studies regarding the spray response under acoustic forcing, it was challenging to produce an airflow oscillating at mainly a single frequency.

Experimental data of the atomization process under a forced flow field, in particular when the air velocity periodically oscillates at a single frequency, could be utilized in the training of machine learning algorithms in order to predict the thermoacoustic instabilities on a jet engine [30–33]. The aim of this study was to provide such data to the academic community, while also contributing to the understanding of the atomization phenomena.

1.3   Dissertation Outline

This dissertation is structured in five major chapters, including Chapter 1 which contains the introduction and motivation for carrying out the research activities in this dissertation.

In Chapter 2, the basic theoretical background is presented in order for the reader to be able to understand and comprehend the contents of the following Chapters.

The contents of Chapter 3 include the description of the experimental method divided into four main subsections. This includes the design and commission of all test rig components into an operational experimental setup, as well as the measurement techniques adopted for characterizing the airflow velocity and the produced spray. Finally, the algorithms for phase averaging of the acquired signals are presented, which were necessary since those signals were expected to be periodic.

The core of this dissertation is Chapter 4, where the results are presented and discussed in four main subsections which contain different types of results. At first, the performance of the model nozzle was investigated under steady airflow conditions. The second part includes the characterization of the airflow velocity when the oscillations are introduced in the system, in order to determine the frequency at which the air velocity oscillates and to select the conditions at which the spray would be excited. In the third part, the complete characterization of the spray under one selected frequency is presented and finally, in the fourth part the influence of the excitation frequency is studied, showing the results of the spray characteristics under the forcing of four different frequencies of similar amplitude.

Finally, Chapter 5 summarizes the outcomes of this dissertation and concludes with a vision for future research in order to expand the knowledge in this field.

2 Theoretical Background

2.1 Combustion Chamber of a Jet Engine

Aircraft gas turbines deal with the challenge of operating over a wide range of inlet pressure and temperature while remaining within the flight envelope of Mach number and altitude. To maintain an appropriate value of turbine inlet temperature, the combustor must operate at high altitudes with significantly reduced air density and mass flow, while using roughly the same fuel-to-air ratio as at sea level. Atmospheric conditions will change quite rapidly during climb and descent, and the combustor must deal with a continuously varying fuel flow without allowing the engine to flame-out or exceed temperature limits. In the event of an in-flight flame-out, the combustor must be capable of relighting over a wide range of flight conditions [34].

Conventional jet engines operate on the same principles as other internal combustion engines; the chemical energy of the fuel is converted into thermal energy, which is then converted into mechanical energy [35,36]. The combustion chamber is the core of the engine, carrying the task of burning large amounts of fuel in order to release heat and generate the necessary thrust for the aircraft to move [37].

The design of a jet engine combustion system is a complicated process that involves fluid dynamics, heat transfer, combustion, and mechanical design [34]. In jet engines, three main types of combustors have been used throughout history: tubular, annular, and tuboannular combustors [8,37].

- A **tubular** combustor is made up of a cylindrical liner placed concentrically inside a cylindrical shell. Tubular systems were less expensive and faster to manufacture than other configurations of combustors, and thus they were used in the early stages of jet engine development. However, because of their great weight and length, these combustors are more commonly employed in industrial applications.

- A **tuboannular** combustor is composed of a set of tubular liners, normally up to ten in number, which are housed inside a single annular casing. A system like this is intended as a hybrid of tubular and annular combustors, resulting in a more compact device with the mechanical strength of tubular combustor designs. On the other hand, because the design of the diffuser is problematic with this type of combustor, achieving a constant airflow pattern can be challenging.

- An **annular** combustor features a concentrically placed annular liner inside an annular shell. Its design has a clean aerodynamic shape that results in reduced pressure loss than other combustor designs. An advantage of this combustor type is the reduction of the surfaces requiring cooling. This way, a part of the cooling airflow can be directed in the combustion chamber and thus the maximum temperature in the chamber can be reduced. Given the need for a compact and aerodynamic design for jet engine combustors, this unit has been developed and optimized for high performance and has become the norm for all modern jet engines.

Regardless of the type of combustor, the chamber of a conventional jet engine is usually divided into three different zones as illustrated in Figure 2.1: the primary, the intermediate, and the dilution zone [34,37].

- The first is the **primary zone**, the principal role of which is to anchor the flame and provide sufficient time, mixing, and temperature to ensure practically complete combustion of the fuel-air mixture. The airflow aids in meeting these targets, with the development of a toroidal flow reversal that entrains and recirculates some of the hot combustion gases in order to provide continuous ignition to the incoming mixture.

- The second is the **intermediate zone**, where the injection of smaller volumes of air gradually drops the temperature to an intermediate level. This prevents the produced CO from rapidly cooling in the third zone, while it also stimulates soot oxidation and facilitates the further burning of CO and any remaining UHC.

- The third is the **dilution zone**, which accepts the remaining air and creates an acceptable temperature distribution for the turbine blades. The excess air that enters the dilution zone accounts for approximately 20-40% of the total combustor airflow [8], via one or more rows of holes in the liner walls.
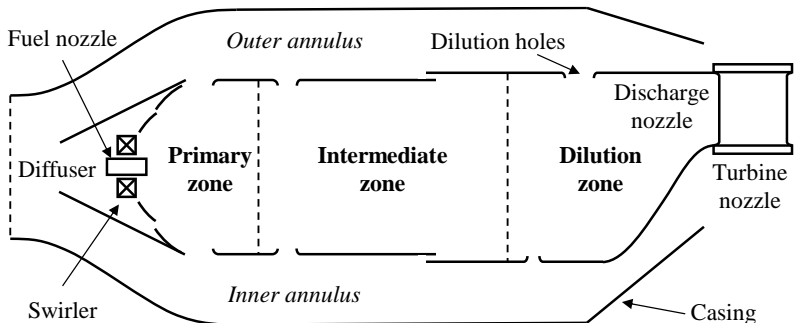
Figure 2.1: Typical structure of a conventional jet engine combustion chamber [8].

Because the target for the operation of a jet engine is the minimization of NO_x emissions due to their importance as explained in section 1.1, the combustion chambers are designed to operate in conditions favourable to achieving this goal. The most critical factor influencing NO_x production is the flame temperature. Theoretically, it peaks at stoichiometric conditions and decreases for both rich and lean mixtures [38]. Despite the fact that operating far from stoichiometric conditions reduces NO_x formation, it increases carbon monoxide (CO) and unburned hydrocarbon (UHC) production, as shown in Figure 2.2.
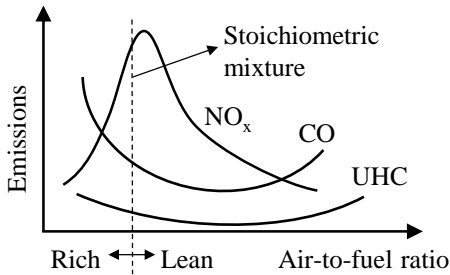
Figure 2.2: Dependence of emissions on the air-to-fuel ratio [34].

One of the methods for reducing the emissions is the dry low NO_x (DLN) operation of the engine. For this approach, the temperature is decreased without the need for water injection by simply operating moderately away from the stoichiometric conditions. Therefore, it is possible to consider either rich or lean burning in the primary zone of the chamber. The most promising approaches that have been developed for these two cases are the Rich-Quench-Lean (RQL) combustion and the Lean Premixed Prevaporized (LPP) combustion respectively.

Rich-Burn, Quick-Quench, Lean-Burn Combustor

In the RQL combustor concept, the combustion is initiated in a fuel-rich primary zone and NO_x formation rates are low due to the oxygen depletion and lower flame temperatures, as shown in Figure 2.2. The remaining air necessary to complete the combustion process is then mixed instantaneously and uniformly with the primary zone outflow, rapidly forming lean burn conditions.

The underlying principle of the RQL technology is the fast and effective injection of the quenching air in order to minimize the residence time near stoichiometric conditions [39,40]. This combustor concept is still considered a viable approach for modern jet engines, since it has been thoroughly investigated and the NO_x reduction was substantial, resulting in emission levels of approximately 50 ppmv [41–44].

Lean Premixed Prevaporized Combustor

The underlying principle of the LPP combustor is to supply the primary zone with a completely homogeneous mixture of fuel and air and to operate at highly lean conditions. In a typical LPP combustor, the fuel is at first injected, evaporated, and thoroughly mixed with the air before combustion initiates. By preventing droplet combustion and supplying the combustion zone with a lean and homogeneous mixture, the combustion process is carried out at low temperatures resulting in low NO_x emissions [11,42]. The challenge, however, is to thoroughly mix fuel vapour and air quickly and to maintain the premixing length short, in order to avoid autoignition phenomena. With the LPP

combustion concept, tests have reported NO_x emissions of less than 10 ppmv [45].

Lean Burn Direct Injection Combustor

The Twin Annular Premixing Swirler (TAPS), developed by GE Aviation, operates with the Lean Direct Injection (LDI) concept in order to exploit the advantages of lean burning, namely the low NO_x emissions [46–48]. In this concept, approximately 60 to 70% of the total airflow passes through the nozzle [49,50]. The fuel is already atomized into a spray before entering the primary zone, ensuring good mixing and partial pre-evaporation. This combustor demonstrated NO_x emissions of 52% below the CAEP/6 standards [49].

2.2 Thermoacoustic Instabilities

Combustion instabilities are a major problem in the design and development of high-performance jet engines [51,52]. These instabilities are the result of interactions between the combustion process and the acoustic fields within the combustor. If the heat released by the combustion process is periodically unsteady, the resulting acoustic pressure waves emanating from the combustion zone are periodic as well, with the same frequency. The pressure waves are returned to the combustion zone with a time delay that depends on the geometry of the chamber.
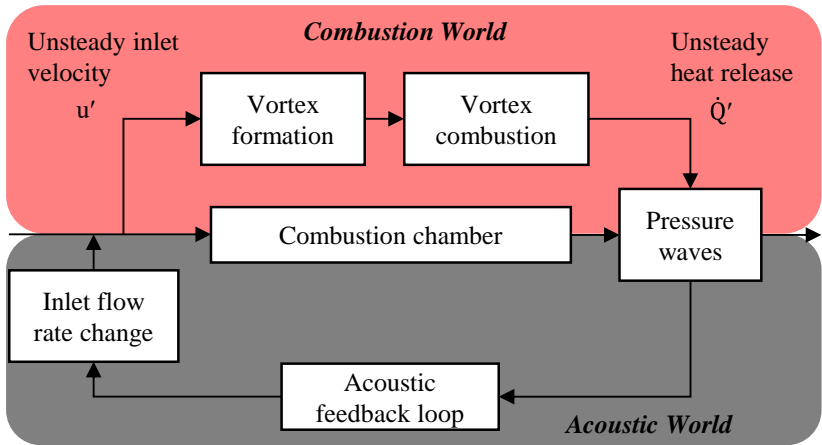
Figure 2.3: Schematic representation of the thermoacoustic instabilities principle based on the coupling of combustion and acoustics phenomena [53].

This coupling between the combustion process and the acoustic field causes energy to be added to the system with each cycle, which results in oscillations that grow in amplitude [54]. Low-frequency oscillations introduce large mechanical vibrations in the system, which may lead to serious damage to the engine hardware [52]. The described process is illustrated in Figure 2.3, where the interaction between the combustion world and the acoustic world through this acoustic feedback loop is evident. The active control of the instabilities on the combustor has an enormous potential [55].

2.2.1   Wave Equations in 1D

Considering the Navier-Stokes equations, where the viscous effects are neglected and a one-dimensional non-reacting flow is assumed, the mass, momentum, and energy conservation equations are [56,57]:

$$\frac{\partial \rho}{\partial t} + \frac{\partial}{\partial x}(\rho u) = 0 \tag{2.1}$$

$$\frac{\partial}{\partial t}(\rho u) + \frac{\partial}{\partial x}(\rho u u) = -\frac{\partial p}{\partial x} \tag{2.2}$$

$$p = C \cdot \rho^{\gamma} \tag{2.3}$$

where the energy equation is replaced by the isentropic relation. Assuming linear acoustics ($A = \bar{A} + A'$) with a perturbation significantly smaller than the average ($A' \ll \bar{A}$) and no mean flow ($\bar{u} = 0$), while conserving only the first-order terms gives [58]:

$$\frac{\partial \rho'}{\partial t} + \bar{\rho}\frac{\partial u'}{\partial x} = 0 \tag{2.4}$$

$$\bar{\rho}\frac{\partial u'}{\partial t} = -\frac{\partial p'}{\partial x} \tag{2.5}$$

$$p' = \frac{\gamma \cdot \bar{p}}{\bar{\rho}}\rho' \tag{2.6}$$

Using Eq.(2.6) in Eq.(2.4)-(2.5) in order to keep only the pressure and velocity fluctuations:

$$\frac{\partial p'}{\partial t} + \bar{\rho}\,\bar{c}^2\frac{\partial u'}{\partial x} = 0 \tag{2.7}$$

$$\bar{\rho}\frac{\partial u'}{\partial t} = -\frac{\partial p'}{\partial x} \tag{2.8}$$

Where the speed of wave propagation (sonic velocity) is:

$$\bar{c}^2 = \frac{\gamma \cdot \bar{p}}{\bar{\rho}}$$

(2.9)

This is a system with two equations and two variables, where u′ and p′ are coupled; at any given position, if p′ is always zero, then the spatial derivative of u′ is always zero, and if u′ is always zero, then the spatial derivative of p′ is always zero. These equations may be combined and lead to the wave equations:

$$\frac{\partial^2 p'}{\partial t^2} - \bar{c}^2 \frac{\partial^2 p'}{\partial x^2} = 0$$

(2.10)

$$\frac{\partial^2 u'}{\partial t^2} - \bar{c}^2 \frac{\partial^2 u'}{\partial x^2} = 0$$

(2.11)

The solution of Eq.(2.10)-(2.11) is the superimposition of two travelling waves f and g, as shown in Figure 2.4 [15].

$$p'(x, t) = f(x - \bar{c}t) + g(x + \bar{c}t)$$

(2.12)

$$\bar{\rho}\, \bar{c}\, u'(x, t) = f(x - \bar{c}t) - g(x + \bar{c}t)$$

(2.13)
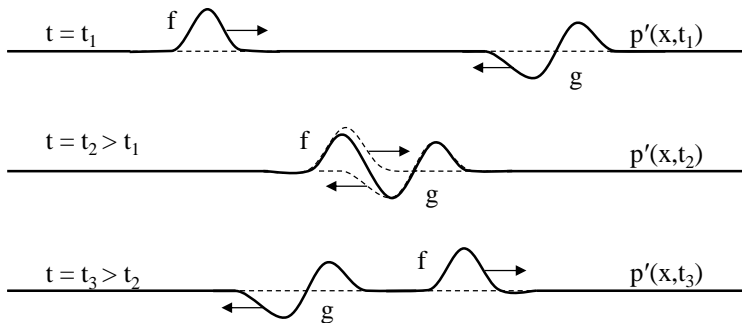
Figure 2.4: One-dimensional waves travelling in opposite directions.

Boundary Conditions

Rigid wall

In the case of a rigid wall at a specific position x_0 in the tube, the velocity at the wall is zero, as well as the velocity perturbations, so the boundary condition is $u' = 0$. Therefore, according to Eq.(2.13), the two waves are equal to each other travelling in opposite directions as shown in Figure 2.5.

$$f(x_0 - \bar{c}t) = g(x_0 + \bar{c}t) \tag{2.14}$$
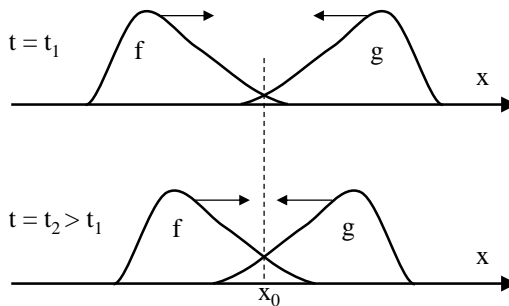
Figure 2.5: Waves in case of a rigid wall boundary condition.

Open-ended tube

In the case of an open-ended tube at a specific position x_0, at the other side of which a large vessel exists where pressure is imposed, the pressure perturbations are zero, and thus the boundary condition would be $p' = 0$. Therefore, the two waves are opposite in value according to Eq.(2.13), and travel as shown in Figure 2.6.

$$f(x_0 - \bar{c}t) = -g(x_0 + \bar{c}t) \tag{2.15}$$
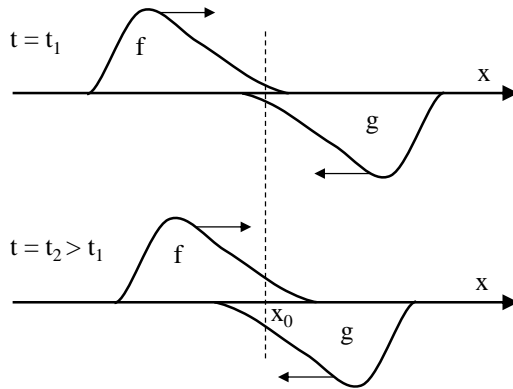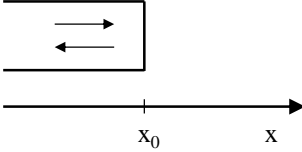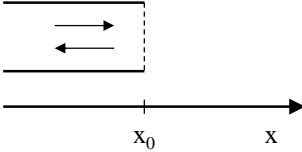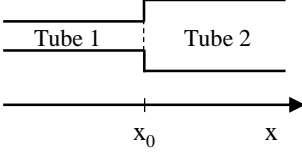
Figure 2.6: Waves in case of an open-ended tube boundary condition.

<u>Connection between two ducts</u>

A third case for boundary condition would be the position x_0 at the connection of two ducts of different heights or diameters. In this case, the pressure perturbations on tube 1 have to be equal to the pressure perturbations on tube 2, since the point x_0 is common in the two tubes. Furthermore, the velocity perturbations on this location have to follow the continuity equation due to the abrupt sectional area change. Therefore, the boundary conditions at the intermediate point between the two ducts are $p_1' = p_2'$ and $A_1 u_1' = A_2 u_2'$.

All aforementioned boundary conditions are summarized in Table 1.

Table 1: Boundary conditions for ideal one-dimensional ducts.

Configuration	Boundary condition
	$u' = 0$
	$p' = 0$
	$p_1' = p_2'$ $A_1 u_1' = A_2 u_2'$

2.2.2 Acoustics in Reacting Flows - Rayleigh Criterion

Considering the Euler equations in a one-dimensional reacting flow:

$$\frac{\partial \rho}{\partial t} + \frac{\partial}{\partial x}(\rho u) = 0 \tag{2.16}$$

$$\rho \frac{\partial u}{\partial t} + \rho u \frac{\partial u}{\partial x} = -\frac{\partial p}{\partial x} \tag{2.17}$$

$$\rho C_P \left(\frac{\partial T}{\partial t} + u \frac{\partial T}{\partial x} \right) = \dot{Q} + \frac{\partial p}{\partial t} \tag{2.18}$$

And the state equation:

$$p = \rho \, R \, T \tag{2.19}$$

Assuming linear acoustics with a perturbation significantly smaller than the average and a zero Mach number, while conserving only the first-order terms gives:

$$\frac{\partial \rho'}{\partial t} + \bar{\rho} \frac{\partial u'}{\partial x} = 0 \tag{2.20}$$

$$\bar{\rho} \frac{\partial u'}{\partial t} = -\frac{\partial p'}{\partial x} \tag{2.21}$$

$$\bar{\rho} \, C_P \frac{\partial T'}{\partial t} = \dot{Q}' + \frac{\partial p'}{\partial t} \tag{2.22}$$

$$\frac{1}{\bar{p}} \frac{\partial p'}{\partial t} = \frac{1}{\bar{\rho}} \frac{\partial \rho'}{\partial t} + \frac{1}{\bar{T}} \frac{\partial T'}{\partial t} \tag{2.23}$$

where Eq.(2.20) is the linearized continuity, Eq.(2.21) is the linearized momentum, Eq.(2.22) is the linearized energy and Eq.(2.23) is the linearized state equation. Combining the energy with the state equation, the partial derivative of the temperature perturbations can be eliminated:

$$\frac{\partial \rho'}{\partial t} = \frac{1}{c^2} \frac{\partial p'}{\partial t} - \frac{\dot{Q}'}{C_P \, \bar{T}} \tag{2.24}$$

By utilizing the linearized continuity equation, the partial derivative of the density fluctuations is eliminated:

$$\frac{1}{c^2} \frac{\partial p'}{\partial t} + \bar{\rho} \frac{\partial u'}{\partial x} = \frac{\dot{Q}'}{C_P \, \bar{T}} \tag{2.25}$$

Finally, combining Eq.(2.25) with the linearized momentum equation, the acoustic energy equation for reacting flows, when Mach = 0, is derived:

$$
\underbrace{\frac{\partial}{\partial t}\left(\frac{1}{2}\bar{\rho}u'^2 + \frac{1}{2}\frac{p'^2}{\bar{\rho}\,c^2}\right)}_{\text{Acoustic Energy}} + \underbrace{\frac{\partial}{\partial x}(u'p')}_{\text{Acoustic Flux}} = \underbrace{\frac{p'\dot{Q}'}{\bar{\rho}\,C_P\,\overline{T}}}_{\text{Source Term}}
\tag{2.26}
$$

This local equation can be integrated spatially over a computation domain V enclosed in a surface S to conclude in the final acoustic energy equation:

$$
\frac{\partial}{\partial t}E + F = \iiint \dot{Q}'p'dV
\tag{2.27}
$$

Where p' is the pressure perturbations and $\dot{Q}'$ is the heat release perturbations, while the terms E and F represent:

$$
E = \underbrace{\int_V \left(\frac{1}{2}\bar{\rho}u'^2 + \frac{1}{2}\frac{p'^2}{\bar{\rho}\,c^2}\right)dV}_{\text{Total acoustic energy in volume V}}
\tag{2.28}
$$

$$
F = \underbrace{\int_S (p'u')dS}_{\text{Total acoustic flux through surface S over the volume V}}
\tag{2.29}
$$

The source term is a correlation between unsteady pressure p' and unsteady heat release $\dot{Q}'$. This term exists due to combustion and can act as a source or a sink term for the acoustic energy. When the product of $\dot{Q}'$ and p' is positive, i.e. if the pressure oscillations p' are in phase with the unsteady heat release $\dot{Q}'$ in enough places in the combustor, the product acts as a source term for the acoustic energy and the instability of the setup is amplified. On the other hand, if unsteady heat release is at a minimum when pressure is at a maximum, the system becomes more stable as the instability decreases.

$$\iiint \dot{Q}'p'dV > 0 \qquad (2.30)$$

This qualitative criterion was first proposed by Rayleigh [59] and has been established as Rayleigh's criterion of combustion instabilities.

2.2.3 Flame Transfer Functions

A usual approach for investigating the combustion instabilities is to consider separately the acoustic phenomenon by replacing the flame with an equivalent active system described by its Flame Transfer Function (FTF) [15]. Then, the Rayleigh criterion can be applied to determine the stability limits. The FTF is a function that provides information on how perturbations of the incoming airflow influence the heat release response of the flame [60,61]. Such a dependency is expressed in the following form:

$$\frac{\dot{Q}'}{\bar{\dot{Q}}} = f\left(\frac{u'}{\bar{u}}\right) \qquad (2.31)$$

This dependency usually relies on the oscillation frequency, and thus a Fourier transformation can be used to transfer the Eq.(2.31) to the frequency domain:

$$\frac{\dot{Q}'(\omega)}{\bar{\dot{Q}}} = FTF(\omega)\left(\frac{u'(\omega)}{\bar{u}}\right) \qquad (2.32)$$

where $Q'(\omega)$ and $u'(\omega)$ are the complex fluctuations and $FTF(\omega)$ is defined as the complex flame transfer function. Considering waveforms of sinusoidal shape, the fluctuations can be elegantly described in the complex plane with a real amplitude $\hat{Q}(\omega)$, $\hat{u}(\omega)$, and a phase angle φ:

$$\dot{Q}'(\omega) = \widehat{\dot{Q}}(\omega)\, e^{i\omega t + i\varphi_{\dot{Q}}(\omega)}$$

(2.33)

$$u'(\omega) = \hat{u}(\omega)\, e^{i\omega t + i\varphi_u(\omega)}$$

(2.34)

Therefore, the transfer function is:

$$FTF(\omega) = \frac{\widehat{\dot{Q}}(\omega)}{\hat{u}(\omega)} \frac{\bar{u}}{\bar{\dot{Q}}}\, e^{i\left[\varphi_{\dot{Q}}(\omega) - \varphi_u(\omega)\right]}$$

(2.35)

The amplitude of the flame transfer function is determined by the ratio of the oscillation amplitudes and the phase by the difference of their phases.

$$\widehat{FTF}(\omega) = \frac{\widehat{\dot{Q}}(\omega)}{\hat{u}(\omega)} \frac{\bar{u}}{\bar{\dot{Q}}}$$

(2.36)

$$\varphi_{FTF(\omega)} = \varphi_{\dot{Q}}(\omega) - \varphi_u(\omega)$$

(2.37)

To experimentally determine the flame transfer function, the luminescence signal of the excited OH(OH*) molecule within the flame is acquired as the measure for heat release [62]. The velocity is either measured directly via hot-wire anemometry, or the acoustic velocity is obtained by utilizing the multi-microphone method [63–65]. Then, the FTF is determined in discrete frequency steps by forcing the system, utilizing an external excitation device.

2.3   The Atomization Process

Because aircrafts must carry the fuel required for their missions, liquid fuels have become the norm [34]. Liquid fuel combustion in gas turbines is dependent on efficient atomization to enhance the specific surface area of the

fuel and achieve high rates of mixing and evaporation [66]. In most combustion systems, reducing mean fuel drop size leads to higher volumetric heat release rates, easier start-up, a broader burning range, and lower pollutant exhaust concentrations [67–69].

2.3.1 Basic Atomization Processes

The atomization process disintegrates a bulk liquid volume into a spray of small particles, allowing it to disperse into the gas stream. This is the initial necessary step for the start of the liquid fuel combustion process. The mass and heat transfer phenomena, such as molecular diffusivity and evaporation rate, have a significant impact on the combustion progress. The physical phenomena that govern the processes outlined above are dependent on the atomization quality. The atomization process intends to increase the surface area of the liquid, hence increasing the mass and heat transfer rates as well as the mixing rate of the fuel and the oxidizer [66]. Furthermore, because the ratio of surface area to volume is inversely proportional to the particle's diameter, the atomized fuel's evaporation rate is intimately tied to the droplet's surface. This is supported by the d^2-law regarding droplet evaporation, where the surface of a droplet decreases linearly with time [70,71]. As a result, a smaller particle diameter would result in more evaporation mass per volume unit. Therefore, in traditional liquid fuel combustion systems, the formation of tiny droplets is critical since it increases evaporation and combustion rates.

2.3.1.1 Single Drop Breakup

The interaction of the drop with the aerodynamic forces of the surrounding air causes the drop to disintegrate [72]. The precise mathematical solution of the

breakup dynamic demands information on the distribution of aerodynamic pressure at each location on the drop surface. However, once the drop is deformed by these forces, the pressure distribution on its surface changes, resulting in an altered state of equilibrium or the possibility of breakup. The surface tension strives to compress the drop, increasing the inner pressure. Neglecting gravity leads to a balance between the pressure force and the force that results from the surface tension [73,74].
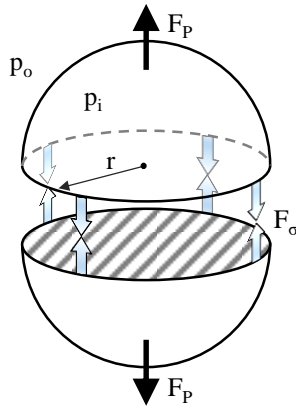
Figure 2.7: Equilibrium consideration for a spherical liquid drop [73].

Assuming a perfectly spherical drop as in Figure 2.7, the associated equilibrium is quite straightforward. If a drop is cut at the equator, the surface tension force would be as follows:

$$\left|\vec{F_\sigma}\right| = 2\,\pi\,r\,\sigma$$

(2.38)

The resulting pressure force points in the vertical direction and has the same value as if the equatorial surface would be subject to the pressure difference $\Delta p = p_\sigma = p_i - p_o$:

$$|\overrightarrow{F_P}| = \Delta p \, \pi \, r^2 = (p_i - p_o)\pi \, r^2 \qquad (2.39)$$

From the balance of the two forces:

$$\Delta p = p_\sigma = p_i - p_o = \frac{2\sigma}{r} \qquad (2.40)$$

At any point, the internal pressure p_i is sufficient to balance the outer aerodynamic pressure p_o and the surface tension pressure p_σ so that:

$$p_i = p_o + p_\sigma = \text{const.} \qquad (2.41)$$

A drop may remain stable as long as a change in the outer pressure p_o can be compensated by a corresponding change in the surface tension pressure p_σ to maintain p_i constant. If, however, p_o becomes large enough compared to p_σ, the outer pressure may deform the drop to a point that leads to further reduction of p_σ and ultimately to the disintegration of the drop into smaller droplets [75]. In the case of a large drop, Eq.(2.40) indicates that the surface tension pressure would be smaller than in the case of a small droplet, meaning that a large drop is more possible to further disintegrate.

Over the years, high-speed imaging techniques have revealed that liquid drop can split up under the action of aerodynamic forces in numerous ways, depending on the conditions. Three main categories of drop deformation were identified by Hinze [76]:

- *Lenticular deformation*, where the drop is flattened to an ellipsoid shape. This ellipsoid is converted into a torus which then gets stretched and disintegrates into small drops.

- *Cigar-shaped deformation*, where the drop is elongated to form a long cylindrical thread or ligament that further breaks into small drops.
- *Bulgy deformation*, where the local deformations on the drop surface create bulges that eventually detach themselves to form smaller drops.

These three categories are schematically illustrated in Figure 2.8:
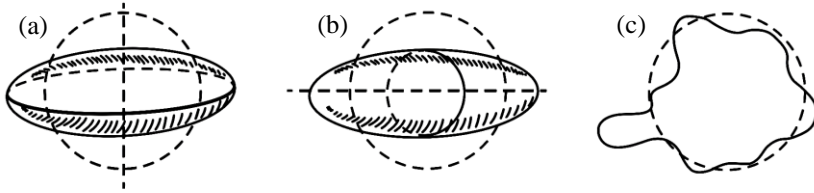
Figure 2.8: Three different modes of drop deformation: (a) lenticular, (b) cigar-shaped, and (c) bulgy deformation [66].

The breakup of a drop in an airflow is controlled by the dynamic pressure, surface tension, and viscous forces [77]. For low-viscosity liquids, the deformation of the drop is governed primarily by the ratio of the aerodynamic forces and the surface tension forces. The dimensionless entity that represents this ratio is the Weber number [78,79]:

$$\text{We} = \frac{\rho_A u_R^2 D}{\sigma} \tag{2.42}$$

where $u_R = u_A - u_L$ is the relative velocity between the air and the liquid drop. A high Weber number denotes larger external aerodynamic forces that tend to deform the drop in comparison with the surface tension forces that tend to reform it.

For a given liquid to disintegrate, the condition would be that the aerodynamic forces are just equal to the surface tension forces:

$$\underbrace{c_D \pi \frac{D^2}{4} \frac{1}{2} \rho_A u_R^2}_{\text{Aerodynamic forces}} = \underbrace{\pi D \sigma}_{\text{Surface tension forces}} \qquad (2.43)$$

This condition is linked to a critical value of the Weber number [66]:

$$We_{crit} = \left(\frac{\rho_A u_R^2 D}{\sigma} \right)_{crit} = \frac{8}{c_D} \qquad (2.44)$$

For a determined relative velocity, the maximum stable drop diameter can be calculated from Eq.(2.44), and reversely the critical relative velocity can be calculated for a determined drop size.

The viscosity of the liquid acts in favour of the drop stabilization. The dimensionless entity that describes the relation of the aerodynamic forces with the viscosity forces is the Reynolds number:

$$Re = \frac{\rho_A u_R D}{\mu_A} \qquad (2.45)$$

Combining the information of Re and We to eliminate the relative velocity, a new dimensionless entity emerges, the Ohnesorge number, which indicates the relationship between the viscous and the surface tension forces [80,81]:

$$Oh = \frac{\sqrt{We}}{Re} = \frac{\mu_A}{\sqrt{\rho_A \sigma D}} \qquad (2.46)$$

The role of the two key parameters for the breakup, i.e. Weber and Ohnesorge number, has been thoroughly studied and a regime map has been developed as shown in Figure 2.9 [82].
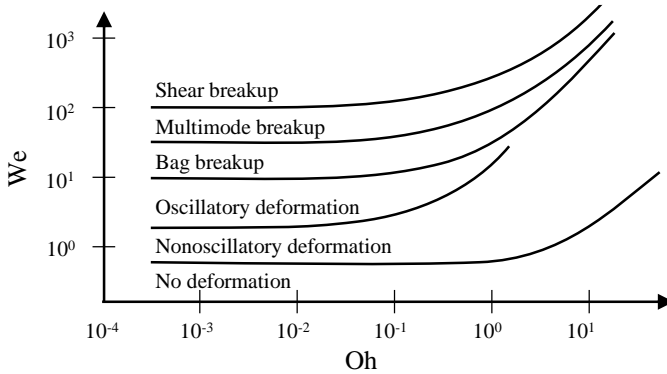
Figure 2.9: Breakup mode depending on Weber number and Ohnesorge number [82].

Table 2: Breakup mechanisms of a single Newtonian drop (flow direction from left to right) [83].

Breakup mode	Weber number				
Vibrational breakup	$0 < We < 12$				
Bag breakup	$12 < We < 50$				
Multimode breakup	$50 < We < 100$				
Sheet stripping	$100 < We < 350$				
Wave crest stripping	$350 < We$				
Catastrophic breakup	$350 < We$				

The breakup mode shifts to favour more rapid and destructive disintegration of the drop as the Weber number increases for a large range of Ohnesorge number values. This is also shown in Table 2 where the different breakup modes are categorized by Pilch and Erdman, depending on the value of the Weber number [83].

2.3.1.2 Liquid Jet Disintegration

In contrast to the single drop breakup, the disintegration of liquid jets reveals a far more complex behaviour, involving multiple phenomena. The creation and propagation of waves on the liquid's surface causes a loss of stability and ultimately a liquid breakup. Small perturbations on the liquid surface were forced in various experiments; the liquid swirling in the former category, the liquid expansion owing to the induced pressure drop, and the atomizer's potential vibrations all contribute to the perturbations. The interaction of the liquid with its environment is what describes the latter (i.e., aerodynamic forces).

Liquid jet breakup is thought to be caused by four distinct mechanisms. The first is created by axisymmetric waves generated by jet speeds of 1 m/s, while the second is caused by asymmetric waves (referred to as "first wind-induced atomization") that apply to jet velocities of 10 m/s. Furthermore, at speeds up to 100 m/s, the high relative velocity between the jet and its surroundings led the liquid jet to disintegrate due to aerodynamic forces as the third mechanism. The influence of turbulence and aerodynamic forces are prominent in the atomization process ("turbulent breakdown"), according to a fourth mechanism described and documented in the literature. The jet breakdown map and several jet disintegration methods are depicted in Figure 2.10 [84–87].
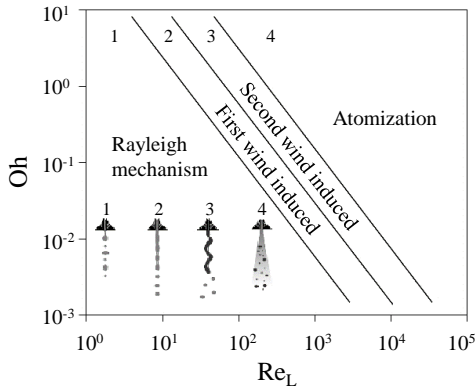
Figure 2.10: Mechanisms of jet breakup [84–87].

The so-called Rayleigh mechanism was discovered when Rayleigh researched the breakup of liquid jets at low velocities in a vacuum [88]. It is characterized by the generation of large drops of rather uniform size, and the diameter of the drops obtained can be predicted using the following equation:

$$D > 1.436 \cdot d \tag{2.47}$$

where D stands for drop diameter, and d stands for orifice diameter. Furthermore, according to Rayleigh's research, hydrodynamic instabilities are initiated by wavelengths greater than the jet's perimeter, with the wavelength at which the jet becomes unstable being defined as:

$$\lambda = 4.51 \cdot d \tag{2.48}$$

Surface tension damps wavelengths with magnitudes less than a minimum value, according to Weber, whereas larger magnitudes amplify their influence on drop disintegration [78]. The damping effects due to higher velocity tend to

increase the optimum wavelength described by Eq.(2.48), as illustrated in these tests. The correlation for the mean drop size produced by a liquid jet was derived:

$$\frac{D}{d} = 1.436(1 + 3 \cdot Oh)^{1/6} \qquad (2.49)$$

Because of the larger relative velocity between the gas and liquid phases in the first wind-induced breakup regime, a static pressure distribution across the jet is produced and thus the surface tension effect is amplified, accelerating the breakdown process. Many jet diameters downstream of the nozzle's exit, the produced drop diameter D is comparable to the orifice diameter d.

The second wind-induced breakage occurs at greater relative velocities. The unstable expansion of short-wavelength waves acting on the jet's surface causes the drop formation. The diameter of the resulting drop is lower than the orifice diameter d. Furthermore, the turbulent breakdown process (atomization) disintegrates the jet, particularly at the nozzle's exit, resulting in droplet sizes that are quite small.

2.3.1.3 Liquid Sheet Disintegration

The breakup of liquid sheets under the assistance of an airflow has been thoroughly studied since the 1950s both theoretically [89–94] as well as experimentally [95–100]. Based on the gas-to-liquid velocity ratio, there are two fundamental liquid sheet breakup regimes [100]. The development of sinuous and dilatational waves, according to Hagerty and Shea, was most likely on the surface of a liquid sheet [93]. Sinusoidal and dilatational waves travelled through the liquid sheet with minimal amplitude increase, resulting in strong

liquid sheet penetration and a small spray angle. This sort of mechanism, schematically illustrated in Figure 2.11(a), is known as a cellular breakdown regime because disintegrating ligaments formed in both span-wise and stream-wise directions [100].

Because of the created vorticity, stream-wise ligaments were forced to span-wise ligaments as the gas-to-liquid velocity ratio rose. As demonstrated in Figure 2.11(b), the sinusoidal oscillation's rapid amplitude growth promoted a high spray angle, a short sheet breakup length, and stretching of stream-wise ligaments to mostly form droplets. The stretched stream-wise ligament breakup regime is the name for this process [100].
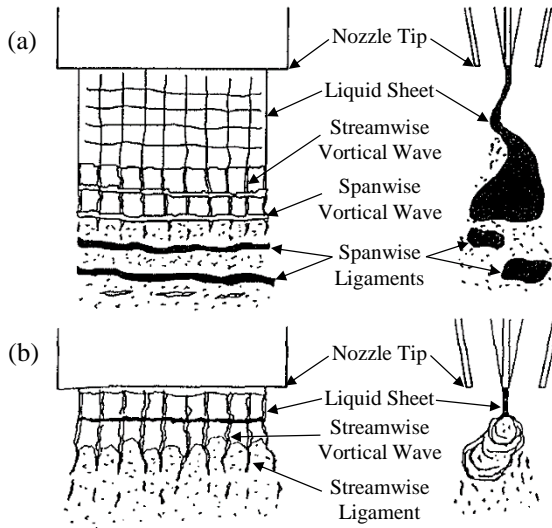
Figure 2.11: Illustration of liquid sheet breakup regimes: (a) cellular breakup and (b) stretched stream-wise ligament breakup [100].

Rangel and Sirignano discovered that the density ratio between the liquid sheet and the surrounding gas influences the development rates of sinuous and dilatational waves [90]. The external forces lowered the thickness of the liquid sheet during the disintegration, according to the analytical investigation of Dombrowski and Johns, where the viscosity of the liquid was also taken into consideration [89].

The disintegration of a liquid sheet is mostly influenced by the liquid's discharge velocity. The breaking up of a liquid sheet into droplets is caused by the loss of stability caused by acting waves on the interface between the continuous and discontinuous phases. Three alternative forms of sheet disruption have been found based on the liquid discharge velocity, as shown in Figure 2.12 [101]:

- The liquid layer grows thinner as the distance downstream of the atomization edge increases, owing to a discharge velocity on the order of a few meters per second. Perforations form in the region with the suitably thin area, and ligaments, which are prone to loss of stability, disintegrate further into droplets.
- At greater discharge velocities, annular and circumferential waves with a longitudinal direction parallel to the sheet's velocity cause disruptions that disintegrate the sheet into annuli, resulting in the creation of droplets.
- At discharge velocities of up to 100 m/s, the flat sheet disintegrates directly into droplets as a result of short-wavelength disturbances of high amplitude, resulting in a greater loss of stability.
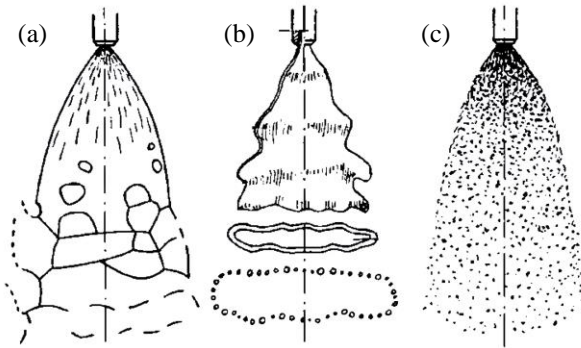
Figure 2.12: Liquid sheet disintegration in a swirl atomizer due to: (a) perforation, (b) wave phenomena, and (c) liquid atomization [101].

Dombrowski and Fraser have documented the early flow visualization of co-flowing air streams interacting with a liquid sheet. Although the aforementioned three kinds of sheet disintegration can be defined for a liquid sheet, they found that the liquid thread or jet was invariably the last phase of the breakdown process. Their conclusion was that the influence of liquid density on sheet disintegration is insignificant, but the viscosity and surface tension have similar effects on the liquid sheet's instability [95].

The development and movement of vortices in the surrounding air suggested causation of the liquid sheet breakup by vortices, according to Crapper et al. [96,97]. The effects of air and liquid stress on ligament development, growth, and lifespan were investigated by Strapper [100]. Berthoumieu et al. studied how a liquid sheet breaks up on a prefilming surface, with their research concentrating on calculating the liquid sheet's frequencies before the breakup [99].

The influence of film thickness on the atomization quality of an airblast atomizer was extensively researched by Rizk and Lefebvre [102]. High viscosity fluids with high flow rates result in thicker films, whereas thinner liquid films create smaller Sauter Mean Diameter (SMD) droplets, resulting in a SMD proportional to $t^{0.4}$, where t in this context is the film thickness. In addition, Gepperth et al. evaluated the influence of air velocity, atomizing edge thickness, prefilming length, liquid film flow rate, and the liquid's physical characteristics on primary atomization, finding that the first two factors dominate [27,103]. Despite the fact that the physical characteristics of the liquid clearly impact ligament formation, they have a minor effect on mean droplet diameter.

2.3.2 Droplet Size Distribution

An atomizer can produce a wide spectrum of droplet sizes due to the highly statistical and chaotic nature of the atomization process and the various varied breakup mechanisms referred in Table 2. As a result, the spray is commonly observed as a spectrum of droplet diameters dispersed around a mean value. The concept of atomization quality is used to describe both the degree and the uniformity of the atomization process. The degree of atomization is linked to the mean droplet diameter, with a higher degree of atomization corresponding to a lower mean droplet diameter. The uniformity of the atomization process is related to the dispersion of droplet size; a low dispersion is achieved with a high spray uniformity [101]. These parameters are utilized in various fields to define the atomization quality standards. The droplet size distribution is a critical characteristic that defines the spray quality. In the case of spray combustion, the droplet size frequency and spatial distribution determine

crucial flame attributes such as heat release, flame stability, and emissions levels [8]. The evaporation and combustion of liquid fuel droplets have been extensively investigated over the past decades, and reviews from numerous studies are available in the literature [104–106]. For optimal operation in some applications, the size distribution must follow a specific pattern (narrow or broad, few large droplets or few small droplets, etc.) [107]. As a result, dependable methods for accurately describing the sprays are necessary.

The distribution of droplet sizes can be illustrated graphically as well as mathematically. The graphical representation may be formed by drawing a droplet size histogram, with each ordinate indicating the number of droplets whose dimensions lie within the boundaries D - $\Delta D/2$ and D + $\Delta D/2$, as shown in Figure 2.13(a). As ΔD decreases, the histogram adopts the shape of a frequency curve, which may be considered as a spray characteristic if it is based on sufficiently large samples. This curve is commonly referred to as a frequency distribution curve [66].
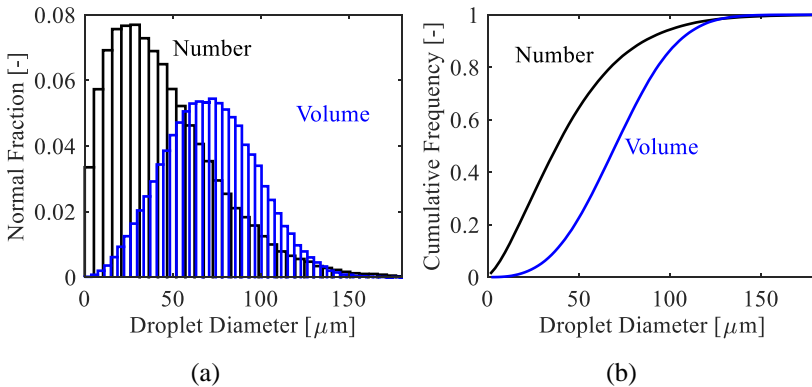
Figure 2.13: Graphical representation of number and volume fraction: (a) distribution representation and (b) cumulative frequency representation.

Moreover, when representing the droplet size distribution using a frequency plot, it is useful to consider a cumulative distribution representation as shown in Figure 2.13(b). This is simply the frequency distribution's integral, and it reflects the proportion of the total number of droplets in the spray that are smaller than a specific diameter. The ordinate values could be expressed in a variety of formats, such as the absolute number of droplets with a specific diameter, the relative number or fraction of the total, or the fraction of the total number in each size class.

Using finite samples of droplet size measurements, mathematical distribution functions have been established to capture the complete spray droplet distribution. Some of the drawbacks associated with the graphical representation can therefore be overcome, and the comparison and correlation of experimental data can be simplified. The most widely used functions are the normal, log-normal, and Rosin-Rammler distributions. There is no particular distribution function able to characterize all experimental data of droplet sizes; instead, several distribution functions must be tried to determine the best match to a set of experimental data. The most extensively used is the one developed by Rosin and Rammler [108]. The Rosin-Rammler distribution is expressed as:

$$Q = 1 - e^{-(D/X)^q} \tag{2.50}$$

where Q is the fraction of the total liquid volume contained in droplets smaller than D in diameter, while q and X are constants [109]. The exponent q is a measure of the spread of droplet sizes and usually ranges from 1.5 to 4 [66]. A large value of q corresponds to a more uniform size distribution. The Rosin-Rammler model is based on the assumption that droplet sizes are limitless. This

allows the data to be extrapolated down to very small droplet sizes, where experimental measurements are difficult to perform and not very reliable.
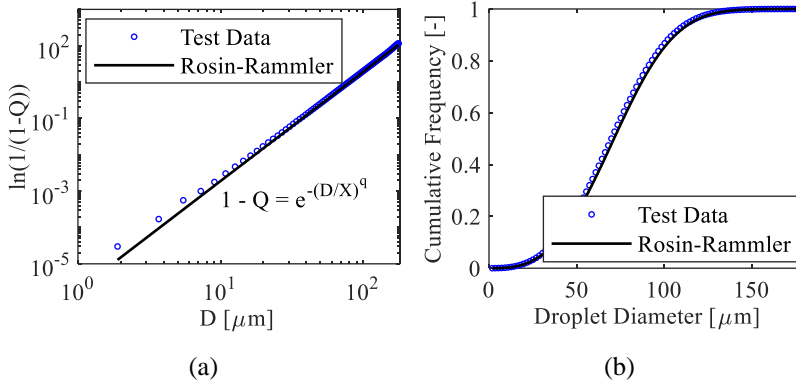
Figure 2.14: Typical Rosin-Rammler distribution: (a) in a log-log graph representation and (b) in a cumulative distribution representation.

Figure 2.14(a) is a typical Rosin–Rammler distribution represented in a logarithmic scale. The slope of the line yields the value of q, whereas X, which is some sort of a representative diameter, is the value of D for which the following equation is satisfied:

$$1 - Q = e^{-1} \tag{2.51}$$

The solution to this equation is $Q = 0.632$, which means that X is the drop diameter such that 63.2% of the total liquid volume is in droplets of smaller diameter. For this reason, the constant X is usually referred to as $D_{63.2\%}$.

To characterize a spray, it is more convenient to deal with the various mean or average diameters instead of describing the complete droplet diameter distribution. A mean droplet diameter is a common measure that defines a

spray of uniform droplets instead of the actual spray. The mean droplet diameters can be determined in a variety of methods to reflect the number, diameter, surface, or volume of droplets. Different mean diameters are relevant depending on the application. The mean diameter does not provide information on the droplet spray as a whole, but it is the most useful measure for evaluating the atomization quality. Among the most used mean diameters are: the Sauter Mean Diameter, length mean diameter, surface area mean diameter, volume mean diameter, surface area-length mean diameter, volume-length mean diameter, and De Brouckere or Herdan mean diameter. The various mean diameters utilized in different applications are summarized in Table 3.

The Sauter Mean Diameter (SMD), originally developed by Josef Sauter, is the diameter of the droplet whose volume-to-surface area ratio is the same as that of the entire spray [110]. The SMD is used to define the atomization quality in combustion applications. This diameter is a measure that indicates the fineness of sprays in terms of the spray's surface area. The expression for SMD is

$$\text{SMD} = D_{32} = \frac{\sum N_i D_i^3}{\sum N_i D_i^2} \tag{2.52}$$

where the subscript i represents the diameter range considered, N_i is the number of droplets in the considered diameter range, and D_i is the median diameter of the considered range. The arithmetic mean diameter, also known as the length mean diameter, D_{10}, is the linear average of all the droplets in the spray.

$$D_{10} = \frac{\sum N_i D_i}{\sum N_i} \tag{2.53}$$

The droplet diameter of an equivalent set with the same number of droplets and total surface area of all droplets as the genuine set is the surface mean diameter D_{20}.

$$D_{20} = \left(\frac{\sum N_i D_i^2}{\sum N_i} \right)^{1/2}$$

(2.54)

D_{30} is the volume mean diameter, the diameter of a droplet whose volume, multiplied by the number of droplets, equals the total volume of the spray.

$$D_{30} = \left(\frac{\sum N_i D_i^3}{\sum N_i} \right)^{1/3}$$

(2.55)

The surface area-length mean diameter, D_{21}, is defined as follows:

$$D_{21} = \frac{\sum N_i D_i^2}{\sum N_i D_i}$$

(2.56)

The volume-length mean diameter, D_{31}, provides information regarding the spray evaporation:

$$D_{31} = \left(\frac{\sum N_i D_i^3}{\sum N_i D_i} \right)^{1/2}$$

(2.57)

The Herdan mean, also known as De Brouckere diameter, D_{43}, is used in the combustion process and is defined as follows:

$$D_{43} = \frac{\sum N_i D_i^4}{\sum N_i D_i^3}$$

(2.58)

Table 3: Classification of droplet diameters based on their application field [108,111].

Mean diameter	Name	Application
D_{10}	Arithmetic/Length	Evaporation
D_{20}	Surface	Surface area controlling (e.g. absorption)
D_{30}	Volume	Volume controlling (e.g. hydrology)
D_{21}	Surface-Length	Adsorption
D_{31}	Volume-Length	Evaporation, molecular diffusion
D_{32}	Sauter (SMD)	Mass/heat transfer, combustion
D_{43}	De Brouckere	Combustion equilibrium

There are various other representative diameters that could be used to define the distribution function. These include the volume or mass-based diameters. For example, $D_{0.1}$ is the drop diameter such that 10% of the total liquid volume lies in droplets of smaller diameters. Most used in this context are $D_{0.1}$, $D_{0.5}$ (also referred to as the mass median diameter) and $D_{0.9}$ [66].
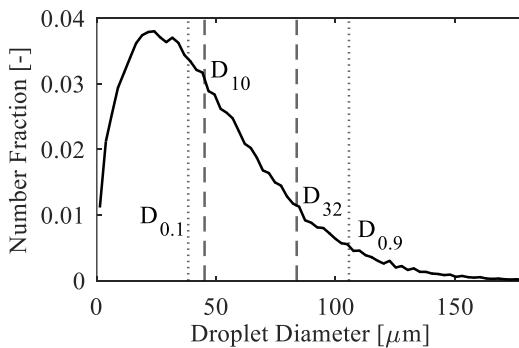
Figure 2.15: Locations of various representative diameters on a size distribution.

A spray contains many particles; therefore, it is essential to include all of the droplets in the measuring sample. Droplets with small diameters typically account for a significant fraction of the spray. The big diameter droplets have the most influence on the computation of the mean droplet diameter and missing one large droplet can modify the average diameter of the spray by up to 100%. It is essential to measure at least 5,500 droplets in order to obtain an accurate approximation of the spray quality [66]. The accuracy of the mean diameter calculated for various sample sizes is shown in Table 4.

Table 4: Influence of sample size on the accuracy of droplet size distribution measurements [66].

Droplet number in sample	Accuracy (%)
500	±17
1,500	±10
5,500	±5
35,000	±2

2.3.3   Atomizer Types & Airblast Atomization

The atomizers are categorized according to the type of energy they use for the atomization process, which can be either the pressure or kinetic energy of the liquid, the mechanical energy applied by vibrating or rotating devices, or the aerodynamic forces from the momentum exchange of a high-velocity gas with the liquid [112,113]. The driving factor of the breakup mechanism, however, remains the same in all three categories; a high relative velocity between the gas and the fluid, which is achieved by high liquid velocities and gas liquid velocities, or vice versa.

Pressure Atomizers

The so-called pressure atomizers fall within the first category of pressure energy of the fluid; they deal with the capillary breakdown of a jet or liquid sheet injected at high pressure and velocity from the nozzle. The liquid mass flow through the pressure atomizer is proportional to the square root of the pressure difference. As a result, the atomization quality is determined by the system and liquid pressure [114]. In Figure 2.16, different types of pressure atomizers are illustrated according to the literature [66].

Liquid ⟶ ▭ Plain-orifice

Liquid ⟶ Simplex

Primary ⟶
Secondary ⟶ Duplex

Primary ⟶
Secondary ⟶ Dual-orifice

Liquid ⟶ Fan spray

Supply ⇄
Spill Spill return
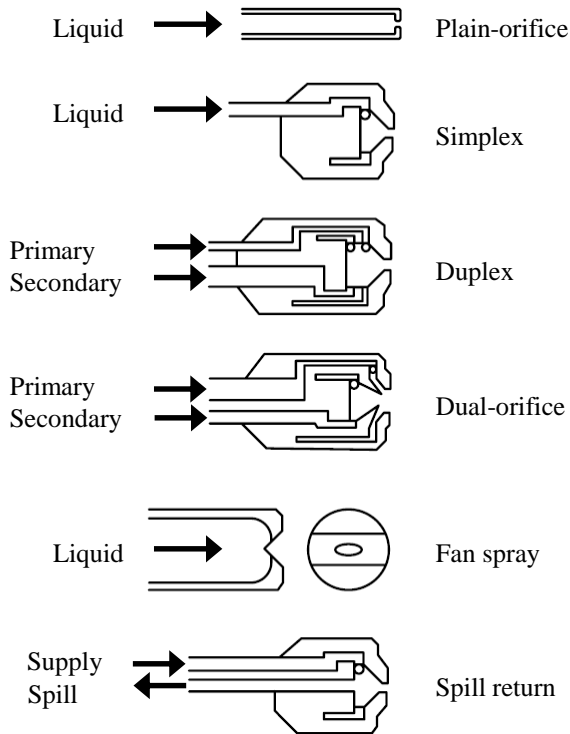
Figure 2.16: Pressure atomizers [66].

Rotary Atomizers

The liquid's centrifugal forces are the subject of the second category of atomizers [66]. A disk or a cup is usually driven by an electrical motor; the centrifugal energy of the atomizer is transferred to the liquid, causing it to discharge at a very fast rate and disintegrate into droplets. The atomization quality is determined by the disk's rotational speed [114]. The concept of a rotary atomizer is schematically depicted in Figure 2.17 [66].
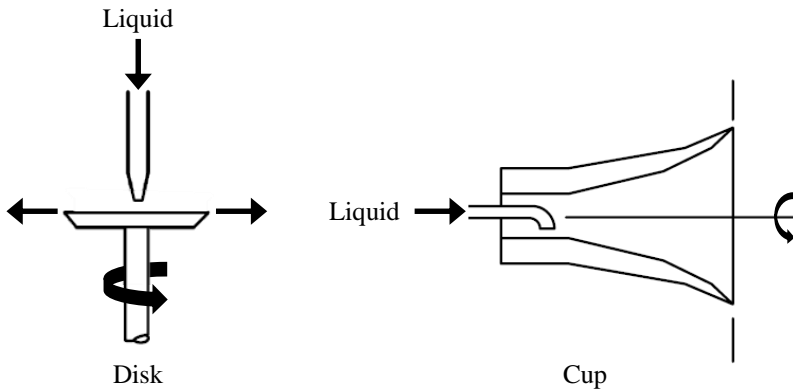
Figure 2.17: Rotary atomizers [66].

Twin-Fluid/Airblast Atomizers

Finally, the twin-fluid atomizers, which exploit the shear stress induced by the exchange of momentum at the gas-liquid interface, fall into the third category. Typical atomizers of this category are depicted in Figure 2.18 [66]. Air-assist atomizers and airblast atomizers are the two common types of twin-fluid atomizers. The distinction between the two setups is that the former consumes

tiny volumes of gas at near sonic velocities. The latter, on the other hand, employs a large amount of air at quite lower velocities.
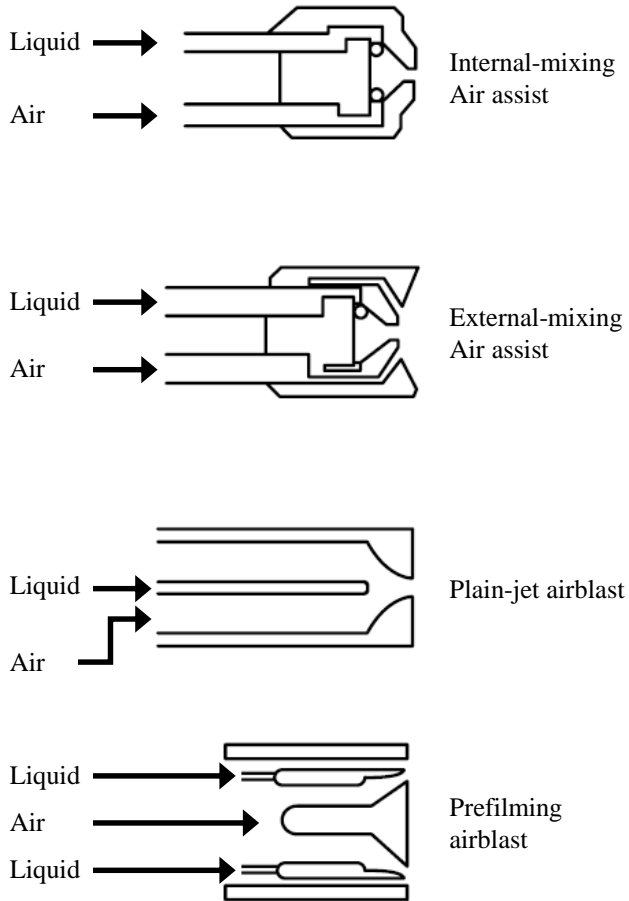
Figure 2.18: Twin-fluid/airblast atomizers [66].

Airblast nozzles are an excellent choice for atomizing liquid fuels in continuous-flow combustion systems such as gas turbines, where high air velocities are typically easily accessible. The most popular type of airblast atomizer involves spreading the liquid into a thin conical sheet and then exposing it to high-velocity air streams on both sides of the sheet. The performance of the atomization process in a prefilming airblast nozzle is generally superior to that of the conventional plain jet airblast nozzle, in which the liquid is injected into the air stream in the form of one or more discrete jets [115,116]. For these reasons, the airblast atomizer has found widespread use in the aviation industry, from where it was originally developed [66].

The airblast atomizer employs the kinetic energy of the flowing air stream to disintegrate the liquid sheet into ligaments and then in a spray of droplets. Because the air velocity through an airblast atomizer is restricted to a maximum value (often approximately 120 m/s), which corresponds to the pressure difference across the combustor liner, a large mass flow of air is necessary to effectively atomize the liquid fuel.

Airblast atomizers offer several benefits over pressure atomizers, particularly when used in high-pressure combustion systems. The main advantage is that they utilize the already existing pressure drop in the combustion chamber when a pressure atomizer would require a pump to generate a high pressure. They produce a fine spray while demanding significantly lower fuel pump pressures for that result, compared to the pressure atomizers. Furthermore, because the airblast atomization process favours the thorough mixing of air and fuel, the subsequent combustion process is characterized by very low soot formation and a low-luminosity blue flame, resulting in reasonably low flame radiation and exhaust smoke.

The majority of systems in use today that employ airblast atomizers are of the prefilming kind, in which the liquid is initially sprayed out in a uniform thin film before being sheared and atomized by the high-velocity air stream [117,118]. A prefilming airblast atomizer is illustrated in Figure 2.19. The air, shown in red, flows through the swirler channels while the injector sprays the liquid fuel onto the prefilming surface. To allow the atomizing air to impact both sides of the liquid sheet, two independent airflows are provided. The air exiting the swirler channels shears the liquid film that has been formed on the surface of the prefilmer, causing the primary breakup at the prefilmer edge. The two swirling airflows converge downstream of the atomizer's tip and carry the sprayed fuel into the primary combustion zone [119].
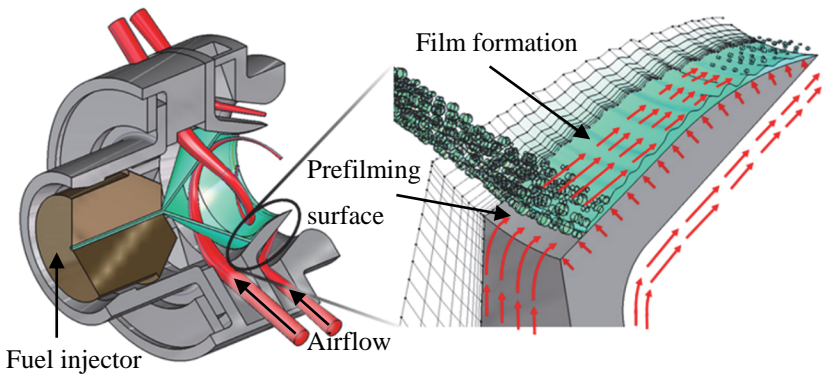
Figure 2.19: Lean-Premixed-Prevaporized airblast atomizer representation [120].

In the context of prefilming airblast atomizers, it has been shown that in order to obtain minimum drop sizes, the physical contact between the air and the liquid has to be maximized. It is critical to ensure that the liquid sheet developed at the atomizing edge is exposed to a high-velocity airflow on both

sides. This also guarantees that the droplets remain buoyant and prevents liquid accumulation on solid surfaces [121].

The atomizer geometry along with the air and liquid properties are the main factors influencing the mean droplet size of the spray. Viscosity, surface tension, and density are the key liquid properties in airblast atomization [122,123]. Air velocity is without a doubt the most critical element of the airflow determining mean drop size. The SMD of low-viscosity liquids is generally inversely related to the air velocity. This emphasizes the significance of arranging for the liquid to be exposed to the maximum feasible air velocity along with the available pressure drop in the airblast atomizer design.

3 Experimental Method

This investigation focuses on the generation of a database regarding the spray response on unsteady airflow conditions. These data are a critical input for the research fellows dealing with predicting thermoacoustic instabilities using machine learning methods, as well as for providing more insight into the chaotic nature of the prefilming airblast atomization process.

3.1 Atmospheric Spray Test Facility

To predict the spray response on the airblast atomization process under an unsteady airflow, a test rig had to be designed, evaluated, and commissioned [124]. A schematic diagram of the test rig is shown in Figure 3.1. The air is supplied in the system by a compressor and the flow is divided into two different branches. A certain amount of the total air mass flow passes the siren, a pulsating device that introduces the oscillations in the airflow velocity. The rest of the air mass flow bypasses the siren through a plenum. The amount of air flowing in each branch is controlled by a set of valves and a flow meter (KROHNE Optiswirl 4200, 4070). The two streams co-axially mix in a long resonance tube, at the end of which the airblast model prefilmer is fixed. The liquid (water in the present work) is fed into the prefilmer from a pressurized vessel using a 200 bar Nitrogen bottle. The mass flow rate of water is regulated by a set of two independent needle valves and a mass flow meter (Yokogawa RotaMass RCCF31). After the atomization process, the sprayed water is collected in a tank and a vacuum pump (Nilfisk T40W L100) sucks the excess air, in order to avoid flow unwanted droplet recirculation in the measurement

region. The test rig was surrounded by a three-axis translation stage regulated via a step motor controller (isel C 142-4), where the measurement techniques could be mounted in order to provide flexibility in the selection of measurement locations.

Water supply   Compressor

Valves

N₂

Flow Meters

Needle valves

Valves

Plenum   Siren

Non-oscillating air   Oscillating air

Atomizer

Flow meter

Water tank

Air

Vacuum Pump
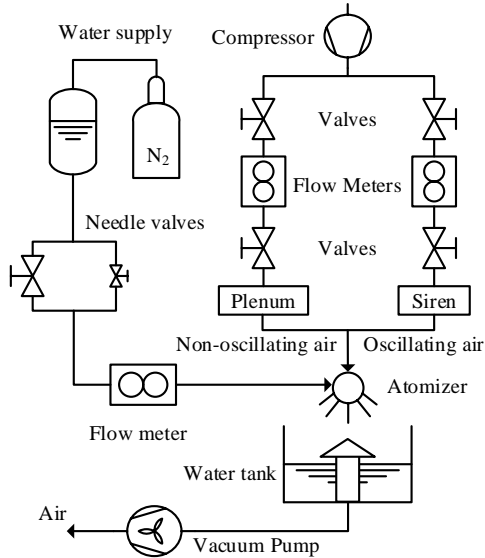
Figure 3.1: Experimental spray test rig schematic.

3.1.1   Main Test Facility Components

Airblast Prefilmer Model

The model prefilmer that was designed and manufactured for the research purposes of this project is shown in Figure 3.2. It consists of a standardized symmetrical airfoil profile (NACA-0010) made of stainless steel with a chord

length of 73 mm and a trailing edge thickness, i.e. an atomizing lip thickness of about 200 μm.
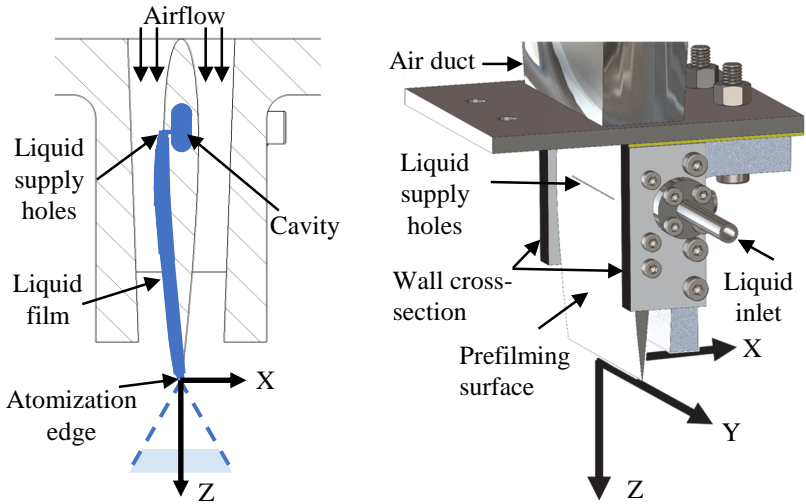
Figure 3.2: Schematic representation of the prefilming airblast atomizer model.
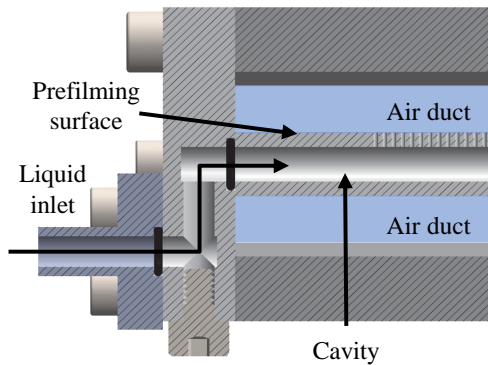
Figure 3.3: Cross-section of the model prefilmer, revealing the liquid inlet channel.

The water enters the cavity on the inside of the prefilmer symmetrically from the two sides (the cross-section for one side is shown in Figure 3.3) and flows through the 40 holes to emerge on the surface, creating a uniform thin film (the liquid film thickness on Figure 3.2 is exaggerated for illustration purposes). The air flows on both sides of the prefilming atomizer, while the liquid film covers only the one side, thus reproducing the prefilming surface of a conventional airblast atomizer. The area at which the air flows is determined by the curved surface of the prefilmer and the wall opposite to it, which has an inclination of 2°. As shown in Figure 3.4, the inclined wall transfers the location of the minimum duct area further downstream of the holes from where the liquid emerges on the surface.
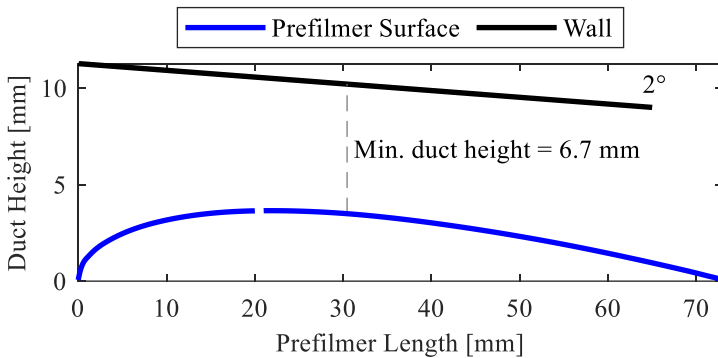
Figure 3.4: Profile of prefilmer surface and inclined wall determining the air duct height.

For planar model atomizers of this type, it is proposed in the literature to express the liquid flow rate in terms of film load $\dot{V}/b$, in units of mm²/s [103]; this implies the independence from the width of the liquid film b and the liquid's density ρ. The former has the effect of relating the flow rate to a two-

dimensional flow in one slice (of an infinitesimal depth Δx) of the prefilming surface, while the latter allows comparison with other types of liquid. In this way, as shown in Figure 3.5, the flow rate of the model prefilmer can be compared to a realistic design of an airblast atomizer.
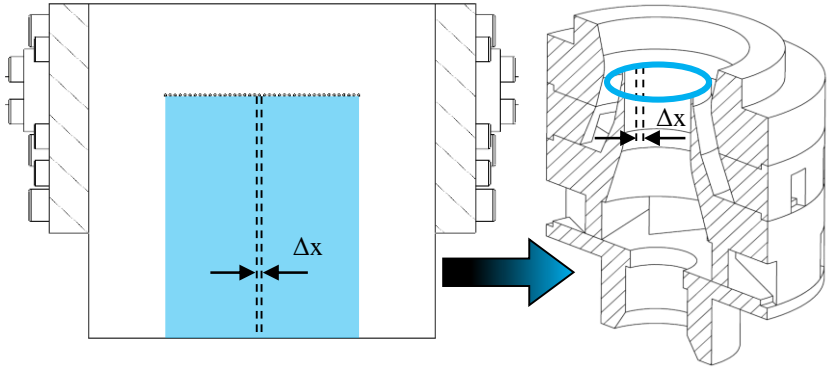
Figure 3.5: Comparison of model atomizer with typical airblast atomizer.

<u>Pulsating Device – Siren</u>

Part of the total air mass flow passes through the siren and is excited with a determined frequency. The siren used for air excitation shown in Figure 3.6 was designed and manufactured at the Technical University of Munich, Chair of Thermodynamics [125,126]. It consists of a housing with an internal rotating disc attached to a motor (Kollmorgen Seidel 6SM37M6000) whose rotational speed is controlled by computer software via a servo amplifier (Kollmorgen Servostar S600). The rotor and the fixed housing have eight and four openings respectively, through which the air can flow. As the rotor moves, when the openings of the rotor coincide with the openings of the stationary siren housing the air passes through, otherwise, the flow is interrupted.
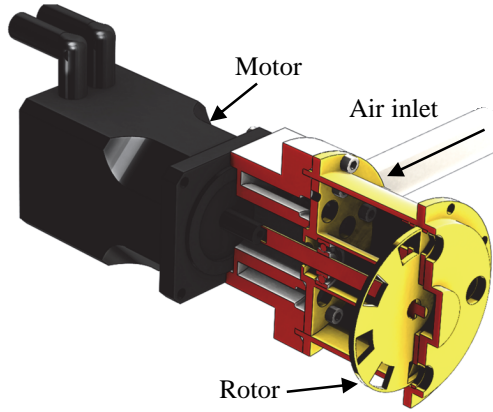
Figure 3.6: Siren configuration in cross-section.

Therefore, the air flows intermittently at an imposed frequency, which ideally is linearly dependent on the rotational speed of the motor:

$$f = \frac{8}{60} N \qquad (3.1)$$

where f is the frequency in Hz at which the air is allowed to pass through and N is the rotational speed of the motor in RPM, controlled by the software.

For the acceleration and deceleration of the motor, a time delay of 4 s was applied for a smoother transition from the current to the required rotational speed. A safety limit for the motor of 6,000 RPM was set, which corresponds to 800 Hz according to Eq.(3.1), high enough to study thermoacoustic phenomena typically occurring in frequencies of up to 500 Hz [14,127,128]. The motor is equipped with an incremental encoder, providing feedback regarding its rotational position. The encoder emits a binary signal with one pulse per revolution denoting its zero/reference position, and a second binary

signal with 1,024 pulses per revolution to indicate the current rotational position. These signals are utilized to correlate the measured spray data from different experiments on the same reference.
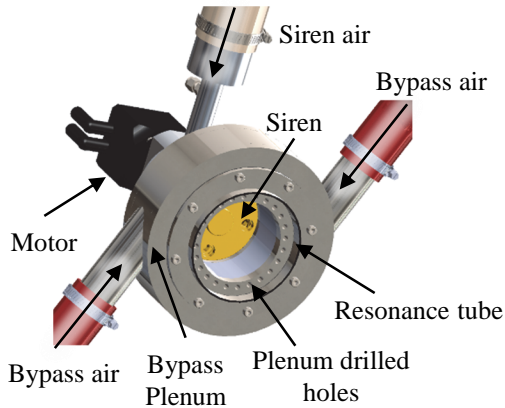
Figure 3.7: Configuration of siren and bypass plenum prior to the 1.5 m resonance tube and the airblast atomizer.

The rest of the total air mass flow passes through the bypass plenum. As shown in Figure 3.7, the air is inserted tangentially into the plenum through two tubes and then flows through 24 drilled holes co-axially with the siren and the resonance tube in order to mix with the pulsating flow coming from the siren. The inlet pipes for the bypass air were designed with a relatively large effective area (inner diameter of Ø39 mm) and holes with an optimum length-to-diameter ratio of two in order to maximize the discharge coefficient and thus minimize the pressure drop across the plenum.

3.1.2 Monitoring and Data Acquisition

The monitoring of the experimental setup, as well as the determination of the operating conditions in real-time, was accomplished by a LabVIEW program developed specifically for this purpose. All acquired signals for the measurement of pressure, temperature, and mass flow of air and water were transmitted from the corresponding measurement device to a proper for the signal National Instruments card housed on a four-card chassis (NI cDAQ-9174).
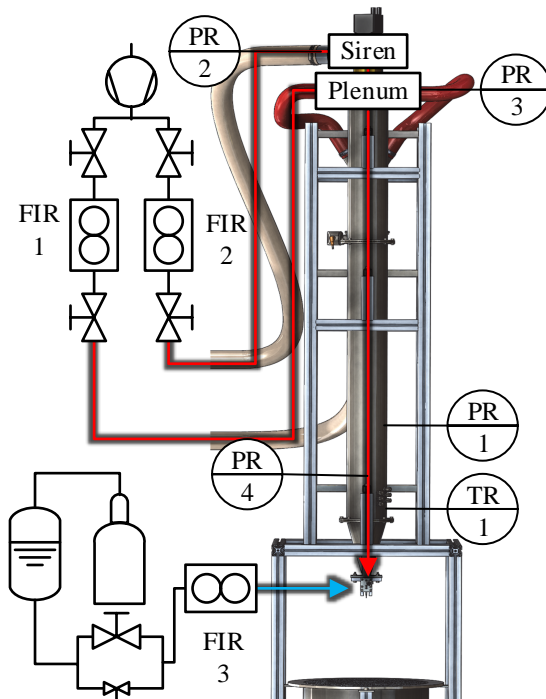
Figure 3.8: Flow chart of experimental setup and measurement instrument positions.

The schematic of the test facility with the measurement instruments and their positions is shown in Figure 3.8 in a P&ID format. The pressure is simultaneously acquired in four critical positions: upstream of the siren, inside the plenum, and twice upstream of the prefilmer model. Of the two pressure transducers placed upstream of the nozzle (PR-1 and PR-4); PR-1 is a differential sensor measuring the pressure at that location in comparison with the atmospheric, while PR-4 is an absolute pressure sensor. Combining the information acquired from the two of them, the atmospheric pressure at every instant was calculated, in order to correlate experiments at different occasions with different ambient conditions. For the same purpose, the type-K thermocouple (TR-1) was employed to measure the instantaneous temperature upstream of the nozzle. Incorporating all measurement instruments on the data acquisition chassis, the acquired signals provide the necessary information for the operation of the test facility, as illustrated in Figure 3.9.
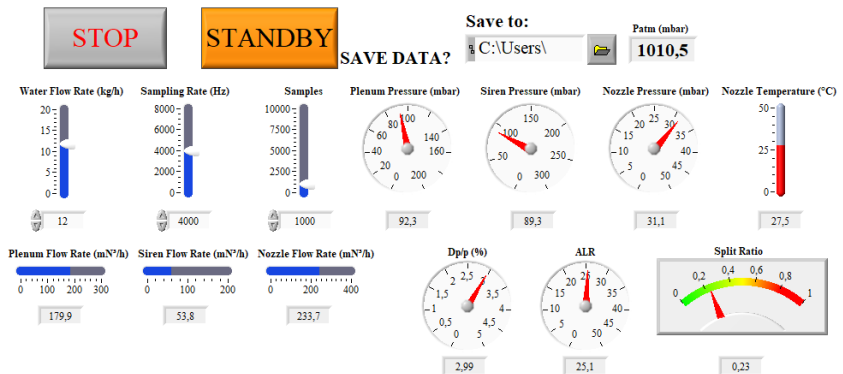
Figure 3.9: Front panel of the LabVIEW monitoring program with the test facility in operation.

3.2   Air Velocity Characterization

The investigation of the resulting airflow at the nozzle under the acoustic forcing after the mixing of the two streams from the siren and the plenum was done using hot-wire Constant Temperature Anemometry (CTA).

3.2.1   Hot-Wire Operating Principles

The measurement of a fluid's velocity via hot-wire anemometry is one of the most well-established methods since it allows not only the measurement of the time-averaged velocity but of the fluctuations as well. The operating principle of the hot-wire CTA technique lies in the heating of a thin metal wire, attached to the two protrusions of a probe, via an electric bridge circuit [129,130]. This setup is schematically shown in Figure 3.10.
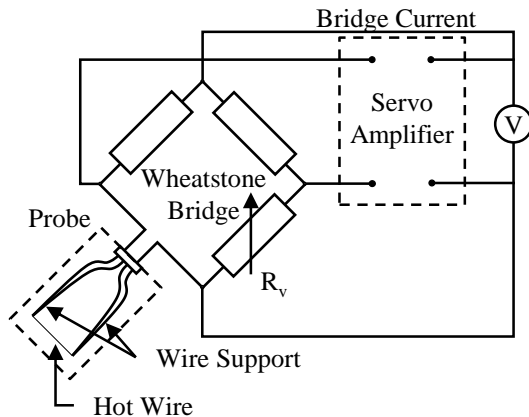
Figure 3.10: Schematic representation of the structure of a hot-wire Constant Temperature Anemometer circuit.

The temperature at which the wire is heated, T_S = 250 °C, is greater than the temperature of the fluid T_F. By controlling the resistance of the bridge R_V and thus the voltage on the bridge, the temperature T_S remains constant as the probe with the wire is inserted in the flow and heat is transferred from the wire to the fluid by convection. This relationship between the bridge voltage and the fluid's velocity was analysed by L. V. King [131] and expressed with the following equation:

$$E^2 = A + B \cdot u^{1/n} \qquad (3.2)$$

where A, B, and n are constants based on the calibration of the system, E is the bridge voltage, and u is the velocity of the fluid. This equation, commonly referred to as King's Law, is the basic equation on which a calibration of the measurement technique can be applied.

3.2.2 Calibration

Before measuring the airflow velocity on the spray setup to characterize its periodic oscillations generated by the siren, a calibration of the selected probe was necessary, i.e., the determination of the velocity-voltage curve using King's Law. A two-wire probe was employed (TSI 1247A-T1.5), with tungsten platinum-coated wires of 3.8 μm diameter and 1.27 mm length each. For this purpose, a calibration test rig was set up as displayed in the sketch diagram of Figure 3.11. A small compressor supplies the air in a duct and a nozzle is placed at its exit, designed with such a geometry in order to provide a bulk velocity profile at its exit [132,133]. The pressure difference between the point upstream of the nozzle and the atmosphere is measured with a differential pressure transducer (WIKA P-30), while the flow rate is measured with a volume flow meter (YOKOGAWA YEWFLO YF101). The

temperature of air at the nozzle is also measured using a commercial type-K thermocouple, in order to calculate its current density [130].
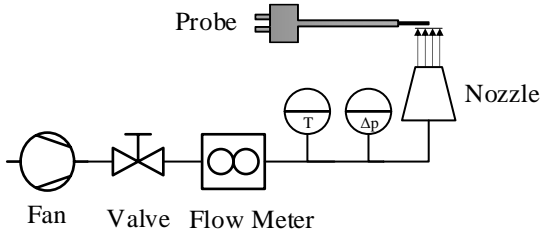
Figure 3.11: Sketch diagram of hot-wire CTA probe calibration setup.

The velocity at the exit of this nozzle can be accurately predicted with the use of the Bernoulli equation and the continuity equation [74,134]:

$$u = \sqrt{\frac{c \cdot 2 \cdot \Delta p}{\rho \cdot \left(1 - \left(\frac{A_2}{A_1}\right)^2\right)}} \qquad (3.3)$$

where Δp is the pressure difference across the nozzle as measured by the sensor, ρ is the density of air, A_2 and A_1 are the cross-sectional areas of the nozzle at its exit and entrance respectively, and c is an empirical coefficient that accounts for the friction and momentum losses based on the diameter ratio of the nozzle and the Reynolds number of the flow. For $D_1 = 45$ mm and $D_2 = 10$ mm, this coefficient is estimated $c = 0.98$ for a large range of Reynolds numbers [134].

The average bridge voltage is measured for the determined velocity calculated by Eq.(3.3). By varying the flow rate on the calibration setup and adjusting the velocity exiting the nozzle, a table of values for the bridge voltage and the

velocity can be established. This set of data displayed in a diagram (Figure 3.12) confirms that the King's Law is followed. Applying Eq.(3.2) to the data, the calibration constants are obtained.

Due to the expected shape of the calibration curve and the steeper and non-linear increase of voltage in the low velocities, more narrowly spaced calibration points were necessary in order to conclude to a curve that would fit the experimental data properly [135]. Inside the range of the examined velocities shown in Figure 3.12, i.e. between approximately 20 m/s and 100 m/s, the calibration curve following King's Law is reliable for measurements in the spray experimental setup.
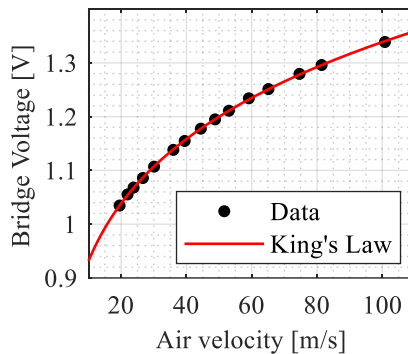
Figure 3.12: Calibration of the hot-wire probe using King's Law.

3.2.3 Application on the Experimental Setup

The two-wire probe was mounted on the translation stage of the experimental setup and connected to the CTA system. A high sampling rate of 40,000 Hz was selected for this application in order to safely identify the oscillations in

the 100-500 Hz order of magnitude, collecting approximately 525,000 samples for each measured position. Acquiring this amount of data with such a sampling rate, the measurement procedure for each position lasts approximately 13.1 s. A typical hot-wire CTA setup with a two-sensor probe is illustrated in Figure 3.13. The probe is connected to the Constant Temperature Anemometer (IFA-300), which through a BNC connector board transmits the acquired signal to the analog-to-digital converter attached to the PC of the system [135].
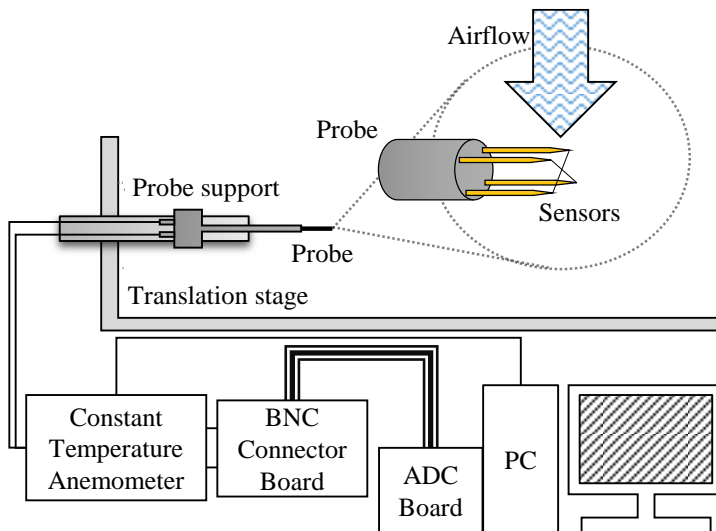
Figure 3.13: Schematic representation of the hot-wire CTA setup.

Since the air velocity is expected to oscillate periodically in time with a specific frequency, theoretically calculated in Eq.(3.1), a frequency domain analysis of the acquired signal was necessary to confirm it. For this purpose, the Fast Fourier Transform (FFT) was applied, which is the algorithm that computes

the discrete Fourier transform of a time series [136–138]. Applying a FFT on the acquired signal of the air velocity, it is possible to quantify the frequency and the amplitude of the oscillation. For the aforementioned measurement duration of approximately 13.1 s, the resolution of the determined frequency using FFT is 0.076 Hz.

3.3　Droplet Spray Characterization

The characterization of the spray implies the measurement of the basic properties of individual droplets included in the spray. These are the size and the velocity of the droplet. Two measurement techniques were set up for accomplishing this target: Phase Doppler Anemometry and Shadowgraphy. Both techniques are suitable for measuring the size and velocity of individual droplets in a spray, each with their respective advantages and disadvantages.

3.3.1　Phase Doppler Anemometry

One of the non-intrusive techniques for measuring particle sizes and velocities in two-phase flows is Phase Doppler Anemometry, a technique introduced, as an extension of the Laser Doppler Anemometry (LDA), by Durst and Zaré [139]. In LDA, one photo detector is used to measure the velocity of the particle, while in PDA the receiving system consists of two or three detectors in order to simultaneously measure the particle's velocity and diameter. The physical principle behind the two techniques is, as their name suggests, the Doppler Effect, which applies when there is a frequency shift in a signal due to a moving source or due to a moving observer. Most of the theoretical principles presented in section 3.3.1 are based on the books of Albrecht et al. and Ruck [140,141].

3.3.1.1   Velocity Measurement

The basic principle of a typical LDA system for the velocity measurement of a droplet is illustrated in Figure 3.14. In this reference system, the laser beams lie on the x-z plane with an intersection angle θ, while the photo detector is located in the x-y plane at an angle φ. The intersection of the two laser beams defines the measurement volume, the dimensions of which are described in section 3.3.1.3.
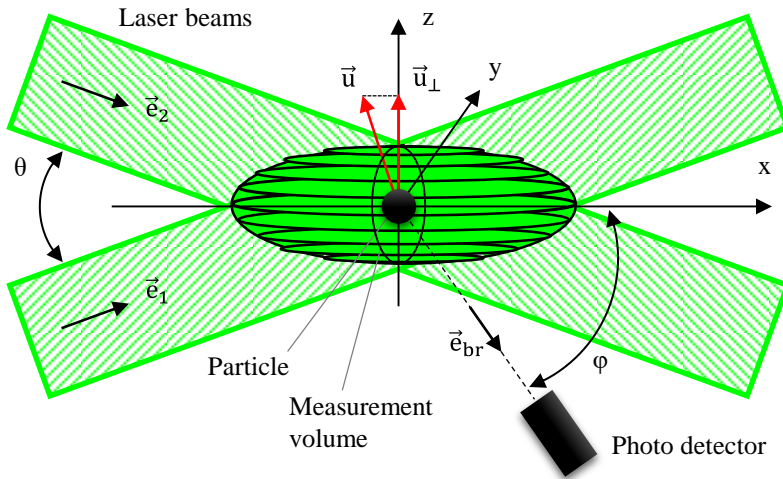
Figure 3.14: Optical configuration and measurement principle of the LDA system.

A particle crossing the measurement volume scatters light, which is collected by the photo detector. This signal is then correlated to the particle's velocity. The Doppler Effect occurs twice as the particle crosses the intersection of the laser beams. The first Doppler shift appears when the light of the laser beam (source) impinges on the moving particle:

$$f_p = f_b \left(1 - \frac{\vec{e}_b \vec{u}_p}{c} \right) \tag{3.4}$$

Where f_p is the frequency of the scattered light due to the moving particle, f_b is the frequency of the laser beam, $\vec{u}_p$ is the velocity of the particle, $\vec{e}_b$ is the unit vector of the incident laser beam, and c is the speed of light. The second Doppler shift occurs when the light scattered from the moving particle (source) is received by the stationary detector:

$$f_{br} = f_p \left(1 - \frac{\vec{e}_{br} \vec{u}_p}{c} \right)^{-1} \tag{3.5}$$

where f_{br} is the frequency detected by the receiving optics and $\vec{e}_{br}$ the unit vector of the scattered light, originating from laser beam b, in the direction of the receiving optics. With the assumption that $|\vec{u}_p| \ll c$, combining the aforementioned equations of the two Doppler shifts, f_{br} can be approximated as:

$$f_{br} \approx f_b \left(1 + \frac{\vec{u}_p (\vec{e}_{br} - \vec{e}_b)}{c} \right) \tag{3.6}$$

The frequency detected by the receiving optics originates from two waves scattered by the moving particle due to the two laser beams. This frequency difference $\Delta f = f_D$, called the Doppler frequency is acquired in the detector when the two waves, of frequencies f_{1r} and f_{2r}, interfere on the surface of the detector lens:

$$\Delta f = f_D = f_{2r} - f_{1r} = f_2 - f_1 - \frac{f_2}{c} \vec{u}_p \vec{e}_2 + \frac{f_1}{c} \vec{u}_p \vec{e}_1 \tag{3.7}$$

For laser beams of the same frequency ($f_1 = f_2 = c/\lambda$), the Doppler frequency Eq.(3.7) becomes:

$$f_D = \frac{2\sin(\theta/2)}{\lambda} u_{p\perp} \tag{3.8}$$

where λ is the wavelength of the laser beams and $u_{p\perp}$ is the particle velocity component perpendicular to the x-y plane, since $\vec{e}_1 - \vec{e}_2 = 2\sin(\theta/2)\,\vec{e}_x$. The drawback of this relationship between the Doppler frequency and the velocity of the particle, as shown in Figure 3.15(a), is that the same frequency corresponds to two different velocity values one opposite of the other. The solution arises by shifting the frequency of one of the laser beams $f_2 = f_1 + f_{shift}$, so Eq.(3.7) becomes:

$$f_D = f_{shift} - \frac{f_{shift}}{c}\vec{u}_p\vec{e}_2 + \frac{f_1}{c}\vec{u}_p(\vec{e}_1 - \vec{e}_2) \tag{3.9}$$

Since $|\vec{e}_1 - \vec{e}_2| > 0$ and $f_1 \gg f_{shift}$, Eq.(3.9) becomes:

$$f_D = f_{shift} + \frac{2\sin(\theta/2)}{\lambda} u_{p\perp} \tag{3.10}$$
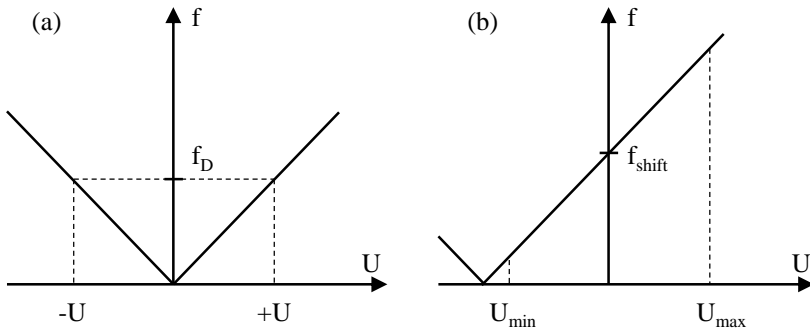
Figure 3.15: Velocity-frequency linear relationship: (a) without a frequency shift and (b) with a frequency shift.

As seen in Figure 3.15(b), with this frequency shift, usually $f_{shift} = 40$ MHz realized by a Bragg cell, each frequency detected is correlated in a one-to-one way to each velocity in the measurement span. Negative velocities are also measured when the Doppler frequency is below the shift frequency, while positive occur for frequencies higher than the shift.

The particle's velocity component perpendicular to the x-y plane is finally calculated:

$$u_{p\perp} = \frac{\lambda}{2\sin(\theta/2)}(f_D - f_{shift})$$

(3.11)

3.3.1.2   Diameter Measurement

To determine the size of homogeneous spherical particles, the supplement provided to the typical LDA technique is the addition of a second photo detector, as shown in Figure 3.16. The transmitting optics of the PDA system are identical to those used in LDA, where the laser beams intersect with an angle θ, creating the measurement volume. The two photo detectors U_1, and U_2, are placed at elevation angles ψ_1, ψ_2 (or $\pm\psi$), while the receiving optics arrangement hosting the detectors lies at an off-axis angle φ. The two photo detectors identify the same Doppler frequency when a particle crosses the measurement volume. On the other hand, the signal arrives at the two detectors as it interferes on their surface with a slight phase shift (Figure 3.17), due to the different lengths the scattered light travels to reach each detector.
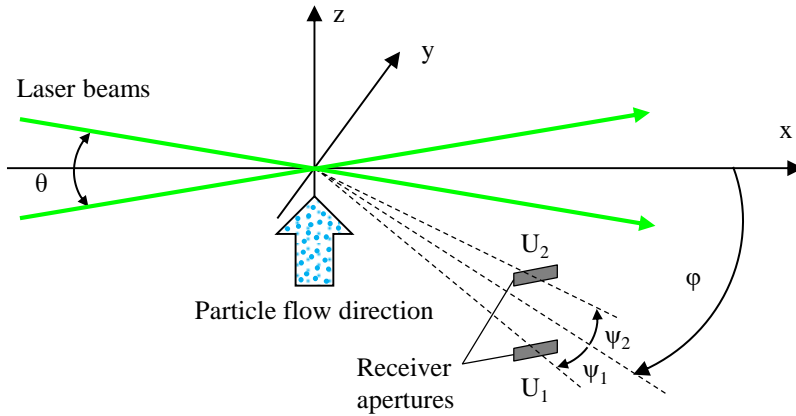
Figure 3.16: Optical configuration of the typical two-detector PDA system.
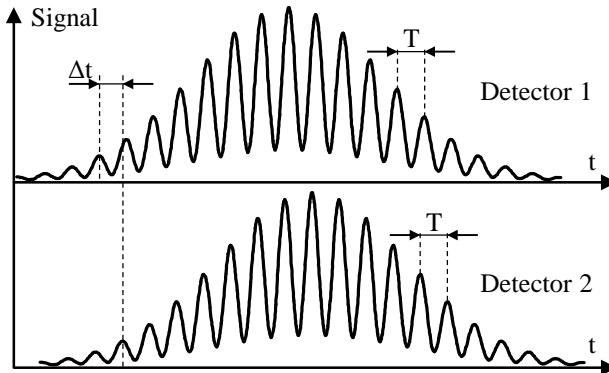
Figure 3.17: Phase shift of the Doppler signal from the two photo detectors.

This shift is proportional to the time difference of the two detected signals:

$$\Delta\Phi_{12} = 2\pi\frac{\Delta t}{T} \tag{3.12}$$

where Δt is the time difference between the signals acquired at the two detectors and T is the period of the Doppler signal. To identify this phase shift and correlate it to the particle diameter, the geometry of the incident beams on the particle, as shown in Figure 3.18, should be examined. A reference beam I' is considered, as well as another incident beam I for the cases of reflection and first-order refraction, illustrated in Figure 3.18(a) and (b) respectively. The phase difference δ relative to the reference beam I' originates from the difference in the path length between the segments AB and A'UB'. For the case of reflection, the length of the path A'UB' is:

$$|A'UB'| = d_p \sin \gamma$$

(3.13)

where d_p is the diameter of the particle and γ is the angle between the incident beam I and the tangent to the particle surface at the point of incidence A.
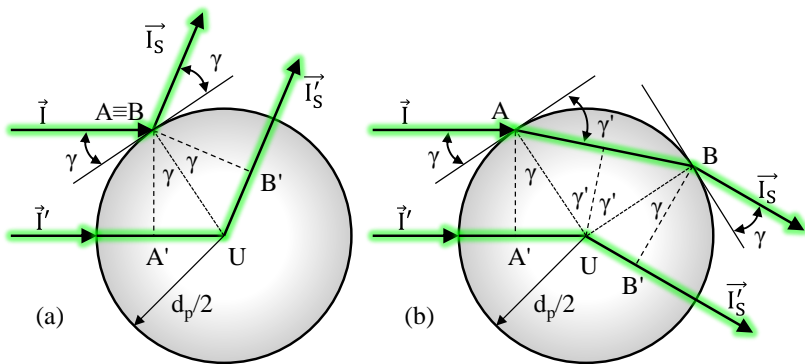
Figure 3.18: Phase shift of the signal acquired by the photo detectors due to the path length difference through the particle in case of (a) reflection and (a) first-order refraction.

In the case of reflection, there is no line segment AB since the two points coincide. By exploiting the relationship between the path difference and the phase difference [142]:

$$\frac{\delta}{2\pi} = \frac{d_p \sin\gamma}{\lambda_M}$$

(3.14)

where δ is the phase difference of the beam I relative to the reference beam I' and λ_M is the wavelength of the beam in the medium. The wavelength in the medium λ_M is linked to the wavelength in vacuum λ_0 via the refractive index of the medium n_M:

$$\lambda_M = \frac{\lambda_0}{n_M}$$

(3.15)

Therefore, the phase shift can be expressed as:

$$\delta = \frac{2\pi}{\lambda_0} n_M d_p \sin\gamma = k n_M d_p \sin\gamma$$

(3.16)

where k is the wave number:

$$k = \frac{2\pi}{\lambda_0}$$

(3.17)

Similarly, for the first-order refraction, the phase shift becomes:

$$\delta = \frac{2\pi}{\lambda_0} n_M d_p (\sin\gamma - n_{rel} \sin\gamma')$$

(3.18)

where n_{rel} is the relative refraction index between the medium and the particle and γ' is the angle between the line segment AB and the tangent to the particle surface at the point of incidence A. Generally, for the i-th order refraction:

$$\delta = \frac{2\pi}{\lambda_0} n_M d_p (\sin \gamma - i \cdot n_{rel} \sin \gamma') \qquad (3.19)$$

The receiving optics are placed in an off-axis angle φ relative to the x-axis, while the two photo detectors are elevated in angles ±ψ from the x-y plane. Due to symmetry, for the phase difference relative to the reference beam applies:

$$\delta_1 = -\delta_2 \qquad (3.20)$$

Therefore, from Eq.(3.16) for reflection the phase shift $\Delta\Phi_{12}$ becomes:

$$\Delta\Phi_{12}^{(1)} = \frac{2\pi}{\lambda_0} n_M d_p \, 2\sin\gamma = \frac{2\pi}{\lambda_0} n_M d_p b^{(1)} \qquad (3.21)$$

while for first order refraction, from Eq.(3.18), the phase shift is:

$$\Delta\Phi_{12}^{(2)} = \frac{2\pi}{\lambda_0} n_M d_p (\sin\gamma - n_{rel}\sin\gamma') = \frac{2\pi}{\lambda_0} n_M d_p b^{(2)} \qquad (3.22)$$

If calculated for the global system coordinates of Figure 3.16, the scattered light term for reflection results in:

$$b^{(1)} = \sqrt{2}\left(\sqrt{1 - \cos\psi\cos\varphi\cos\frac{\theta}{2} + \sin\psi\sin\frac{\theta}{2}}\right.$$
$$\left. - \sqrt{1 - \cos\psi\cos\varphi\cos\frac{\theta}{2} - \sin\psi\sin\frac{\theta}{2}}\right) \tag{3.23}$$

and for first-order refraction:

$$b^{(2)} =$$
$$2\left(\sqrt{1 + n_{rel}^2 - n_{rel}\sqrt{2}\sqrt{1 + \cos\psi\cos\varphi\cos\frac{\theta}{2} + \sin\psi\sin\frac{\theta}{2}}}\right.$$
$$\left. - \sqrt{1 + n_{rel}^2 - n_{rel}\sqrt{2}\sqrt{1 + \cos\psi\cos\varphi\cos\frac{\theta}{2} - \sin\psi\sin\frac{\theta}{2}}}\right) \tag{3.24}$$

Therefore, the diameter of the particle is calculated linearly to the phase difference between the two detectors:

$$\Delta\Phi_{12}^{(I)} = \frac{2\pi}{\lambda_M}b^{(I)} \cdot d_p \tag{3.25}$$

$$d_p = \frac{\lambda_M}{2\pi}\frac{1}{b^{(I)}} \cdot \Delta\Phi_{12}^{(I)} \tag{3.26}$$

The two-detector PDA system is restricted in a limited range of particle diameters because it can only determine a phase shift up to 2π. As illustrated in Figure 3.19, a higher phase difference is observed in the signal when a larger

particle is detected. However, if the particle has a large enough diameter, the phase difference exceeds the value of 2π; this leads to a misconception of the real particle diameter, so an incorrect value is assigned.
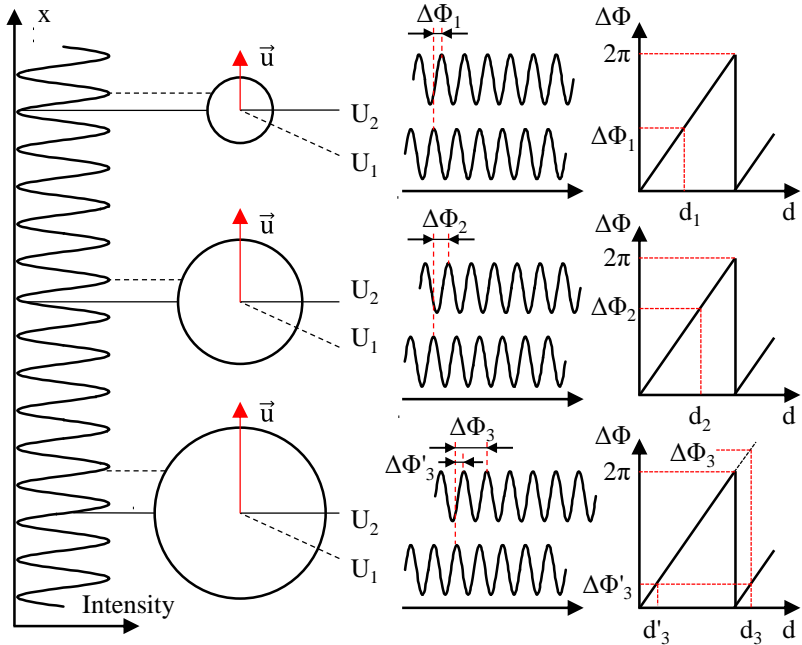
Figure 3.19: Two-detector system 2π-ambiguity.

This 2π ambiguity is overcome by setting a three-detector PDA system, as shown in Figure 3.20. With this setup, three phase differences are measured for each detected particle; $\Delta\Phi_{12}$ between detectors U_1 and U_2, $\Delta\Phi_{13}$ between detectors U_1 and U_3, and $\Delta\Phi_{23}$ between detectors U_2 and U_3. The difference in the elevation angles of the three detectors yields separate phase differences and thus particle diameters. The detectors U_1 and U_2 that are placed at steeper

elevation angles measure a phase difference that leads to more accurate diameter measurement compared to the closely spaced detector pair U_1 and U_3, which measures in a larger size range.
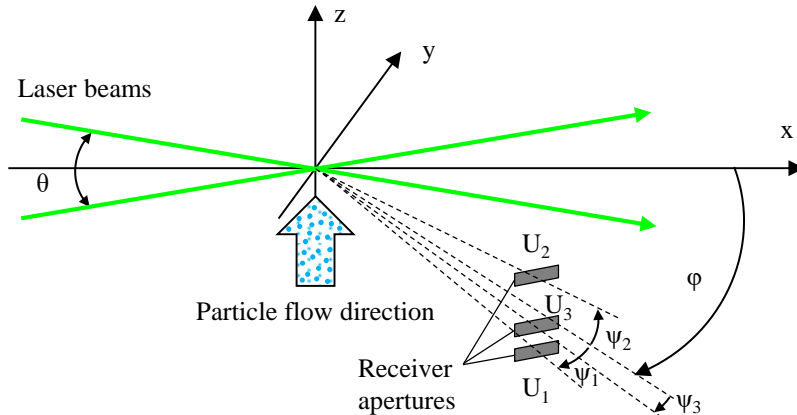
Figure 3.20: Optical configuration of the typical three-detector PDA system.

As shown in Figure 3.21, the phase difference $\Delta\Phi_{12}$ corresponds to multiple particle diameters, while only one of them matches the phase difference $\Delta\Phi_{13}$ as well.

The diameter measured via the phase differences of the detector pairs refers to a curvature of the particle surface. Since all detectors on a standard three-detector PDA system lie on the same off-axis angle, the detector pairs measure approximately the same curvature on a meridian line over the particle surface, as illustrated in Figure 3.22(a). In the case of a perfectly spherical particle, $\Delta\Phi_{12}$ and $\Delta\Phi_{13}$ result in the same particle diameter as shown in Figure 3.21(b). However, if the two curvatures slightly diverge, then $\Delta\Phi_{12}$ and $\Delta\Phi_{13}$ lead to diameter measurements with a difference of Δd_p as shown in Figure 3.22(b).

This divergence of the measured diameter is used as a sphericity criterion in order to consider only near perfectly spherical particles.
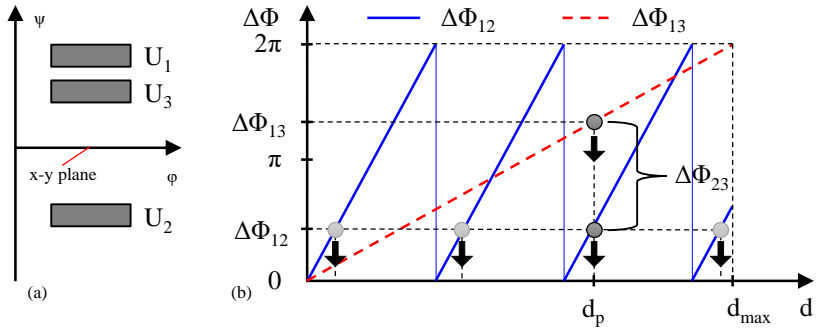
Figure 3.21: (a) Elevation angles of the three detectors. (b) Phase difference - diameter relationship of the three detector system to overcome the 2π ambiguity.
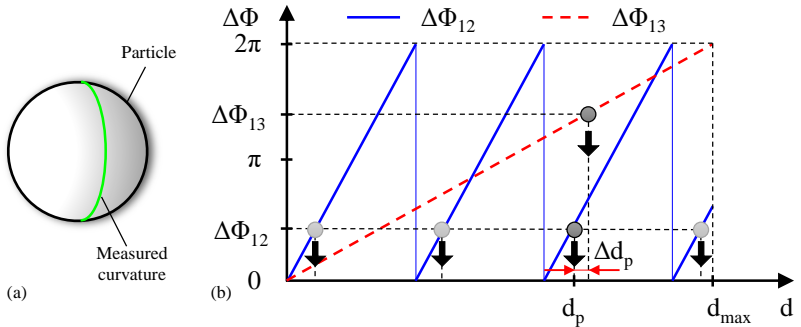
Figure 3.22: (a) Measured curvature on the meridian of the particle. (b) Sphericity validation of particle based on the diameter difference Δd_p as an outcome of the values of $\Delta\Phi_{12}$ and $\Delta\Phi_{13}$.

73

3.3.1.3 Measurement Volume Size Calculation

As shown in Figure 3.14, measurements take place in the intersection between the two incident laser beams. This measurement volume is an ellipsoid, with its dimensions illustrated in Figure 3.23.
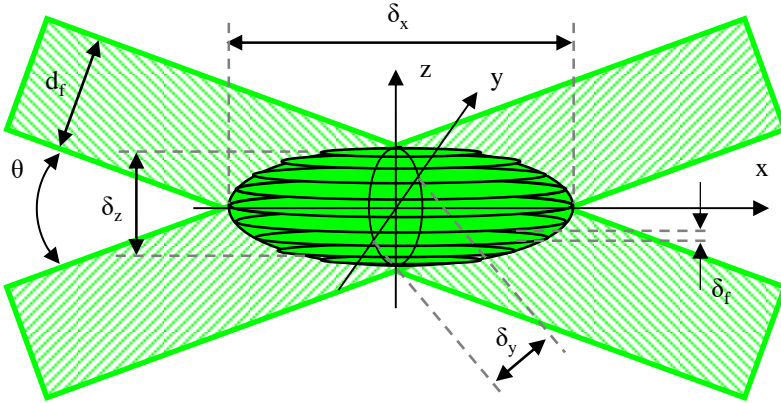
Figure 3.23: The measurement volume.

The fringe spacing δ_f, which is the distance between the individual interference fringes, was already subtly involved in the particle velocity – Doppler frequency correlation of Eq.(3.11). It depends on the intersection angle θ and the wavelength of the laser beam λ:

$$\delta_f = \frac{\lambda}{\sin(\theta/2)} \tag{3.27}$$

The beam waist diameter d_f, which is the diameter of the focused laser beam, is a function of the focal length f, the wavelength of the laser beam λ, the beam expansion factor E, and the laser beam diameter at its origin d_L:

$$d_f = \frac{4f\lambda}{\pi E d_L}$$

(3.28)

The size of the measurement volume can be calculated from the beam waist diameter d_f and the intersection angle θ:

$$\delta_x = \frac{d_f}{\sin(\theta/2)}, \qquad \delta_y = d_f, \qquad \delta_z = \frac{d_f}{\cos(\theta/2)}$$

(3.29)

The total number of fringes can be calculated from the height of the measurement volume d_z and the fringe spacing δ_f:

$$N_f = \frac{\delta_z}{\delta_f} = \frac{2d_f}{\lambda}\tan(\theta/2)$$

(3.30)

3.3.1.4 Mass Flux Calculation

The basic issue that needs to be addressed is the definition of a cross-sectional area as a reference for the particle detection. Several factors influence the effective area of detection illustrated in Figure 3.24.
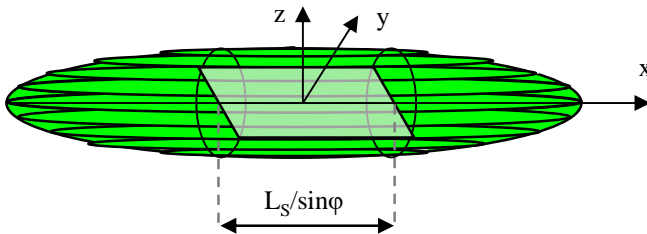
Figure 3.24: Theoretical measurement volume (ellipsoid) and effective area of detection.

These factors are the beam waist diameter d_f, the scattering angle φ (s. Figure 3.20) as well as the width of the slit aperture L_S. However, three further factors are of importance as well; the particle size, the particle trajectory, and the validation criteria.

Dependence of detection area on particle size

The effect of a larger effective measurement volume for larger particles was introduced by Saffman [143]. The algorithm proposed by Saffman considers particle trajectories along the z-axis on the y-z plane of Figure 3.24.
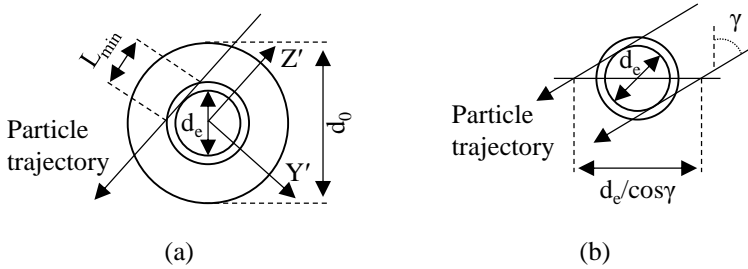
Figure 3.25: Effective detection area perpendicular to the z-axis.

The effective area measurement is based on the concept of an effective measurement volume diameter d_e shown in Figure 3.25(a), which depends on the particle size. Knowing this size, the cross-sectional areas are calculated:

$$A_z(d_i) = d_e(d_i) \frac{L_S}{\sin \varphi} \tag{3.31}$$

$$A_y(d_i) = d_e(d_i) \frac{L_S}{\sin \varphi} + \frac{\pi}{4} d_e^2 \cot \varphi \tag{3.32}$$

Dependence of detection area on particle trajectory

When measuring the particle size, concentration, or mass flux, the number of detected particles is always measured in relation to a reference cross-sectional area. For particle trajectories in the z or y direction, the reference areas are A_z and A_y. However, when particles travel in a different trajectory on the y-z plane, then this effective area changes relatively to the detection of the particle. This is illustrated in Figure 3.25(b) for the reference area perpendicular to the z-coordinate. This effective area is defined specifically for the particles that cross the detection boundary d_e. Applying the same for the area perpendicular to the y-direction:

$$A_z' = \frac{A_z}{\cos\gamma} = \frac{L_S \cdot d_e}{\cos\varphi \cdot \cos\gamma} \tag{3.33}$$

$$A_y' = \frac{A_y}{\sin\gamma} = \frac{L_S \cdot d_e}{\sin\varphi \cdot \sin\gamma} + \frac{\frac{\pi}{4} d_e^2 \cot\varphi}{\sin\gamma} \tag{3.34}$$

where the angle γ is dependent only on the measured velocity components:

$$\gamma = \tan^{-1}\frac{v}{u} \tag{3.35}$$

Dependence of detection area on validation criteria

The reference detection area is finally also influenced by the validation routine. The validation ensures the rejection of particles that cross the measurement volume and reflect light instead of refracting it. Thus, the rejection of particles crossing the detection area of the measurement volume is reduced. This reduction is dependent on the particle size, the refraction index, and the particle

trajectory. To reduce the probability of having multiple particles simultaneously inside the measurement volume, a limit is imposed on the detector optic by using a slit of appropriate length.

Having established the effective detection area of each direction and how it is influenced, the mass flux can be calculated for each direction based on the corresponding velocity component.

$$\dot{m}_z'' = \rho_P \frac{\pi}{6\Delta t} \sum_{i=1}^{N} \frac{d_i^3 \cdot \cos \gamma_i}{A_z} \tag{3.36}$$

$$\dot{m}_y'' = \rho_P \frac{\pi}{6\Delta t} \sum_{i=1}^{N} \frac{d_i^3 \cdot \sin \gamma_i}{A_y} \tag{3.37}$$

where ρ_P, d_i, and γ_i are the particle density, diameter, and trajectory angle respectively. The detailed steps of the algorithm are described in Appendix A

3.3.2   Shadowgraphy

Another non-intrusive technique for characterizing a spray of particles in terms of size and velocity is Shadowgraphy imaging. The phenomenon was first observed by R. Hooke in the 17th century [144] and was later adapted into a solid, coherent measurement technique [145].

3.3.2.1   Measuring Principle

The measuring principle of the technique is based on the pulsating backlight illumination of particles travelling through the field of view of the focal plane, with an imaging system capturing their shadows. In Figure 3.26 the basic

arrangement of a shadowgraphy setup is illustrated, with a camera aligned to the illumination source and the focal plane at the centre. The camera can be attached to a long-distance microscope in order to focus on a small field of view, while the illumination source usually consists of a laser and a high-efficiency diffuser [146].
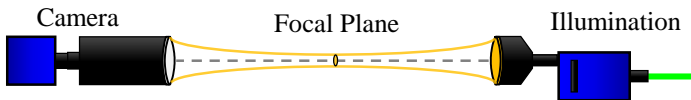
Figure 3.26: Generic setup of the shadowgraphy imaging measurement technique.

The long-distance microscope operates with the principle shown in Figure 3.27. Light passes through the front correcting lens and is refracted directly in the primary mirror at the back of the microscope. The light is then reflected in the front section's secondary mirror and sent back to the prism via a tube supported in the primary mirror's centre hole. As a result, the picture that reaches the camera's axial port gets amplified in size. Long-distance microscopes of this type can measure particles with a diameter of 5 to 100 μm.
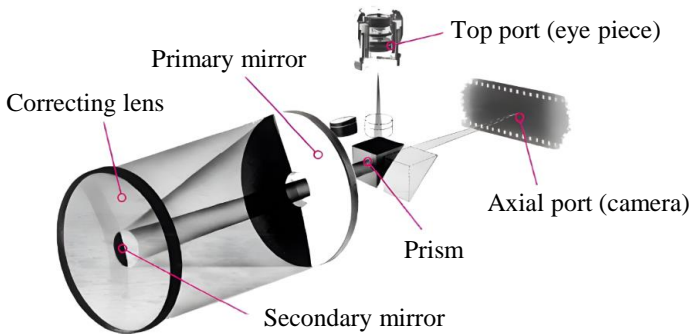
Figure 3.27: Operating principle of the long-distance microscope [146].

A scale imprinted on a transparent plate as seen in Figure 3.28 is used to calibrate the size on the obtained pictures. A 5 mm distance is split into 200 lines on this plate, with the lowest distance between lines being 25 μm. The scaling plate is placed at the focal plane in the field of view to be used as a reference for providing size information on the captured images.
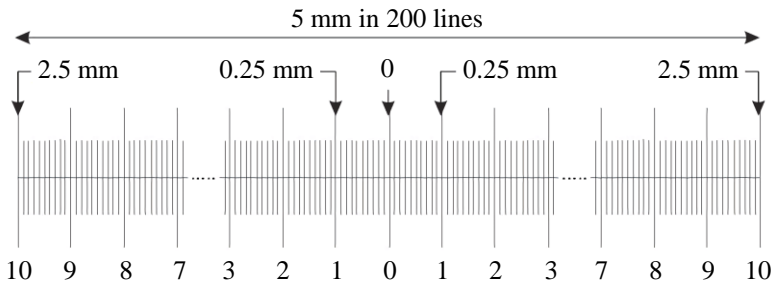
Figure 3.28: Scaling plate of shadowgraphy system [146].

3.3.2.2 Preliminary Image Processing

The captured images are subject to a preliminary processing to normalize their intensity since images may have a different total or local intensity based on the particle flow at each instant. Particles that are far outside of the focus plane appear on the picture as diffuse shadows, therefore the image intensity is locally affected. The intensity normalization process involves adjusting the entire image's intensity to a reference value. The latter is accomplished by using a sliding maximum, which specifies the search radius in pixels, and the processing software generates a reference image based on this as seen in Figure 3.29. The original raw image's local intensity is then divided by the reference

image's intensity, yielding a new normalized image that may be used for the particle identification and further processing.

The effect of various normalizing radius examples is displayed in Figure 3.29. As shown with the red curve, the varied local intensities are not clearly separated, and the diffuse particles are not resolved, when the raw picture is normalized with a single value of the total intensity. It is clear, especially when small diffuse structures are near large particles, that the low intensity of this region would be misidentified as one large structure, introducing an inaccuracy in spray characteristic prediction. The intensity of small-scale characteristics is increased as the normalization radius is reduced as shown in the examples with the blue and green curves.
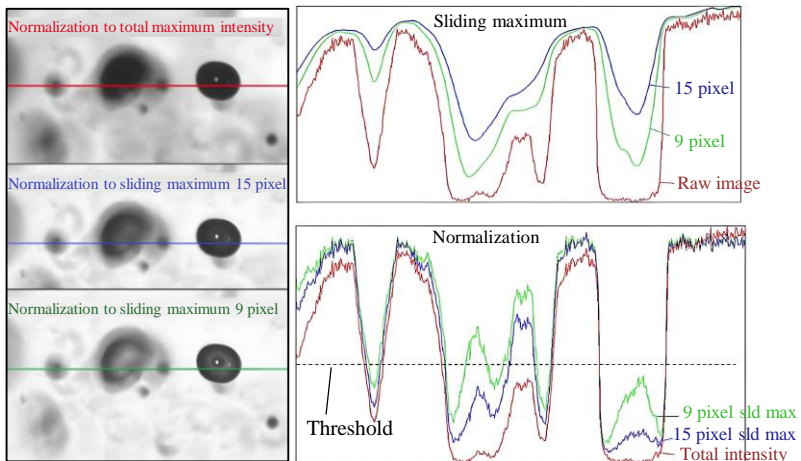
Figure 3.29: Image intensity normalization using a sliding maximum [146].

After the intensity normalization, each captured image includes regions with high local intensity values on the scale of 0 to 100%, as well as regions with

low-intensity values on that scale, denoting the appearance of particles. To ultimately determine when a region of the image contains a particle or not, based on the local intensity values, a binarization threshold must be selected. This threshold to binarize a grayscale image into a black-and-white image is usually selected based on the method developed by Otsu [147,148].

The second parameter in the preliminary processing of the images is the minimum shadow area, which denotes the necessary number of pixels on a shape on the image after binarization in order to consider the given shape as a particle. Extremely low values on this parameter may lead to a false interpretation of random noise on the image as particles, while high values would reject the small particles existing on the image.

Finally, the third parameter of this pre-processing is the minimum intensity slope. The gradient of the intensity from each pixel to its neighbouring pixels on the grayscale image denotes the change in the intensity value. Low values of that slope indicate that the intensity does not significantly vary between the neighbouring pixels. A high slope, however, denotes a rapid change in intensity, indicating the existence of a particle. The higher this gradient value, the sharper the detected particle on the image. This can be visualized in Figure 3.29 where the sharpness of each droplet along the coloured horizontal line on the photos on the left can be correlated to the slope of the corresponding plotted lines in the graphs on the right. Setting a minimum threshold on that intensity slope excludes extremely blurry particles that are located far from the focal plane but are still leaving their shadow on the captured image.

3.3.2.3 Diameter and Velocity Measurement

Having established the pre-processing of the images, the software is able to identify the particles and proceed to calculate their characteristics. The particle area is defined as the region encompassed by the identified particle rim, as illustrated in Figure 3.30(a). An ellipse is then fit to the particle area as shown in Figure 3.30(b), whose long and short axis deviation is a measure of the particle's sphericity. The coordinates of the centroid, which can be used to track the particle's position in space, are calculated as the geometric centre of the detected particle area. Finally, the equivalent particle diameter is calculated as the diameter of a circle with the same area as the one detected.
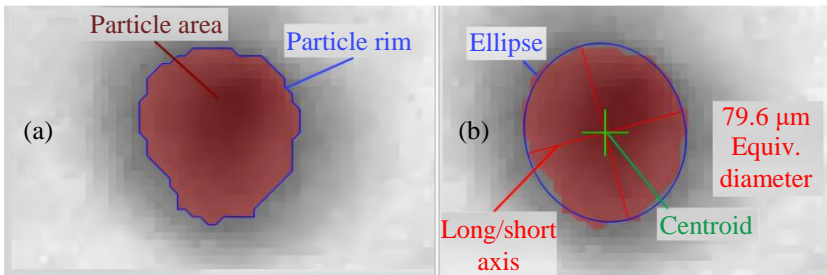
Figure 3.30: Fundamental processing: (a) particle recognition and (b) derived values [146].

Since the geometric characteristics of the particle have been completely identified, its velocity can then be calculated. The way the velocity is calculated is similar to the measurement technique of Particle Image Velocimetry (PIV), with the difference that here the velocity of each single particle is determined instead of a collection of particles [149]. This is possible when the illumination source and the camera of the setup illustrated in Figure

3.26 are double-pulsed and double-frame respectively. The illumination source emits two pulses with a time interval of a few μs between them and the camera is synchronized and captures two frames with the same time difference. These two images are called sibling images in this context, where Frame A is the first and Frame B is the second. Since the time interval between these two frames is determined and the coordinates of each particle on both frames are analysed, the velocity of that particle can be calculated. However, the challenge is to identify which particle of Frame B corresponds to which particle of Frame A.

This identification process is illustrated in Figure 3.31. Two basic parameters are used in order to overcome this challenge and identify the sibling particle of Frame B which corresponds to the original particle of Frame A.
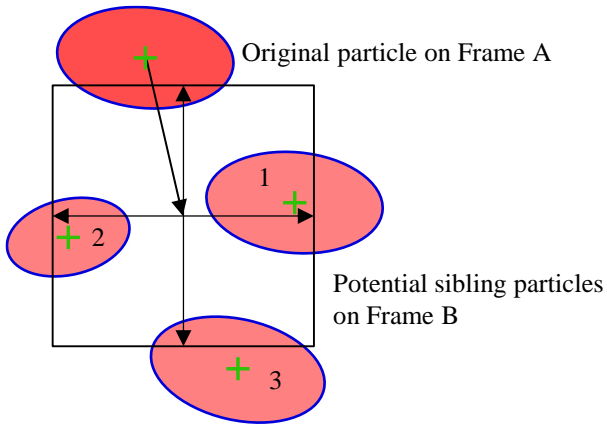
Figure 3.31: Investigation of a sibling particle in a determined radius from the original particle [146].

The most important is to set the expected velocity of the particle for both components on the plane, with a maximum expected deviation from that velocity. This determines a search area, inside of which the centroid of the

sibling particle in Frame B must exist. As shown in the example of Figure 3.31, the potential siblings numbered 1 and 2 are inside this search area depicted as a box, while particle 3 is not and therefore excluded. The second parameter is the expected size deviation of the original particle as it moves. This is a restriction to exclude all particles that are inside the search area but their size is significantly different than the original particle of Frame A. In this example, particle 2 would be excluded based on a restriction for a maximum allowed size deviation, so particle 1 has to be the sibling of the original particle. Therefore, the distance of the centroids between the two sibling particles is used to determine the particle's velocity.

3.3.2.4   Size Correction

Based on the premise of a homogeneously distributed sample in 3D space, the disclosure of statistical figures by the software is possible. This indicates that the probability of detecting a specific particle within a certain size range is the same over the whole sample volume. The technique encompasses a bias that varies with particle size. This indicates that smaller and bigger particles are not detected with the same probability, even when they are homogeneously dispersed with the same number density (particles per volume unit).

A size-dependent bias is caused by two factors that modify the detection probability:

- **Border effect**: Larger particles are more likely to touch the image's rim, resulting in a lower effective field-of-view size.
- **Depth-of-field (DOF) effect**: Larger particles are detected from a bigger depth than smaller particles, leading to a deeper detection volume.

When calculating statistic values, both effects are addressed in such a way that each particle is weighted and not treated as equal to all other particles. The statistical weight of a particle compensates for differences in detection likelihood (bias). It is the inverse of the probability of being detected:

$$sw = sw_{border} \cdot sw_{DOF} = \frac{1}{p_{border}} \frac{1}{p_{DOF}} \tag{3.38}$$

where sw is the total statistical weight, sw_{border} and sw_{DOF} are the statistical weights to compensate for the border and DOF effects respectively, while p_{border} and p_{DOF} are the probabilities of a particle to be detected, biased by the border and the DOF effect respectively.

The border correction decreases the probability of bigger particles being identified by compensating for the size-dependent probability of contacting or intersecting the image border. The effective field of view of a camera picture can be used to represent a particle's effective detection area. For a spherical particle with a diameter of d in a field of vision region of width w and height h as illustrated in the sketch of Figure 3.32, the statistical weight sw is determined as follows:

$$sw_{border} = \frac{w \cdot h}{(w - d)(h - d)} \tag{3.39}$$

Smaller particles are detected from a smaller sample volume, while larger particles are detected from a deeper sample volume. Assuming that the depth of field is proportional to the particle diameter, the DOF effect can be compensated for. The statistical weight of a particle of diameter d cannot be represented in absolute terms; instead, it must be expressed in terms of a

reference particle of size d_{ref}. The value for d_{ref} in the ParticleMaster software is hard-coded to 100 μm.

$$sw_{DOF} = \frac{d_{ref}}{d} \tag{3.40}$$
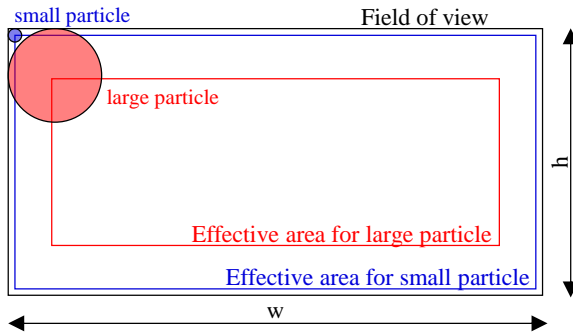
Figure 3.32: Effective area of particle detection on the field of view for different particle sizes [146].
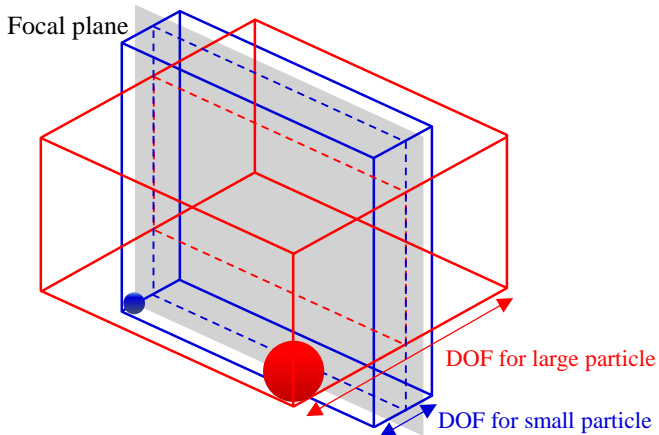
Figure 3.33: Depth of field correction for detection of different particle sizes [146].

3.3.3   Application on the Experimental Setup

3.3.3.1   Phase Doppler Anemometry

For this work, a 2D Fiber PDA system in first-order refraction mode was utilized, in a setup with a three-detector receiving optic at a scattering angle of 30°. A DPSS laser was used, providing laser beams in the wavelengths of 532 nm (green) and 561 nm (yellow). Comparing the model atomizer to the real airblast atomizer as shown in Figure 3.5, the velocity component parallel to the Z-axis of Figure 3.2 corresponds to the axial velocity, while the component parallel to the X-axis of Figure 3.2 corresponds to the radial velocity. The axial velocity component and the droplet diameter measurements were accomplished with the green laser light, while for the measurement of the radial component of the droplet velocity the yellow one was used. Lenses with a focal length of 500 mm were used for both the sending and receiving fiber optics. Considering the wavelength of the laser beams, the beam spacing, and their intersection angle, this setup configuration generates an ellipsoid measurement volume with a diameter of approximately 154 μm and a length of approximately 2.7 mm, which allows measurement for droplet diameters up to 300 μm.

This setup configuration involves an effective spatial filter width of 0.4 mm, phase factors of 2.212 °/μm and 0.8679 °/μm for detectors 1-2 and 1-3 respectively. When the measurement volume was located inside the region of the dense spray, data rates of 5 to 10 kHz were achieved, with a validation rate of approximately 60%. This relatively high data rate is a crucial factor for tracking the possible fluctuations that may appear in the characteristics of the spray during the forced flow experiments. However, even in the

characterization of the prefilmer under non-forced conditions, the high data rate enables faster data acquisition. The monitoring of the data acquisition via PDA, as well as the parameter control, was accomplished by using the corresponding commercial software [150]. The described setup is shown in Figure 3.34.
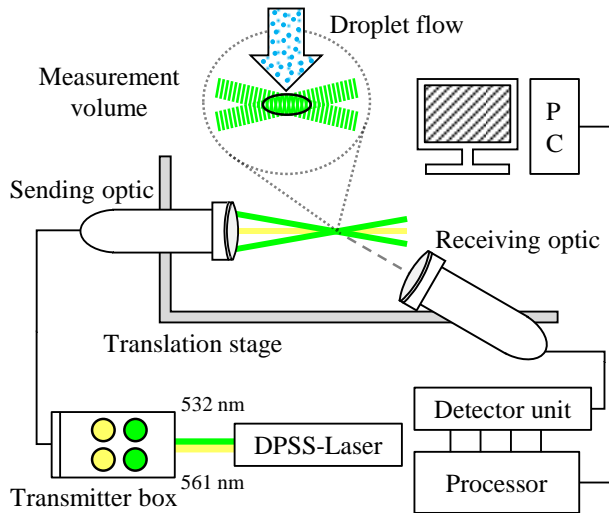
Figure 3.34: Schematic representation of the PDA setup.

3.3.3.2 Shadowgraphy

To characterize the spray in non-forced conditions, the technique of shadowgraphy was also employed on the setup. The shadowgraphy setup is schematically shown in Figure 3.35. The illumination system consists of a Litron Lasers double pulsed Nd: YAG laser and a high-efficiency diffuser, which diffuses the original laser beam of wavelength 532 nm to an incoherent

light sheet of wavelength in the range of 574 to 580 nm. The set of two pulses is emitted at a frequency of 15 Hz, for a duration of 4 ns per pulse and a time difference of approximately 10 to 15 µs between the two pulses. A Programmable Timing Unit (PTU) synchronizes the laser pulse with the acquisition system of the double frame sCMOS camera, which also collects images at a rate of 15 Hz. A long-distance microscope is coupled with the camera in order to enlarge the image.
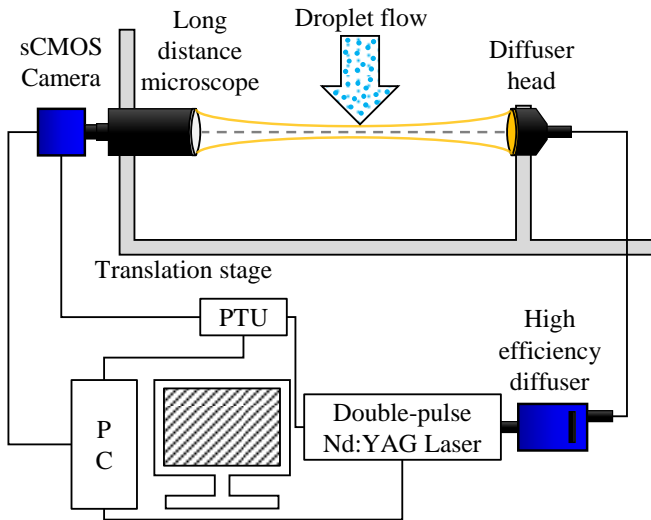
Figure 3.35: Schematic representation of the shadowgraphy setup.

In order to provide insight into the data acquired by the shadowgraphy technique, two exemplary images are shown in Figure 3.36: a photo of the primary breakup at the edge of the prefilmer and a photo of the spray of droplets downstream of the prefilmer. The photos shown in Figure 3.36(a) and (b) are taken in the planes illustrated in Figure 3.37(a) and (b) respectively.

Figure 3.37(a) highlights a 7 mm width and 6 mm height plane located at the lip of the nozzle, on Figure 3.37(b) 18 planes of the same size are shown for the spray characterization, both at Y = 0 mm.

(a)   (b)
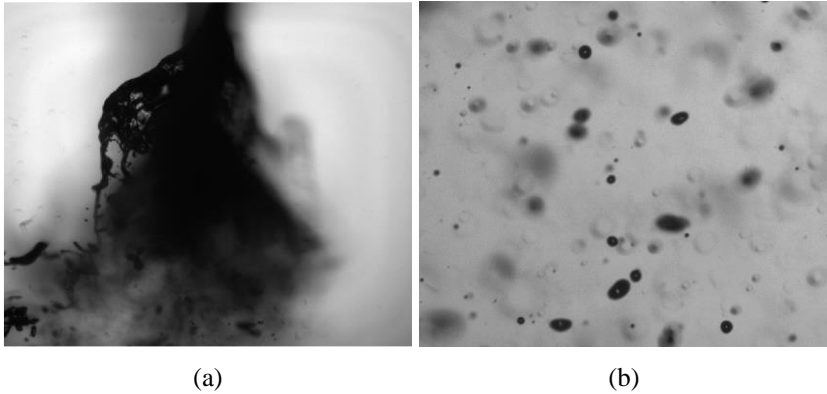
Figure 3.36: Shadowgraphy images: (a) film at the primary breakup region and (b) droplets at the spray region.

(a)   (b)
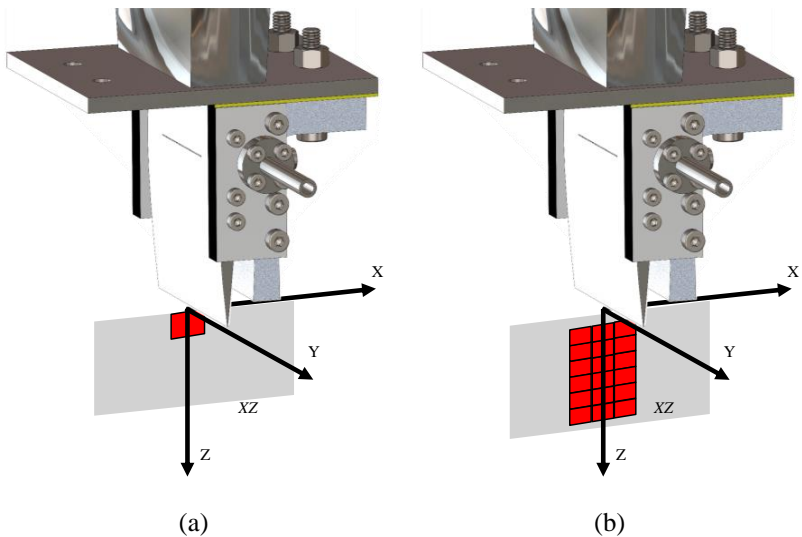
Figure 3.37: Shadowgraphy measurement positions: (a) for the primary breakup analysis and (b) for the spray characterization.

3.4   Phase Averaging of Periodic Signals

To properly analyse the data acquired from the experiments when the siren is operating and the oscillation is introduced in the flow, it is advantageous to present them in a way which reveals their periodic fluctuation. This method is called the time synchronous averaging or phase averaging of the signals [151]. Similar algorithms are used to determine the phase-locked characteristics of rotating equipment, or in applications where a fluid flow is naturally oscillating [152,153]. For this work, the phase averaging algorithm developed and applied depends on the type of the signal. As demonstrated in Figure 3.38, the signal types for this work are discretized not only based on the measurement technique itself but primarily on the nature of the sampling rate. To measure the air velocity with the hot-wire, the sampling rate is constant and strictly determined by the user. On the other hand, the droplet data acquired by PDA are unevenly sampled, because each sample is recorded whenever a droplet happens to cross the measurement volume and is properly identified by the software.
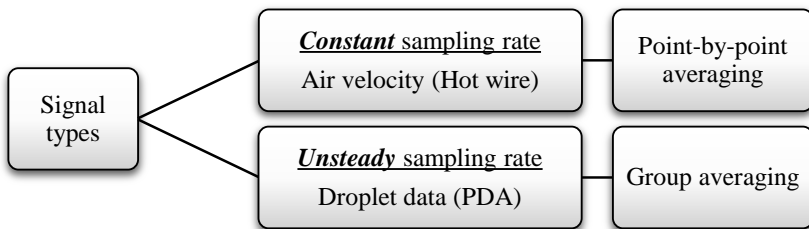
Figure 3.38: Determination of phase averaging algorithm of periodically oscillating signals depending on the measurement technique and its sampling rate type.

In the first case where the data rate is constant, the samples are evenly spaced in time. Assuming a periodic signal with random noise as shown in Figure 3.39(a), since all points are evenly distributed in time, each point in one period has its counterpart in the following periods. Therefore, a time-synchronous average algorithm can be applied, where the averaging is done point by point for each period of the signal. The outcome is displayed in Figure 3.39(b), where all repeating periods are shown in the background one on top of the other and the phase-averaged signal clearly emerges in front of them. The x-axis of the diagram in this case represents the phase angle from 0 to 360° instead of the time, implying an endless periodicity of that phase-averaged signal. This phase-averaged signal contains the same number of points with the points included in one period of the original signal. Assuming a phenomenon with a periodicity of 10 Hz and a sampling rate of 500 Hz, each period would contain 50 samples, therefore this would be the number of points on the resulting phase-averaged curve.

(a)   (b)
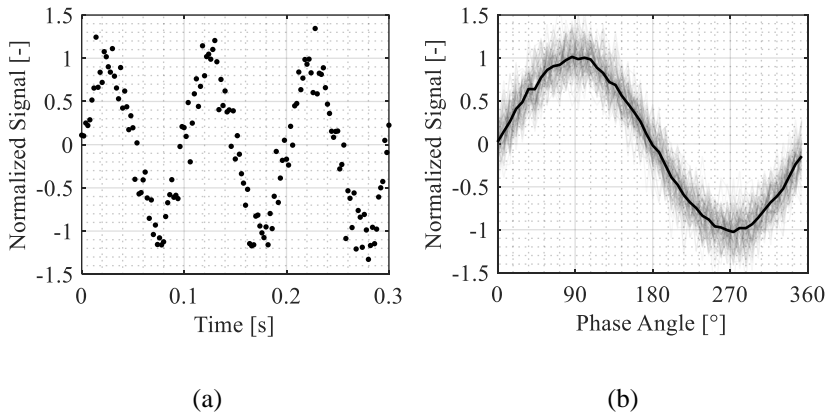
Figure 3.39: Phase averaging of signal with a constant sampling rate.

For the second case, the data are randomly sampled because of the nature of the PDA technique and the randomness of a spray. In such an occasion as shown in Figure 3.40(a), no point during each period has a corresponding point in the rest of the periods, since they are unevenly sampled. Therefore, every period in the measured signal is divided into a finite number of subsections. The data of each subsection of every period are grouped with the data of the corresponding subsection of every other period. This way, for every subsection an average value can be calculated as shown in Figure 3.40(b), or any other more complex calculation is possible (e.g. SMD or mass flux of the spray) since the data are grouped based on their phase angle. In Figure 3.40(b) the subsection boundaries are illustrated as vertical dotted lines and in-between the calculated average of each subsection as a black dot, forming this way the phase-averaged curve.

(a) (b)
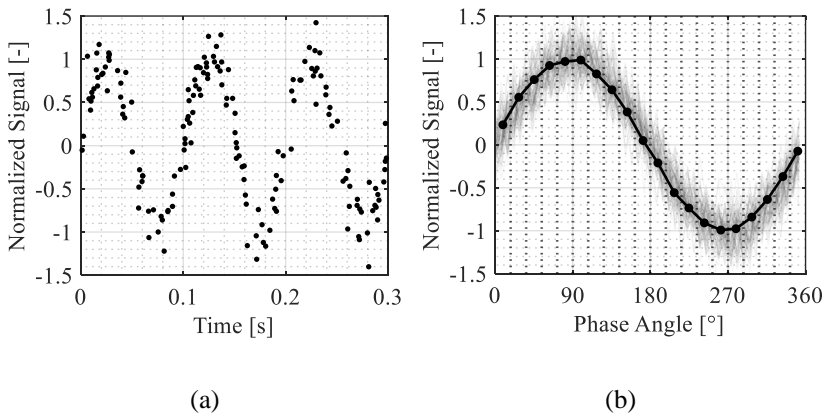
Figure 3.40: Phase averaging of signal with unevenly spaced data in time due to the random sampling rate.

4   Results and Discussion

4.1   Spray Characterization under non-Oscillating Flow Field

To characterize the model prefilmer that was designed and manufactured for these research activities, tests in the experimental setup were done without the operation of the pulsating device. Therefore, a steady airflow of determined conditions was applied to study the produced spray. The characterization of the prefilmer under steady conditions was accomplished using both measurement techniques described, i.e., shadowgraphy and PDA. The operating conditions for the spray characteristics results under a non-oscillating flow field presented in section 4.1 are summarized in Table 5.

Table 5: Summary of basic conditions for the non-oscillating flow field spray results.

X [mm]	Y [mm]	Z [mm]	$\overline{\Delta p / p}$ [%]	$\dot{V}/b$ [mm²/s]	$\overline{GALR}$ [-]
4.1.1 Sheet Breakup and Preliminary Spray Characterization					
Sheet Breakup					
				83.5	26
				62.6	35
-3.5:3.5	0	0:6	3	41.8	52
				20.9	104
Preliminary Spray Characterization					
-10:10	0	10:46	3	83.5	26
4.1.2 Model Prefilmer Characterization					
-10:0	0	40	3	83.5	26

4.1.1   Sheet Breakup and Preliminary Spray Characterization

4.1.1.1   Primary Breakup

To analyse the primary breakup procedure and quantify the average breakup length, the shadowgraphy imaging technique was utilized. Figure 4.1 shows the general processing procedure for estimating the breakup length under the various conditions presented in Table 5. For each of the four operating conditions, a set of four hundred images was acquired. Each image is essentially a matrix of values for the intensity of light reaching the camera lens on each pixel, where a zero value (black) represents the shadow of the liquid and the maximum value of 255 (white) represents the background light. Averaging the images as an arithmetic mean of the intensity for each pixel results in a new image representing the average behaviour of the ligaments' structure for the given operating conditions.
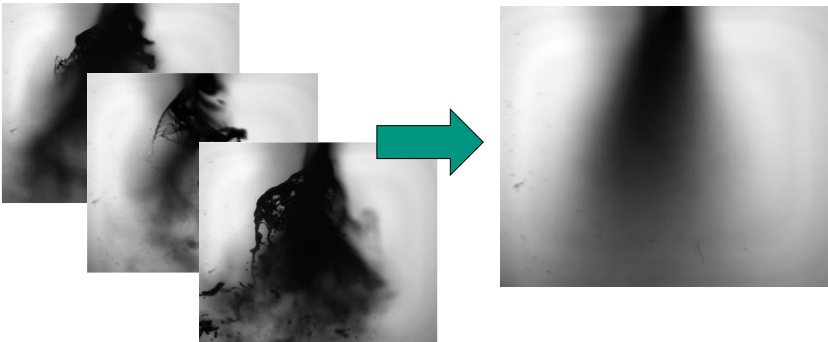
Figure 4.1: Averaging of recorded images at the edge of the prefilmer showing the primary breakup of the film.
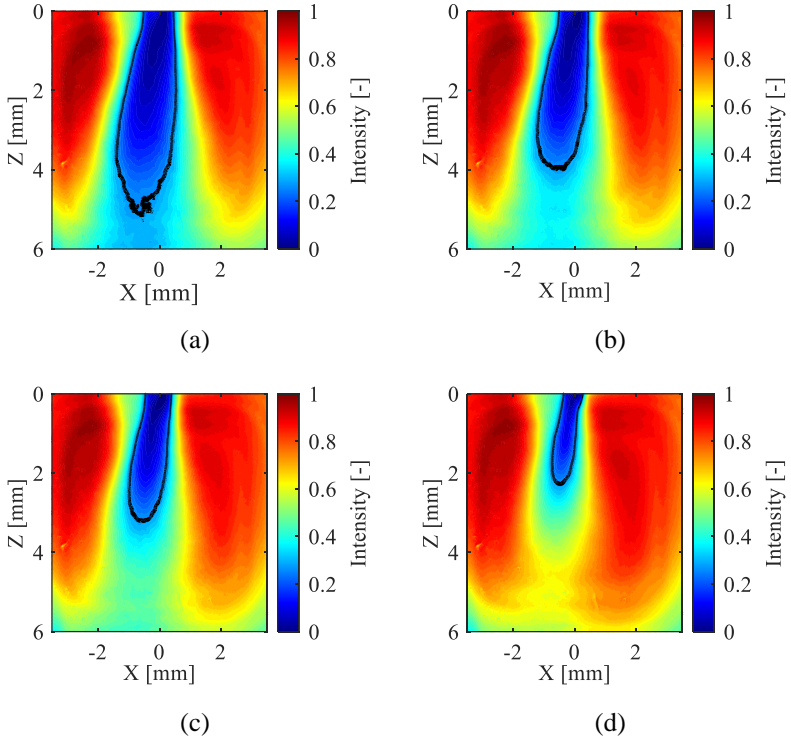
Figure 4.2: Probability-based breakup length for a variety of air-to-liquid ratios: (a) ALR = 26, (b) ALR = 35, (c) ALR = 52, and (d) ALR = 104.

Applying this procedure for a variation of operating conditions by changing the air-to-liquid ratio while keeping the pressure drop across the nozzle at 3%, the average image for each set of conditions was obtained. In Figure 4.2 the average image intensity is illustrated in the four air-to-liquid ratios investigated. Low intensity values denote locations containing mostly liquid while high values indicate the background illumination. By setting a threshold on the intensity to indicate the boundaries of the average liquid sheet, illustrated as a black line in Figure 4.2, the maximum distance of it in the Z axis

can be distinguished. With increasing air-to-liquid ratio, the primary breakup length becomes shorter. This outcome is reasonable since higher ALR values have a positive impact on the airblast atomization process, leading to shorter atomization timescales. Similar techniques for breakup length characterization have been reported in the literature for various applications [154–156].

The selection of such a threshold naturally affects the absolute value of the length. However, as shown in Figure 4.3 for a variety of thresholds p, the trend remains the same. For an increasing global ALR inside the range of values examined, the breakup length decreases with a power correlation and an exponent of approximately -0.75.

$$L = A + B \cdot ALR^{-0.75} \tag{4.1}$$

This decrease in the breakup length with the air-to-liquid ratio had already been documented in the literature in the previous decades [157] as well as in more recent investigations showing analogous power correlation trends [158,159].
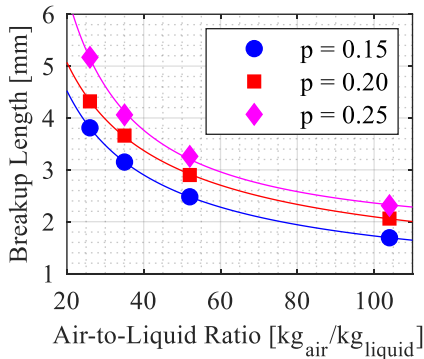
Figure 4.3: Breakup length correlation to the ALR.

4.1.1.2 Spray Characteristics

Figure 3.37(b) shows the 18 planes on which the spray characterization was carried out using the shadowgraphy imaging technique. The developed strategy was comparable to the Eulerian-Eulerian technique for the simulation of multi-phase flows in order to obtain a general picture of the distribution of spray properties [160–162]. The regions of the measurement area were discretized into a finite number of control areas, and the properties of all the particles inside the control area were averaged using this method. The observed results provide insight into the spray's average behaviour. However, because the amount of particles inside the control area directly influences the value being averaged, this average is highly dependent on the number of control areas. Therefore, an optimization on this number was applied in order to accurately represent the acquired data. Nevertheless, the qualitative trend of the data was independent of the discretization in control areas.

In Figure 4.4 the droplet velocity is illustrated in the measurement region defined in Figure 3.37(b). As explained in the aforementioned description, the measurement area was discretized into a finite number of control areas. In each of those discrete areas, all droplets were identified and their velocity was determined. Considering the statistical weight of each droplet as explained in subsection 3.3.2.4, the average velocity for the whole discrete control area was calculated.

$$u = \frac{\sum_{i=1}^{N}\left(u_{d,i} \cdot sw_i\right)}{\sum_{i=1}^{N} sw_i} \qquad (4.2)$$

The spray shows a symmetry around the centreline in the radial direction (X-axis); a local minimum in the velocity is observed around X = 0 mm and local

maxima approximately 5 mm radially from the centreline. The droplet velocity rises with increasing distance downstream of the nozzle (Z-axis), from approximately 25 m/s to 45 m/s. This is explained due to the acceleration of the droplets as they move along the Z-axis. The non-coloured regions denote areas in space where no droplets were identified by the software processing the recorded images.
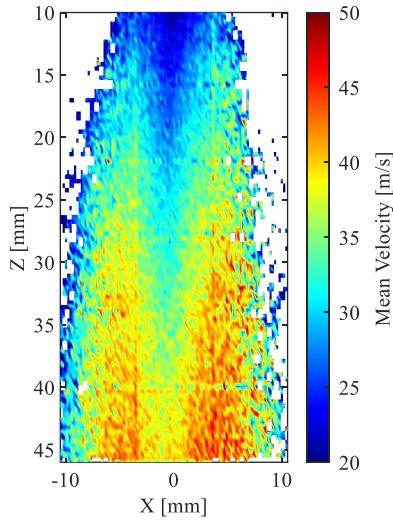
Figure 4.4: Droplet velocity distribution in the spray.

Having established the droplet velocity distribution in the spray region, the SMD is then demonstrated in Figure 4.5 in two ways. Figure 4.5(a) shows the typical SMD as calculated by the software taking into account the statistical weight of each droplet as explained in subsection 3.3.2.4. This parameter compensates for the size bias in the detection of droplets.

$$D_{32} = \frac{\sum_{i=1}^{N}(D_i^3 \cdot sw_i)}{\sum_{i=1}^{N}(D_i^2 \cdot sw_i)} \tag{4.3}$$

However, a second correction was also applied which depends also on the velocity of each accounted droplet. This is necessary because the number of particles inside the detection region in a determined time period is directly related to the frequency with which the particles are injected, which is inversely proportional to their velocity. Because of their fast movement and the greater distance between them, particles with a high velocity are underestimated if a velocity compensation is not applied to the SMD calculation [163].

$$D_{32} = \frac{\sum_{i=1}^{N}\left(D_i^3 \cdot sw_i \cdot u_{d,i}\right)}{\sum_{i=1}^{N}\left(D_i^2 \cdot sw_i \cdot u_{d,i}\right)} \qquad (4.4)$$
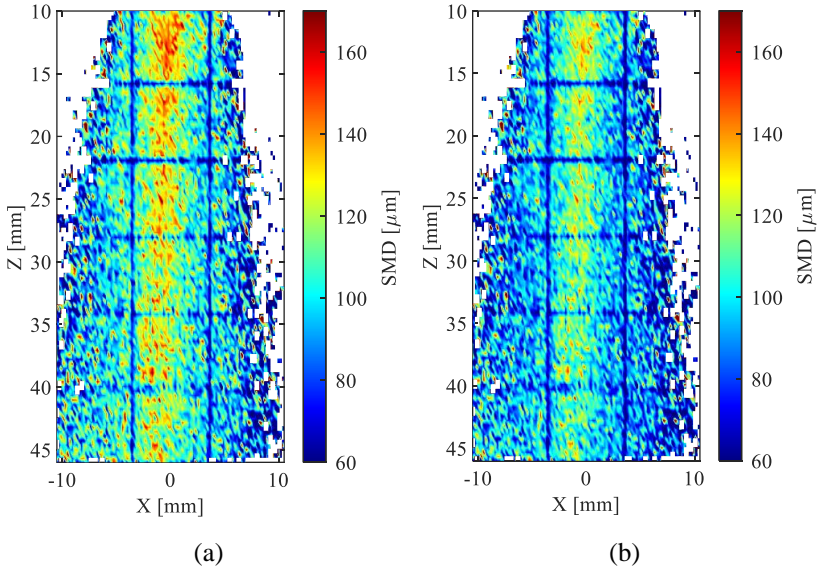
Figure 4.5: SMD distribution in the spray: (a) classic calculation and (b) velocity corrected calculation.

The SMD shows a local maximum at the centreline near $X = 0$ mm in contrast to the velocity at this spray region. Moving radially, along the X axis, the SMD

drops. The boundaries of each subsection of the spray region as shown in Figure 3.37(b) are visible in Figure 4.5. Since these are the boundaries of each individual measurement region, fewer droplets were identified there. Large droplets are more difficult to identify near the borders of each image compared to smaller ones, and therefore the SMD which is heavily weighted on larger diameters shows lower values in these borders.

Finally, the spray structure is depicted in Figure 4.6 as a number density, i.e. the droplet number of each discrete control area per mm² of that control area. Most of the droplets are concentrated along the centreline, while the spray spreads out as it moves downstream the prefilmer edge. An analogous structure was observed in the experimental work of Gepperth [164,165] and the simulations of Chaussonnet [166] where a similar geometry two-dimensional model prefilmer was investigated.
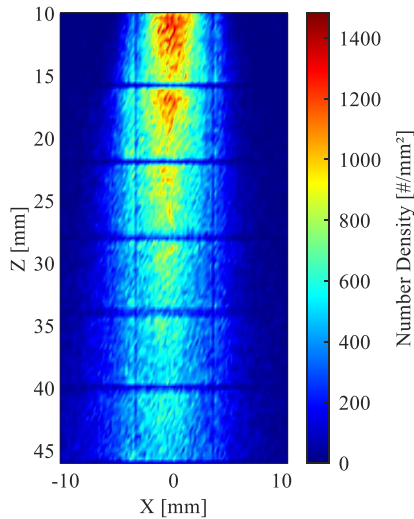
Figure 4.6: Spray structure illustrated as droplet number density.

4.1.2   Model Prefilmer Characterization

The model prefilmer was further characterized by means of PDA for a more detailed analysis of the spray structure. As shown in Table 5, the spray was analyzed in this subsection along the radial X-direction, at $Z = 40$ mm and $Y = 0$ mm. The reference conditions were maintained: a pressure drop across the nozzle of 3%, an air-to-liquid mass flow ratio of 26, and a liquid mass flow rate of 12 kg/h corresponding to a film load of 83.5 mm²/s.

To provide statistical relevance to the results presented, a confidence interval was implemented as well, with a confidence level of 95% for all cases. The method of the Student's t-test was applied for the spray characteristics that represent a simple arithmetic average [167], while the bootstrap resampling method was applied for the spray characteristics calculated in ways more complicated than a simple arithmetic average (e.g. SMD, mass flux) [168]. For the bootstrap method, 10,000 bootstrap samples were used for the error determination. In some cases such as the mean droplet velocity, the error of the investigated variable is negligible, leading to almost non-visible error bars on the diagram. For the X-coordinate a systematic error of ±0.5 mm was added to represent the uncertainty included in the movement of the translation stage and the human factor accuracy.

One of the most relevant measures of the spray measured with the PDA technique is the mean droplet velocity, which is analyzed in two components, the axial and the radial velocity, in the direction of the Z and the X-axis respectively. Figure 4.7 shows the two velocity components along the X-axis. The axial velocity, mirroring the behaviour observed by the shadowgraphy imaging technique illustrated in Figure 4.4, shows a local minimum at

X = 0 mm and a local maximum approximately 5 mm from the centreline. Comparable behaviour was observed in the literature for experiments or simulations on two-dimensional prefilming atomizers similar to the one of the present study [165,169]. The local minimum at X = 0 mm in the axial velocity in Figure 4.7 or Figure 4.4 is explained due to the wake downstream of the prefilmer. On the other hand, the radial velocity in Figure 4.7(b) shows near zero values at X = 0 mm where the spray is moving in the direction of the Z-axis and increases in absolute value in the radial direction. The velocity uncertainty is so small compared to the velocity values at the plotted points, that the error bars are not clearly visible. This shows that the average velocity calculated from the data is indeed a reliable outcome.

(a)

(b)
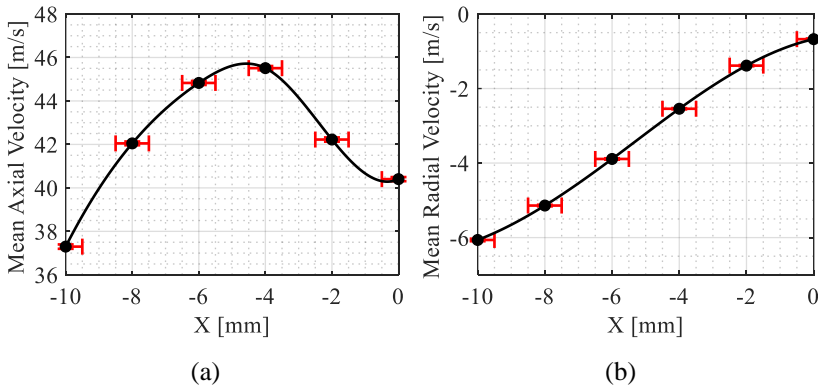
Figure 4.7: Mean spray velocity components along the X-direction at Z = 40 mm.

The most representative measure of a spray, especially in gas turbine combustor applications, is certainly the SMD. The measured SMD of the spray is shown in Figure 4.8. The values, as well as the trend along the radial direction, are in correspondence to the corrected SMD using the shadowgraphy

technique in Figure 4.5(b). The SMD is smaller when the average velocity of the spray is higher, which is expected since on average the smaller droplets move faster [170,171].
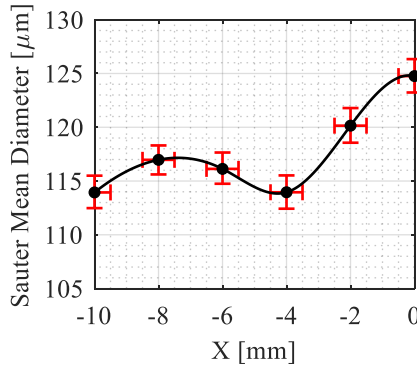
Figure 4.8: SMD of spray along the X-direction at Z = 40 mm.

This is also apparent in the size-velocity correlation of the spray. Figure 4.9 shows this correlation for the position at X = 0 mm, where the inverse proportionality of the velocity to the diameter is evident. Every dot on the diagram corresponds to the diameter and the velocity of a single droplet. Because in some regions of the diagram, the concentration of dots is higher than in other regions, meaning a higher number of droplets sharing a common velocity and diameter, a colour scale was applied to visualize this concentration difference. The colour scale implies the droplet number density, i.e. the number of droplets inside every grid cell of the graph. Naturally, the absolute number of droplets inside each cell directly depends on the number of cells in such a grid; the trend, however, is constant, and the number of cells in the grid is of trivial importance since clearer visualization is achieved. Similar

spray behaviours regarding the size-velocity correlation have been reported in various investigations in the literature [165,172].
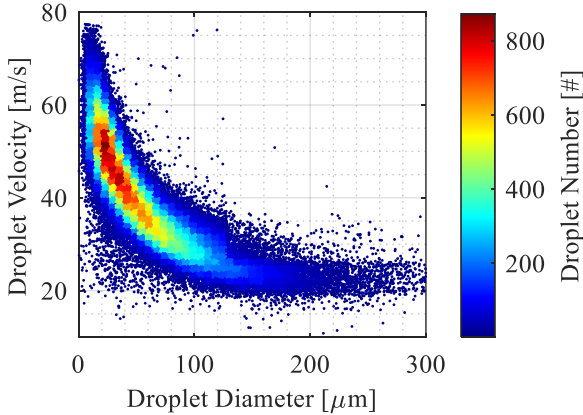
Figure 4.9: Size-velocity correlation of the spray at X = 0 mm and Z = 40 mm.

The advantage of the PDA system is that by utilizing the velocity and diameter measurement, the mass flux of the spray can be derived. This is possible by also taking advantage of the information about the arrival time of each droplet on the PDA measurement volume and the corresponding transit time (the time a droplet needs to cross the volume, in the scale of a few μs). The algorithm proposed by Saffman [143,173], discussed in 3.3.1.4, takes into account the mentioned time stamps for each droplet as well as the geometry of the PDA setup in order to estimate the effective area for the mass flux calculation. The resulting mass flux is calculated using Eq.(3.36)-(3.37) for the two mass flux components [174].

At a downstream distance of Z = 40 mm, a spectrum of locations on the X-Y plane was chosen to cover the whole spray cross-sectional area. The result is

shown in Figure 4.10, where the resulting total mass flux on the measured places is represented by black dots, while the data are fitted by a fifth-order polynomial surface. The spray mass flux peaks at $X = 0$ mm, showing that the spray is denser towards the centreline and sparse in the radial direction. The mass flux nears zero values at the borders of the interval on the X-axis, indicating that the spray region was virtually entirely covered. Calculating the volume beneath the surface fit with a surface integral of the mass flux data, the mass flow rate can be estimated. The resulting mass flow rate from the integration of the data was approximately 11 kg/h, close to the actual mass flow provided by the flow meter, with a deviation of less than 9%. This outcome validates the experimental data acquired.
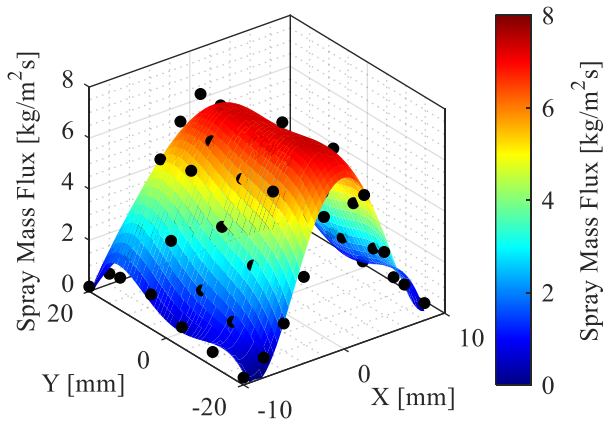
Figure 4.10: Spray mass flux at the $Z = 40$ mm plane.

4.2   Oscillating Flow Field

In order to characterize the operation of the siren in terms of amplitude and frequency, CTA hot-wire measurements were carried out. After calibrating the

probe for the expected velocity range as shown in 3.2.2, the air velocity at the nozzle could be measured while the siren is operating at various rotational speeds. Maintaining the same mass flow rate through the siren and split ratio between the siren and the plenum, the airflow velocity and its fluctuations were measured with the hot-wire. To separate turbulence effects from the influence of the excitation forced on the airflow, a low-pass filter at 2,000 Hz was applied during the data acquisition. This way, the high-frequency turbulence was eliminated and simultaneously all possibly occurring undesired harmonics of the forced excitation would remain in the signal.

4.2.1   Maximum Amplitude Oscillation

To begin with investigating the flow oscillations, the target was set in the low-frequency range of 90 to 150 Hz, since this is one of the ranges of interest for the instabilities usually occurring in jet engines referred to as engine rumble [14,175].
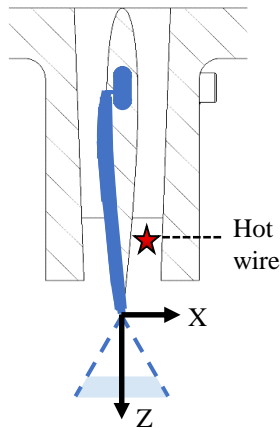
Figure 4.11: Hot-wire placement for the determination of excitation frequency.

To determine the excitation frequency to be used for spray measurements under low frequency forcing of maximum amplitude, the hot-wire probe was placed at Y = 0 mm, inside the air duct of the nozzle as illustrated in the cross-section of Figure 4.11. The measurements were carried out for 11 different rotational speeds, starting from 700 RPM to 1,100 RPM to match the aforementioned target range according to Eq.(3.1), with an increment of 40 RPM, or correspondingly 5.3 Hz. Once the velocity measurements have been accomplished, it was essential to analyse the results in the frequency domain, via a Fast Fourier Transform.

Figure 4.12 shows the FFT of the 11 velocity signals measured, depending on excitation frequency (each different colour representing a measurement with one corresponding rotational speed). Identifying the measured excitation frequencies from the FFT of Figure 4.12 and comparing them to the corresponding theoretical frequencies that should occur as a function of the forced rotational speed according to Eq.(3.1) that are shown in vertical dashed lines on the same diagram, a maximum deviation of less than 0.2% was observed in all cases.

Another critical variable to be taken into consideration is the presence of harmonics on the measured signals and their influence. As observed from the processing of the measured signals, the harmonics in most of the investigated cases are at least one order of magnitude lower than the main excitation frequency. This was taken into consideration when selecting the operating conditions for the spray characterization measurements since the ideal scenario would be to excite the airflow with a single frequency without any influence of harmonics on that signal.
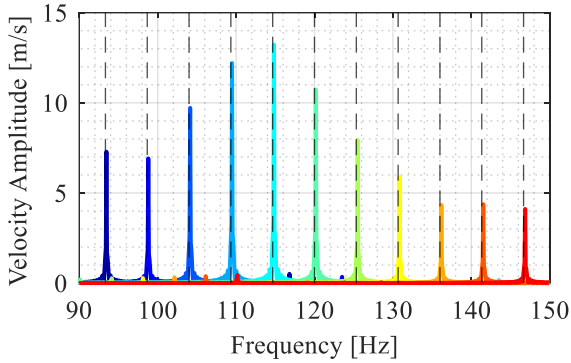
Figure 4.12: Fast Fourier Transform of the air velocity signal for low frequencies at the maximum possible amplitude, measured inside the air duct.

For the present work, the rotational speed of 900 RPM was chosen for the operation of the siren in order to investigate the atomization process, which corresponds to $f = 120$ Hz as calculated from Eq.(3.1), or 120.16 Hz as measured with the hot-wire anemometry and calculated through the FFT. For the sake of simplicity, this will be referred to as the case with a frequency of 120 Hz. The objectives were the maximum possible amplitude and the lowest possible influence of harmonics. The case of 120 Hz was therefore the choice that optimizes the objective criterion. Nevertheless, at all the rotation speeds tested, the higher harmonics had a non-zero but negligible amplitude.

Since the frequency appearing on the signal is determined by FFT, it is possible to calculate a phase-averaged velocity signal from all the separate periods included in it as explained in section 3.4. Each point can be averaged with its counterpart in all the other periods, with a time step of exactly $T = 1/f = 8.3$ ms (i.e. a time step equal to the period of the determined excitation frequency). Figure 4.13 shows the outcome of this method; the solid line is the resulting

phase averaged velocity for one period (corresponding to one-eighth of the rotation of the siren rotor), while the mist of lines on the background represents all the separate one-period signals superimposed. To isolate the modulation of the airflow velocity from the turbulence, a low-pass filter at 2,000 Hz was applied to the raw signal. The resulting curve after the phase averaging shows a negligible deviation from all the separate periods contained in the signal, indicating how accurately the siren produces the oscillation in the flow without interference in the signal. In fact, the maximum deviation of the original signal from the phase-averaged result is less than 3% at the extremes of the oscillation.
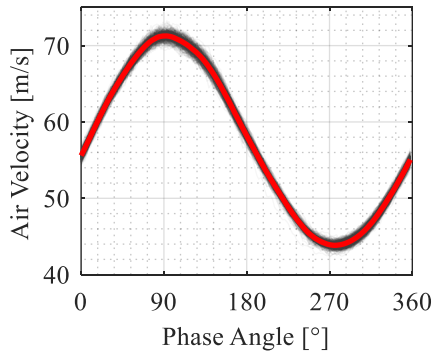
Figure 4.13: Phase-averaging of the air velocity at an excitation frequency of 120 Hz.

By considering the phase-averaged signal continuously in time, it can be directly superimposed with the original signal. This is illustrated in Figure 4.14 where the phase-averaged air velocity demonstrates a proper fit to the original signal. Since the frequency of 120 Hz was selected for carrying out the spray measurements, it was useful to obtain the phase-averaged air velocity for the same positions where the spray was measured. Therefore, Figure 4.15 shows

the phase-averaged air velocity along the radial direction at a downstream distance of $Z = 40$ mm, from the centreline $X = 0$ mm until $X = -10$ mm, always at $Y = 0$ mm. As observed, the air velocity does not substantially change in this radial distance.
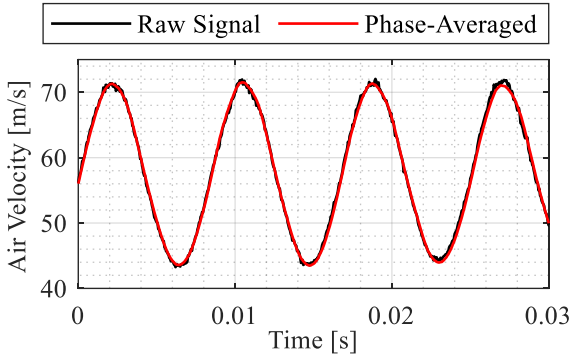
Figure 4.14: Raw signal of measured air velocity compared to the calculated phase-averaged velocity.
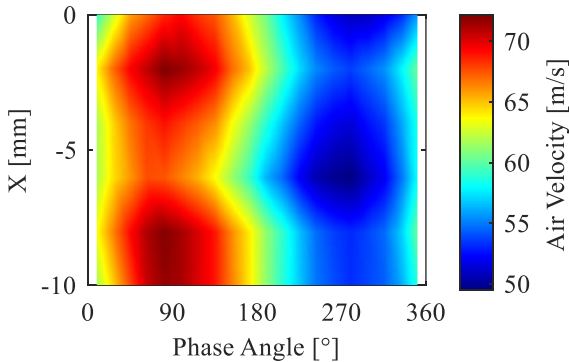
Figure 4.15: Phase-averaged air velocity along the radial direction at an excitation frequency of 120 Hz at $Z = 40$ mm.

4.2.2 Similar Amplitude Oscillations

Apart from thoroughly analyzing the spray in a low-frequency excitation, this work examines the influence of the excitation frequency as well. Therefore, a wide range of excitation frequencies was investigated in order to determine the appropriate conditions for spray measurements. However, since the target of this second part was not to investigate the spray characteristics at the maximum possible amplitude, but rather to study the influence on the spray at various frequencies, the airflow split was adjusted in order to obtain a lower oscillation amplitude compared to the first part. For these measurements, the hot-wire probe was placed once more inside the air duct as shown in Figure 4.11.

This time, the target was set in a broad range, from 50 to 500 Hz, since this is generally a large and interesting range for the thermoacoustic instabilities. Measurements for 46 different rotational speeds were carried out, from 375 RPM to 3,750 RPM, with an increment of 75 RPM, or correspondingly 10 Hz. The same procedure with post-processing of the acquired velocity signal was applied, by analysing the frequency domain with a FFT, as shown in Figure 4.16. As in Figure 4.12, each different colour represents the FFT curve of a measurement with a different corresponding rotational speed of the siren rotor, i.e. with a determined excitation frequency.

Even though the total air mass flow was constant during the 46 different cases, a resonance appears in the system when the excitation frequency reaches multiples of 100 Hz. This means that around these frequencies, the amplitude of the oscillation is greater than in the rest of the investigated cases, although the rest of the operating conditions are unchanged. The x-axis of the diagram in Figure 4.16 extends to 1,000 Hz, which is double the highest investigated

frequency of 500 Hz. This shows the harmonics of some of the signals, which in most cases are at least one order of magnitude lower than the main excitation frequency.
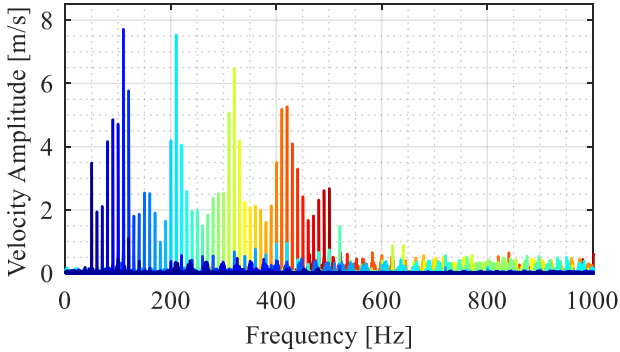
Figure 4.16: Fast Fourier Transform of the air velocity signal for a large variety of excitation frequencies from 50 to 500 Hz showing the resonance around multiples of 100 Hz, measured inside the air duct.

Since the highest amplitude appeared near the multiples of 100 Hz, a new measurement campaign was planned specifically around these resonance regions. These more targeted investigations consist of sets of 21 measurements with an increment of 15 RPM in the rotational speed of the motor, or 2 Hz according to Eq.(3.1). The regions investigated were four: 90 to 130 Hz, 190 to 230 Hz, 300 to 340 Hz, and 400 to 440 Hz. The FFT for each of these four measurement campaigns is presented in Figure 4.17.

As shown in Figure 4.17, the various excitation frequencies have different amplitudes. Since the target of this campaign was to investigate the spray response under multiple excitations of different frequencies, it made sense to select the cases where the amplitude is constant. In Table 6, a summary of the

investigated ranges and the selected frequencies for the spray measurements is presented. The cases of 102 Hz, 206 Hz, 320 Hz, and 416 Hz share an oscillation amplitude of approximately 6.5 m/s.
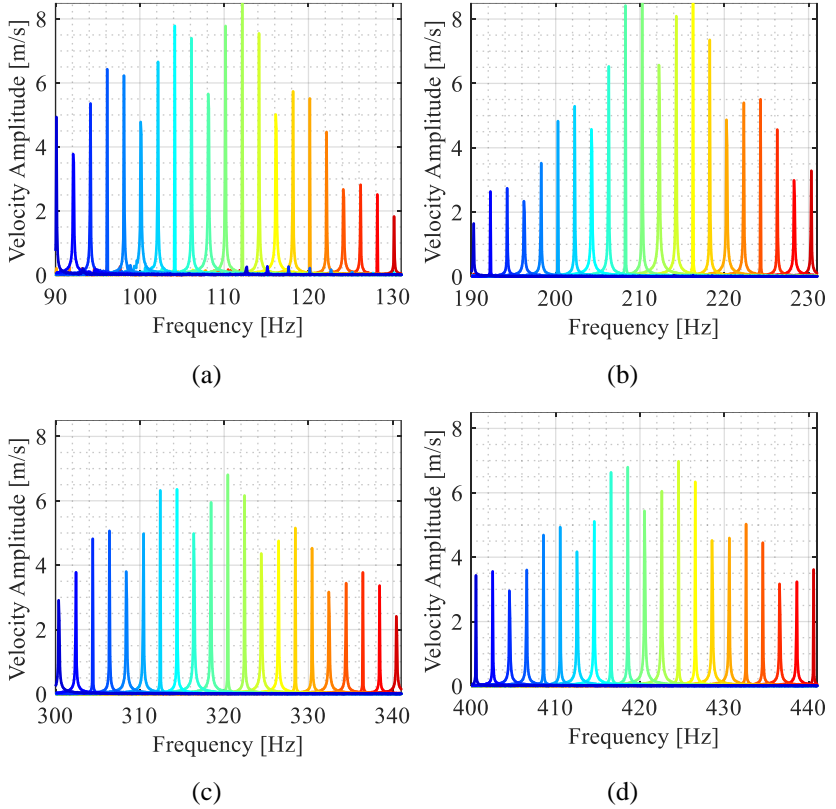
Figure 4.17: Fast Fourier Transform of the air velocity signal in the ranges: (a) 90 to 130 Hz, (b) 190 to 230 Hz, (c) 300 to 340 Hz, and (d) 400 to 440 Hz, measured inside the air duct.

Table 6: Selected frequencies as operating conditions for the spray measurements.

Case	Range	Selected Frequency	Amplitude
1	90-130 Hz	102 Hz	
2	190-230 Hz	206 Hz	
3	300-340 Hz	320 Hz	6.5 m/s
4	400-440 Hz	416 Hz	

4.2.3   Spray Measurement Plan

Having determined all the cases for both the low-frequency analysis as well as the frequency influence analysis, the basic operating conditions are summarized and presented in Table 7.

Table 7: Summary of basic conditions for the forced flow spray results.

f	Amplitude	X	Y	Z	$\overline{\Delta p/p}$	$\overline{\dot{V}/b}$	$\overline{GALR}$
[Hz]	[m/s]	[mm]	[mm]	[mm]	[%]	[mm²/s]	[-]
4.3.1 Spray Centre Analysis							
120	11	0	0	40	3	83.5	26
4.3.2 Radial Direction Analysis							
120	11	-10:0	0	40	3	83.5	26
4.4.1 Influence of Excitation Frequency on the Spray Characteristics							
102							
206	6.5	-10:0	0	40	3	83.5	26
320							
416							

All experiments were conducted at atmospheric conditions, with an average pressure drop across the nozzle of 3% and an average global air-to-liquid ratio of approximately 26. Since the uniformity of the spray along the Y-axis was confirmed in 4.1.2, the experiments were conducted at Y = 0 mm. Across the axial direction downstream of the nozzle, the distance of Z = 40 mm was selected. Based on the preliminary measurements presented in 4.1, at this downstream distance, the spray has completely formed and reaches a radial distance of 10 mm, which is enough to characterize the spray in a large enough distance, for a second direction as well.

4.3   Spray Characterization under Low-Frequency Forcing

In order to measure the spray characteristics with PDA, it is necessary to operate the siren at the rotational speed that was determined by the aforementioned analysis. The same airflow split and the same average total air mass flow were maintained. While the air was excited by the siren at the frequency of f = 120 Hz, the influence on the atomization process was recorded with PDA measurements. For each droplet passing through the measurement volume, its velocity as well as its diameter were measured with the corresponding time stamp. By post-processing the 100,000 droplet samples of data in a MATLAB code which was developed for this purpose, their periodic fluctuation could be derived as a function of the phase angle, similar to how the phase-averaged velocity of the air was calculated. The basic characteristics of the spray were averaged in twenty bins for a time period that corresponds to one period of the phenomenon. In this section, the analysis of the spray characteristics is split into two parts: the first part involves a thorough

analysis at the centre of the spray, while the second part includes the behaviour of the same characteristics along the radial direction.

4.3.1 Spray Centre Analysis

In this subsection, the spray is analyzed at the centreline, i.e. at X = 0 mm. In most of the following graphs explaining the behaviour of the spray, the y-axis represents a spray parameter and the x-axis the phase angle, showing the periodic oscillation of the respective spray parameter.

4.3.1.1 Basic Spray Characteristics

The most basic but rather relevant measure of the spray is the arithmetic mean diameter D_{10}, which provides preliminary information about the size distribution of the spray. Figure 4.18 shows the phase-averaged mean diameter of the spray, where a significant variation of approximately 10% of its average value is observed.
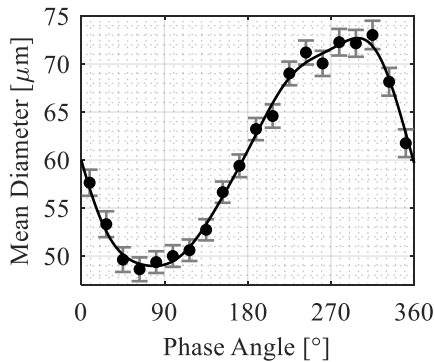
Figure 4.18: Phase-averaging of mean droplet diameter at X = 0 mm and Z = 40 mm.

The average from approximately 5,000 samples in each of the twenty subsections is reliable since the 95% confidence interval calculated with the Student's t-test is narrow.

A more detailed way to examine the behaviour of the droplet sizes is to observe the original diameter data of each individual droplet along one period of oscillation, as shown in Figure 4.19. The droplet number is illustrated along the period as the number density in a grid on top of the diameter data, in order to show which parts of the graph contain more droplets. It is evident that the sudden increase of droplet number before 90° mainly affects droplets with smaller diameters, therefore the mean droplet diameter decreases. Simultaneously, the oscillation of the SMD along the period is shown in Figure 4.19, which is in phase with the mean diameter. Apart from the diameter information, the velocity of each droplet was calculated through the PDA technique. Since the radial velocity at $X = 0$ mm is negligible (Figure 4.7(b)), only the axial component is considered in 4.3.1. In Figure 4.20, the velocities of all detected droplets are illustrated for one period of the fluctuation phenomenon, while the phase-averaged droplet velocity is shown as well in a black curve. The number density in the droplet velocity is also illustrated in Figure 4.20 during the period of oscillation, simultaneously with the independent velocity of each droplet. It is evident that during a certain time the period around 90°, an above-average number of droplets pass through the measurement volume, as it was already observed in Figure 4.19. However, Figure 4.20 shows that this burst of droplets around 90° is not related to a specific velocity class, but rather to all droplet velocities.
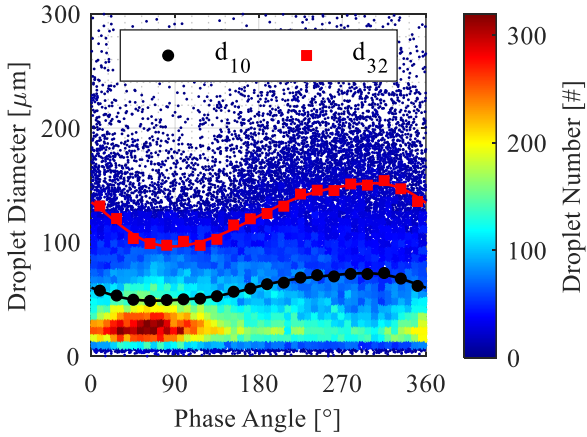
Figure 4.19: Droplet diameter - number density along one period of the oscillation at X = 0 mm and Z = 40 mm.
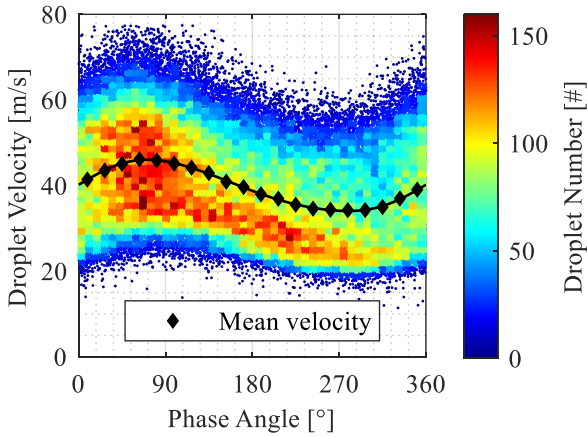
Figure 4.20: Droplet velocity - number density along one period of the oscillation at X = 0 mm and Z = 40 mm.

To get a better overview of the mean droplet velocity, the droplets were divided into size classes according to their diameter. In Figure 4.21, this size-class separation is shown for numerous diameter classes starting from 0 to 5 μm, with an increment of 5 μm from each class to the next. Each curve represents the phase-averaged mean droplet velocity in one period for the droplets belonging to the respective size class, along with the phase-averaged velocity of all the droplets denoted in the black curve. As expected, the small droplets have higher velocity due to their low inertia and a subordinate small Stokes number [170,171], which allows them to follow the trajectory of the airflow more easily. As the droplet diameter increases, the mean droplet velocity has a lower mean value and a lower oscillation amplitude. The velocities in the classes of the largest droplets appear to converge on each other, which is consistent with the minimum values of droplet velocities from Figure 4.20.
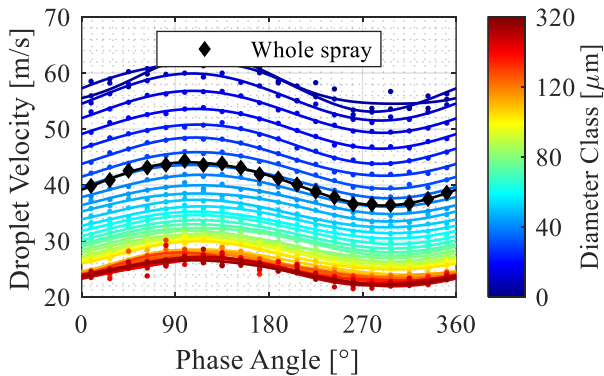
Figure 4.21: Size-class separation for the phase-averaged mean droplet velocity at X = 0 mm and Z = 40 mm.

One of the most important parameters necessary for the characterization of the spray is the SMD and its variation over time (Figure 4.22). Apart from the

already illustrated oscillating behaviour shown in Figure 4.19 alongside the mean diameter, two main outcomes are observed.
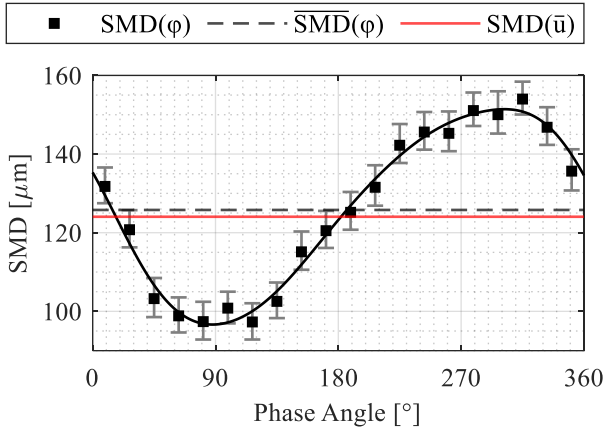
Figure 4.22: Phase averaging of SMD in comparison with unforced flow SMD at X = 0 mm and Z = 40 mm.

The first outcome is that there is a natural shift of approximately 180° between the droplet velocity (Figure 4.20) and the SMD (or the mean diameter from Figure 4.19), as shown by other similar investigations as well [176], because the smaller the droplets are, the lower their inertia and hence the faster they move.

The second outcome becomes clear when the SMD of a non-forced experiment at the average air velocity of Figure 4.13 is juxtaposed with the SMD of the forced flow case. The SMD of the mean air velocity is almost the same as the mean SMD of the forced case, namely slightly lower. This experimental observation could indicate that the spray in the two cases of a forced flow and

a stationary flow at the average forced air velocity is similar because of the breakup mechanism, but the droplets are subject to a temporal separation.

To further support the hypothesis of this separation of the droplets, similar behaviour with respect to the SMD can be noticed numerically by using the following model, which predicts the SMD of the spray generated by a similar two-dimensional airblast prefilmer [103]:

$$\frac{D_{32}}{\delta_{x,e}} = 4.96 \, \text{Re}_d^{-0.17} \, \text{We}_d^{-0.36} \left(\frac{\rho_l}{\rho_g}\right)^{-0.013} \left(\frac{h}{\delta_{x,e}}\right)^{0.46} \tag{4.5}$$

where D_{32} is the SMD of the spray $\delta_{x,e}$ is the boundary layer thickness at the atomizing edge, Re_d and We_d are the Reynolds and Weber numbers of the droplet spray respectively, ρ_l and ρ_g are the densities for the liquid and the gas respectively, and h is the atomizing edge thickness.

Further analyzing the model, since all non-constants of Eq.(4.5) are a function of the gas velocity, it is possible to directly correlate the SMD with the gas velocity as follows:

$$D_{32} = c \cdot u_g^{-0.892} \tag{4.6}$$

where c is a constant derived from all the constants and the gas and liquid properties of Eq.(4.5).

The SMD calculated from Eq.(4.6) fluctuates asymmetrically about its mean value when the oscillating air velocity of Figure 4.13 is used as an input for the gas velocity of Eq.(4.6). This is observed in Figure 4.23, which shows the derived SMD, the average SMD, and the SMD of the average air velocity. According to Eq.(4.6), the SMD of the average air velocity is 123.3 μm, while

the average SMD of the oscillating solution from Eq.(4.6) is slightly higher at 124.6 μm, reflecting the behaviour observed in the experimental results in Figure 4.22.
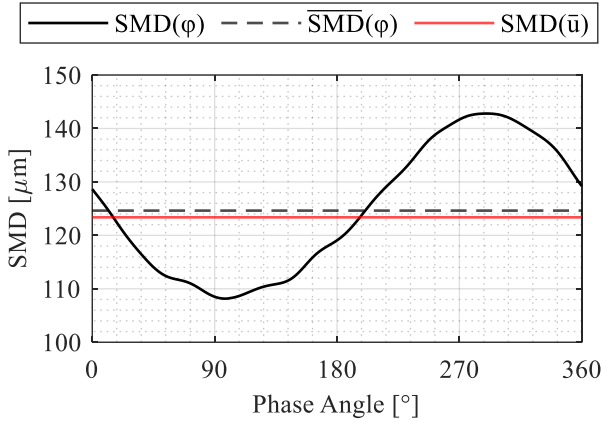
Figure 4.23: SMD calculation based on the measured phase-averaged air velocity at X = 0 mm and Z = 40 mm.

4.3.1.2 Derived Spray Characteristics

The large variation in the diameter of the spray over time can be explained by a change in the diameter distribution along the oscillation period. In Figure 4.24, the droplet diameter distribution is shown as a probability density function for two instances of the period, with a phase difference of 180°, near the minimum and maximum of the SMD fluctuation at the centreline (X = 0 mm). The difference in the shape of the distributions is clear; at 261°, the peak is less pronounced and there are more droplets with high diameters compared to the distribution at 81°, hence the higher SMD and mean diameter. As discussed in section 2.3.2, various models have been proposed to quantify

the particle size distribution. The most extensively used is the one developed by Rosin and Rammler [108]. Figure 4.25 is an example application of the Rosin-Rammler equation for one phase angle. The fit to the data is rather appropriate, either on the volume fraction or the cumulative volume fraction on the right axis.
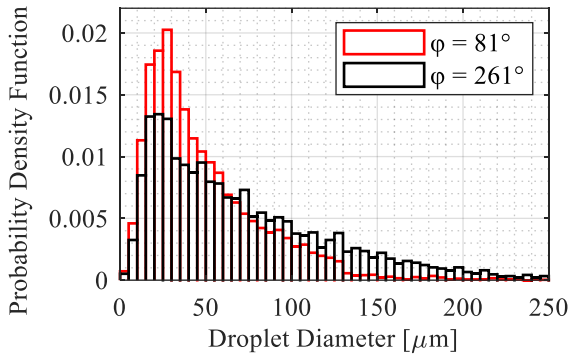
Figure 4.24: Probability Density function of the droplet diameter for two instances of the periodic oscillation at X = 0 mm and Z = 40 mm.
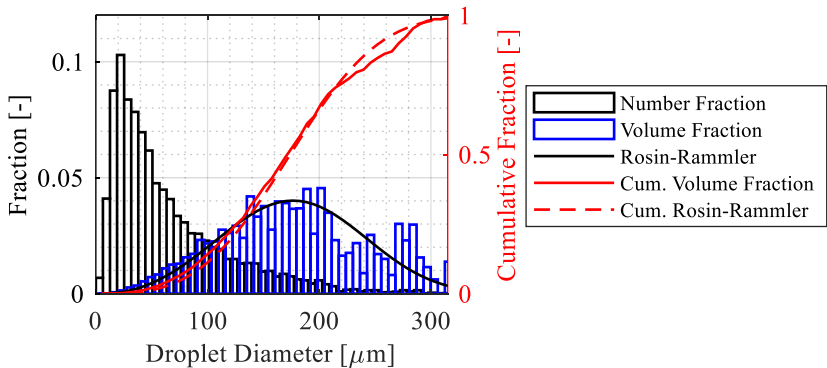
Figure 4.25: Rosin-Rammler fit on the volume fraction of the droplet size distribution in one instant of the period at X = 0 mm and Z = 40 mm.

125

By fitting the Rosin-Rammler equation to the diameter distribution data for each different time stamp during the period, the two model parameters were obtained. In Figure 4.26, the $D_{63.2\%}$ parameter is clearly oscillating in time, similar to the SMD of the spray, explaining how the droplet size distribution of Figure 4.24 fluctuates in time. The spread parameter q also shows a slight but rather insignificant oscillation, while it is mostly maintained in the range of 2 to 3.

The two vertical dashed lines indicate the time instances for which the two probability density functions were shown in Figure 4.24, 81° and 261°; both points are located near the maximum and minimum of the Rosin-Rammler distribution parameters. The smaller the q parameter, the wider the volume distribution is, while at infinite values the volume distribution collapses at a single diameter. On the other hand, for larger values of the $D_{63.2\%}$ parameter, the distribution shifts to higher diameters. The oscillation of the $D_{63.2\%}$ parameter is actually stronger, as expected by the distribution change during the period.
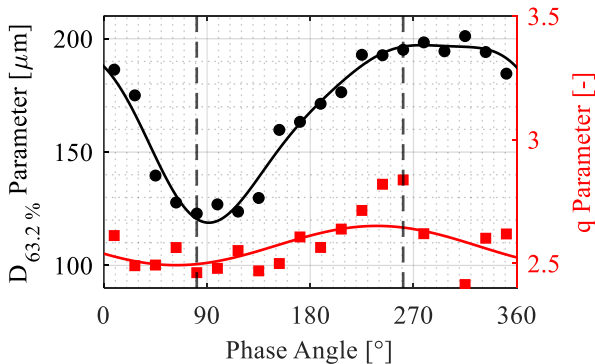
Figure 4.26: Parameters of the Rosin-Rammler droplet size distribution models at X = 0 mm and Z = 40 mm.

A further derived characteristic of the spray is the mass flow rate per unit area, i.e. the mass flux of the spray. By following the algorithm described in 3.3.1.4 which was applied in non-forced conditions in Figure 4.10, the mass flux can be calculated and its potential oscillation in the period can be observed.

For each measured position in the spray, a single value of the mass flux is usually calculated. Since in this section the data were phase-averaged into twenty bins, the mass flux is calculated separately for each bin on the $X = 0$ mm position. The result of the mass flux is presented in Figure 4.27, where a clear oscillation over time can be observed with an average of approximately 7.4 kg/m²s, matching the values observed at the centre of the spray in non-forced conditions shown in Figure 4.10. Even though the mass flux calculation is based on both the velocity and the diameter of the droplet, it is evident that higher values are observed when the SMD of the spray is larger (comparing Figure 4.27 with Figure 4.19 or Figure 4.20), showing that the size of the droplet is dominant over its velocity for the mass flux estimation.
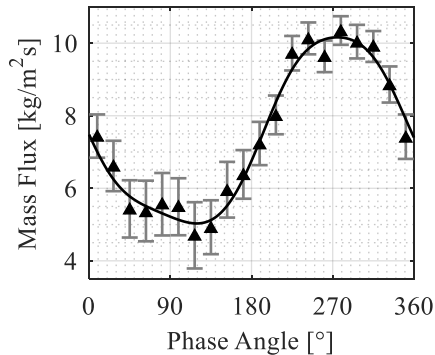
Figure 4.27: Phase averaging of the spray mass flux at $X = 0$ mm and $Z = 40$ mm.

Having established the fact that the spray mass flux oscillates in time due to the acoustic forcing imposed in the airflow, even though the water was supplied in the system at a constant rate, the question of the behaviour of the air-to-liquid ratio arises. The ALR is expressed as the mass flow rate of the air over the mass flow rate of the liquid:

$$\text{ALR} = \frac{\dot{m}_A}{\dot{m}_L} = \frac{\rho_A u_A}{\dot{m}_L''} \tag{4.7}$$

In this case, where the mass flux of the liquid is calculated based on the algorithm developed by Saffman, the second expression of Eq.(4.7) can be used. For the air mass flow rate, the phase-averaged air velocity shown in Figure 4.13 was utilized. Since both the velocity on the numerator and the mass flux on the denominator are phase-averaged in one period, this also applies to the resulting ALR.
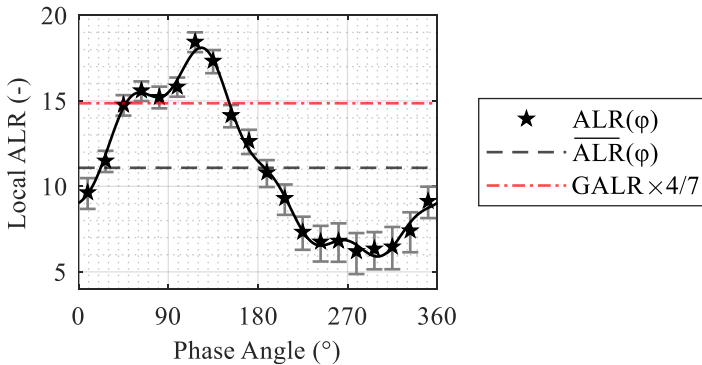
Figure 4.28: Phase averaging of local Air-to-Liquid Ratio at $X = 0$ mm and $Z = 40$ mm.

The local ALR calculated at $X = 0$ mm is shown in Figure 4.28 where a strong periodic oscillation can be observed. In the same graph, two horizontal lines

have also been highlighted. The black one refers to the average of the oscillating local ALR. The red line is a specific fraction of the average global ALR (GALR), i.e. the total average mass flow rate of the air supplied in the system over the total water mass flow rate, which was approximately 26 as mentioned in Table 7. On the model prefilmer, as shown in Figure 3.5, the air obviously flows over the entire duct with a width of 70 mm, while the water film covers a width of only 40 mm, due to the positioning of the drilled holes. Therefore, a 4/7 fraction of the GALR is relevant in this context of comparing with the calculated local ALR. This fraction of the GALR is higher than the average of the oscillating local ALR. This is normal since the majority of the droplets fall in the region under the prefilmer (at $X = 0$ m), as shown by preliminary measurements under non-forced conditions. Therefore, the local ALR in this position is expected to be lower than the GALR. This implies that at a specific radial distance, the local ALR should be equal to that fraction of the GALR

4.3.2   Radial Direction Analysis

Having established and discussed the spray characteristics in detail for one location in the spray, namely the spray centre for a determined downstream distance, a reasonable next step was to study how the same characteristics behave in the radial direction. Therefore, in this subsection, the spray is analyzed along the radial direction of the X-axis for a distance of 10 mm, as shown in Table 7. In most of the following graphs explaining the behaviour of the spray, the y-axis represents the radial direction X and the x-axis the phase angle. The respective spray parameter is illustrated as a coloured contour,

showing the periodic oscillation of the respective spray parameter in time for multiple radial locations.

Figure 4.29 depicts the mean vertical droplet velocity measured utilizing the PDA system's green line (532 nm wavelength), which shows a noticeable periodic oscillation over time for all various measured positions. A local maximum in the mean axial droplet velocity develops in the spray along the X-axis, approximately 4 to 6 mm away from the centreline, while the airflow velocity was relatively constant as observed in Figure 4.15. However, this local maximum of the mean droplet velocity was also noticed in the spray during the investigations under non-forced conditions of section 4.1, in Figure 4.4 and Figure 4.7(a). This is another indication that the spray structure is similar to the non-forced case, although the droplets undergo a fluctuating movement. Figure 4.29 also depicts a number of black dots that qualitatively indicate the SMD for each measured place depending on the phase angle. The SMD is smaller when the velocity is higher, which is expected since small droplets tend to accelerate and move faster [170,171]. Because the measurement technique used for this investigation involved a 2D PDA system as described in section 3.3.1, the radial velocity component, parallel to the X-axis, was also determined utilizing the PDA system's yellow line (561 nm wavelength). This radial velocity component shown in Figure 4.30, as expected in accordance with the non-forced case of Figure 4.7(b), increases in absolute value with an increasing radial distance from the centreline. The temporal oscillation is also visible, with a phase matching to the axial velocity component. The absolute amplitude of the oscillation in radial velocity increases as the absolute mean value increases from X = 0 mm to X = -10 mm.
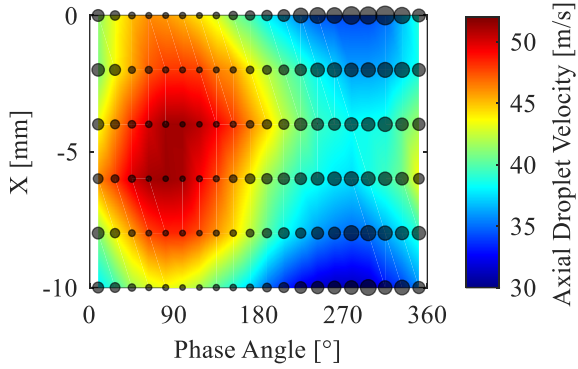
Figure 4.29: Periodic oscillation of mean axial droplet velocity along the radial direction (qualitative SMD trend on black dots) at Z = 40 mm.
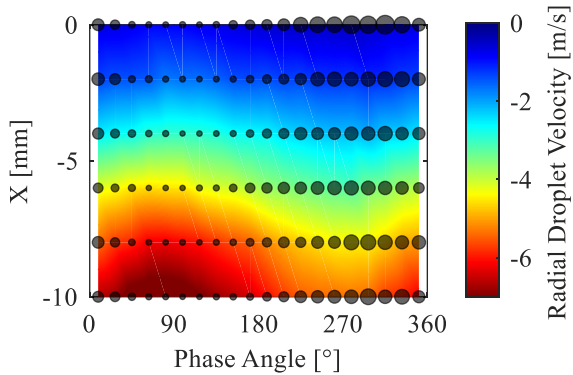
Figure 4.30: Periodic oscillation of mean radial droplet velocity along the radial direction (qualitative SMD trend on black dots) at Z = 40 mm.

This results in a variation in the mean velocity angle (i.e. spray half-angle) in space along the radial direction, but apparently not in time, as shown in Figure 4.31. At the limits of the measured interval, this angle (relative to the Z-axis on the X-Z plane) increases in absolute value, reaching values of up to 10°.
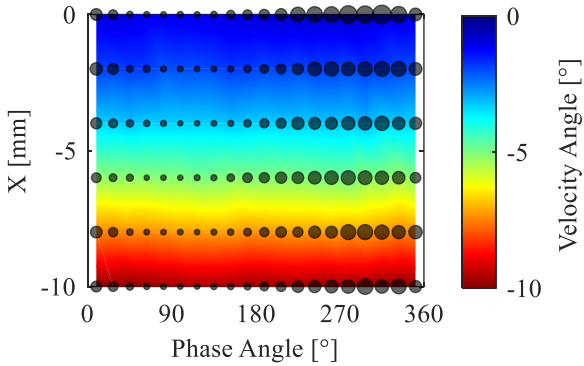
Figure 4.31: Mean velocity angle along the radial direction (qualitative SMD trend on black dots) at Z = 40 mm.

This indicates a spray angle of approximately 20° at a radial distance of ±10 mm on the X-axis. However, no substantial variation is observed throughout the oscillation period because the fluctuations of the two velocity components compensate each other. This means that an external observer with a fixed point of view at one position of the spray as an Eulerian approach, would observe the droplets continuously arriving at the same angle, although their absolute velocity oscillates in time due to the excitation imposed in the system.

Utilizing the measured droplet diameters from the PDA technique, the SMD of the spray was calculated. For all 6 measurement positions along the radial direction, the SMD is displayed in Figure 4.32. As already seen in Figure 4.22, the SMD undergoes a clear periodic fluctuation at the centre of the spray, which seems to be maintained along the radial direction. The black dots on this graph represent the average absolute velocity (total velocity of the two measured components, apparently near in value to the axial component). The

SMD is lower in the phase angles and radial locations where the velocity is higher, as already briefly observed in Figure 4.29, due to the size-velocity correlation of the spray explained in Figure 4.9. Taking this into account, the SMD indeed shows a local minimum near X = -5 mm, in the location where the axial velocity shows a local maximum.
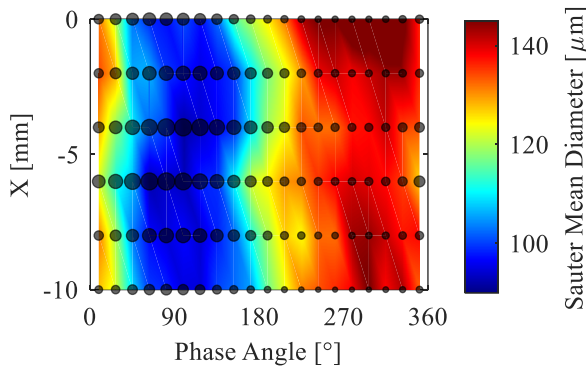
Figure 4.32: Periodic oscillation of Sauter Mean Diameter along the radial direction (qualitative total velocity trend on black dots) at Z = 40 mm.

Following a similar procedure to the analysis at the spray centre in 4.3.1, the mass flux of the spray can be calculated by utilizing the measured droplet velocities and diameter, in combination with the rest of the PDA system's data. The resulting mass flux in this subsection 4.3.2 is presented as a contour for all six measured radial locations, and the outcome is presented in Figure 4.33. The phase-averaged mass flux is periodically oscillating in all radial locations similar to the behaviour shown in Figure 4.27 for X = 0 mm, while it tends to reach near zero values at the edge of the spray at X = -10 mm, as expected from the non-forced case of Figure 4.10. The average value for each position also coincides with the value of the non-forced case, providing another indication

that the spray produced is of similar quality, but the droplets travel along the pulsating flow and reach the measurement volume of the PDA system with a time delay. The black dots on these graphs qualitatively depict the oscillation of the SMD for each measured position, showing the influence of the diameter over the velocity for the mass flux calculation.
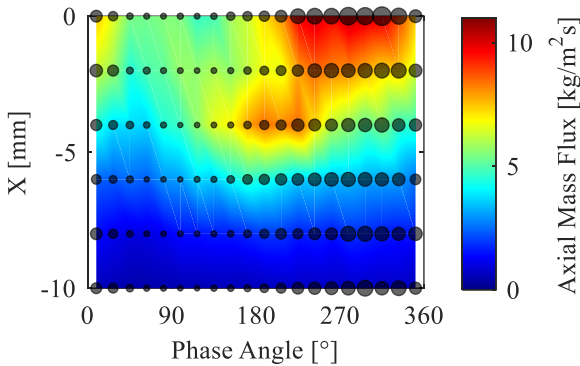
Figure 4.33: Periodic oscillation of the spray mass flux along the radial direction (qualitative SMD trend on black dots) at Z = 40 mm.

To conclude with the analysis of the spray characteristics in the radial direction, the local air-to-liquid mass flow ratio can be calculated by using the already-known mass flux. The same procedure followed in 4.3.1.2 using Eq.(4.7) was applied in order to obtain the local ALR and its periodic fluctuation in the six radial positions. For the air velocity, the data of Figure 4.15 were used. The outcome is presented in the contour of Figure 4.34. A strong periodic oscillation is observed in all different positions, starting from very low average values at the centre of the spray at X = 0 mm, ending in values higher than 100 at the edge of the measured interval at X = -10 mm. This was expected since the spray is dense close to its centreline and even

though it does spread along the radial direction as well, the mass flux there is radically decreasing (Figure 4.33, or Figure 4.10 for the non-forced case). The colour map in Figure 4.34 is on a logarithmic scale, in order to better visualize the periodic fluctuation in all locations along the radial direction.
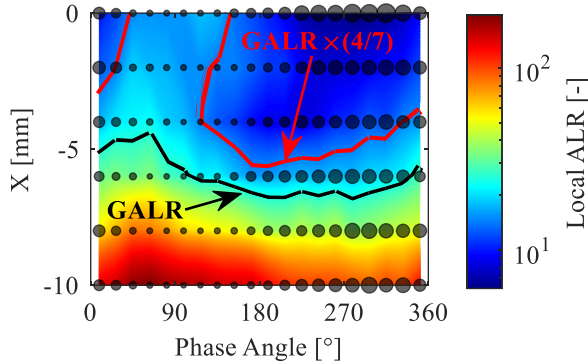
Figure 4.34: Periodic oscillation of the local ALR along the radial direction (qualitative SMD trend on black dots) at $Z = 40$ mm.

On the same graph, two iso-ALR lines have been highlighted. The black one refers to the average global ALR (GALR) of the system, i.e. the total average mass flow rate of the air supplied in the system over the total water mass flow rate. The red line is the specific 4/7 fraction of the GALR, as discussed in Figure 4.28. These two lines on the contour of the ALR oscillate around the positions -6 mm for the GALR and -3 mm for the 4/7 fraction of the GALR.

Finally, it is useful to compare the basic spray characteristics under non-forced conditions presented in 4.1.2 with the results of the average oscillating spray characteristics of this subsection. Comparing the conditions for subsection 4.1.2 presented in Table 5 with the respective conditions regarding 4.3.2 in

Table 7, it is evident that the measured locations as well as the average air and water flow conditions are the same. The mean total droplet velocity is juxtaposed with the SMD of the spray in Figure 4.35 for all six radial locations. As already observed by comparing the results of subsection 4.3.2 to those of subsection 4.1.2, the same behaviour of the spray characteristics was found in the forced and non-forced cases. For this reason, the average velocity of the spray and the SMD of the spray on each position for the forced flow experiments shown in Figure 4.35 are treated as if they behaved quasi-steady.
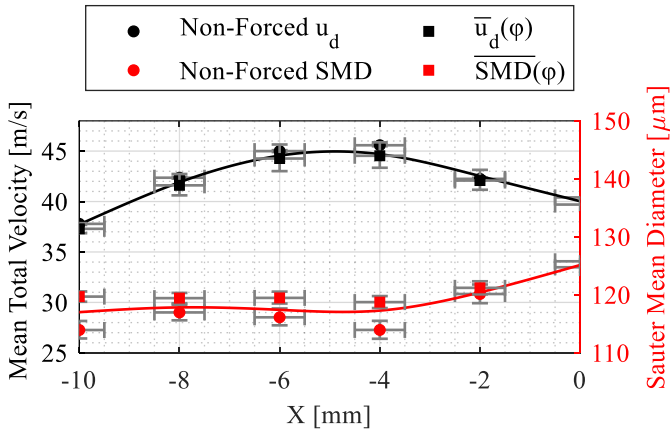
Figure 4.35: Mean total droplet velocity and SMD along the radial direction for forced and non-forced conditions at $Z = 40$ mm.

Since the behaviour match between the two cases was established, it is interesting to quantify how strong the fluctuation of each of the spray characteristics is. By calculating the amplitude of the oscillation for the velocities, the angle, the SMD, the mass flux, and the local ALR, on each of the six measurement positions, it is possible to examine and compare how

influenced they were due to the air forcing. For the mean vertical droplet velocity and the SMD, the average of the forced case has already been shown to match the non-forced values in Figure 4.35, while the same applies to all other spray characteristics. Therefore, the amplitude of each parameter for each position was calculated as a percentage relative to their average value and presented in Figure 4.36. The velocity angle has the lowest and less significant relative amplitude since it was already established that it remains almost constant in time. The two velocity components oscillate with an amplitude near 18% of their average, while for the SMD the relative amplitude is approximately 20%. The spray mass flux has a significantly higher relative oscillation amplitude compared to the other spray characteristics, reaching values of 40%. As a result, the local ALR also oscillates with a high amplitude, between 40% and 55%. Such a strong oscillation in the local ALR would influence the flame stability and potentially risk the engine hardware.
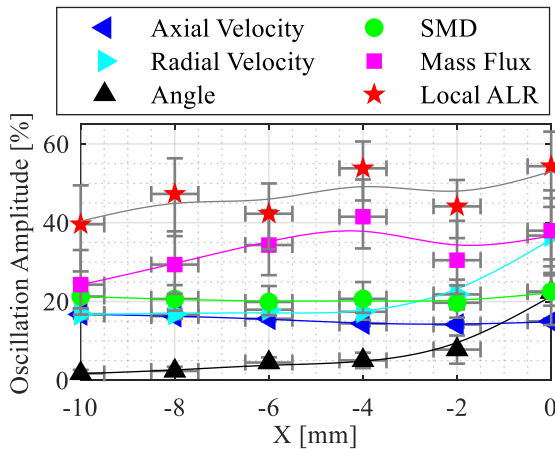
Figure 4.36: Relative amplitudes of the phase-averaged main spray characteristics at Z = 40 mm.

4.4   Spray Characterization under Varying Conditions

4.4.1   Influence of Excitation Frequency on the Spray Characteristics

Since the spray has been extensively characterized at a single frequency in section 4.3, the final step was to investigate the influence of the excitation frequency [177]. As described in subsection 4.2.2 and summarized in Table 7, the experimental investigations of this subsection consider four different cases with excitation frequencies of approximately 100 Hz difference from one another at a constant oscillation amplitude. The results of the spray response via its basic characteristics are summarized and discussed in this section. As indicated in Table 7, this investigation considers the same radial distance from X = -10 mm to X = 0 mm as in subsection 4.3.2. However, for practical reasons in visualizing these results, only figures regarding three discrete locations are displayed: at X = 0 mm, at X = -5 mm, and at X = -10 mm.

The phase-averaged axial droplet velocity at the four frequencies studied was calculated and shown in Figure 4.37, for the three radial positions selected. As it was already evident from the droplet velocity in the single frequency spray characterization in section 4.3, the shape of the curves is close to the ideal sinusoidal shape at the lowest frequency of 102 Hz but deviates as the frequency increases. This is due to the response of the spray to the imposed excitation at the higher frequencies [149,170]. As the frequency increases, the phase difference between the maximum and the minimum of the oscillation during the period becomes larger. Furthermore, similar behaviour is observed in Figure 4.37(a), (b) and (c) in terms of the average velocity trend.

(a)

(b)

(c)
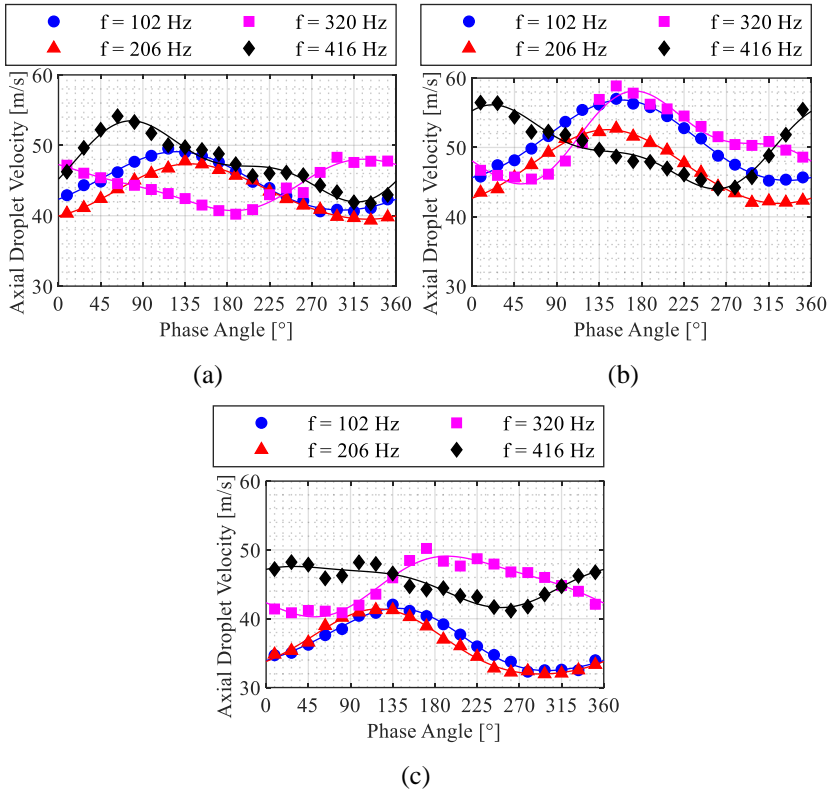
Figure 4.37: Phase averaging of axial droplet velocity for a variety of excitation frequencies at Z = 40 mm and (a) X = 0 mm, (b) X = -5 mm, and (c) X = -10 mm.

As shown in subsection 4.3.2, approximately 5 mm away from the centreline the axial droplet velocity is higher on average compared to the velocity at X = 0 mm and X = -10 mm; this is observed in Figure 4.37 as well for all four excitation frequencies examined. In Figure 4.37(c) specifically, the axial velocity component for the higher frequencies is higher, showing a more uniform distribution of the velocity along the radial direction.

To provide further insight into the droplet velocity behaviour, since the spray in this section was analysed along the X-axis as well, the radial velocity component was also measured. This velocity component is shown in Figure 4.38 for the three selected radial locations. As expected from the previous outcomes, the radial component increases in absolute value when moving radially from the centreline at X = 0 mm.

(a)

(b)

(c)
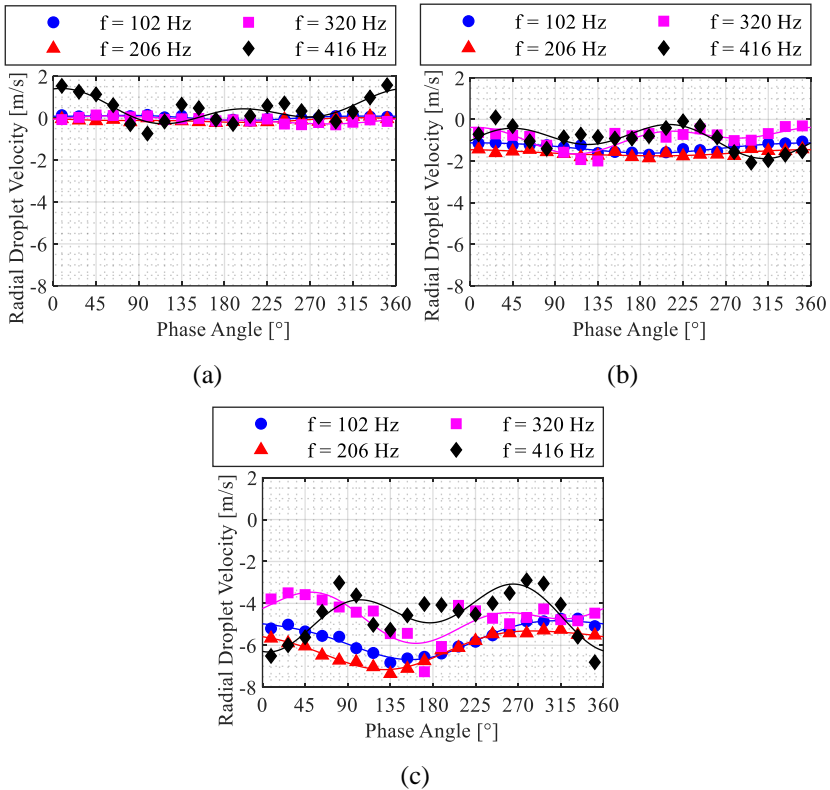
Figure 4.38: Phase averaging of radial droplet velocity for a variety of excitation frequencies at Z = 40 mm and (a) X = 0 mm, (b) X = -5 mm, and (c) X = -10 mm.

The absolute amplitude of the oscillation in radial velocity increases as the absolute mean value increases from X = 0 mm to X = -10 mm. However, in Figure 4.38(a) the amplitude of the case with the highest excitation frequency of 416 Hz is significantly higher than in the other frequencies where it is negligible, showing an instability of the spray in the radial direction as well. In Figure 4.38(b), this instability starts to become apparent for the 320 Hz case as well while the two lowest frequencies maintain a negligible amplitude. This indicates that the spray behaviour changes along the radial direction for higher excitation frequencies. Finally, in Figure 4.38(c) the absolute value of the radial velocity for the cases of the two higher frequencies is smaller than the lower frequencies. The opposite trend was observed for the axial velocity in Figure 4.37(c), highlighting that as the excitation frequency increases, the radial structure of the spray changes.

The combined behaviour of the two velocity components results in a variation in the mean velocity angle along the radial direction, which is presented in Figure 4.39 for the four examined cases. As described in the spray analysis at one frequency along the radial direction in subsection 4.3.2, the spray angle increases in absolute value with increasing distance from the centre of the spray. Similarly to the previous findings, negligible fluctuations were observed throughout the oscillation period because the fluctuations of the two velocity components counter each other. However, the outcome observed in the radial velocity component from Figure 4.38 is also evident; the velocity angle is more unstable at the higher excitation frequencies, even at X = 0 mm. Furthermore, the angle at the edge of the spray shown in Figure 4.39(c) for the cases of 320 Hz and 416 Hz is smaller in comparison to the cases of 102 Hz and

206 Hz. This further supports the hypothesis that the spray structure undergoes a change in the radial direction as the excitation frequency increases.

(a)

(b)

(c)
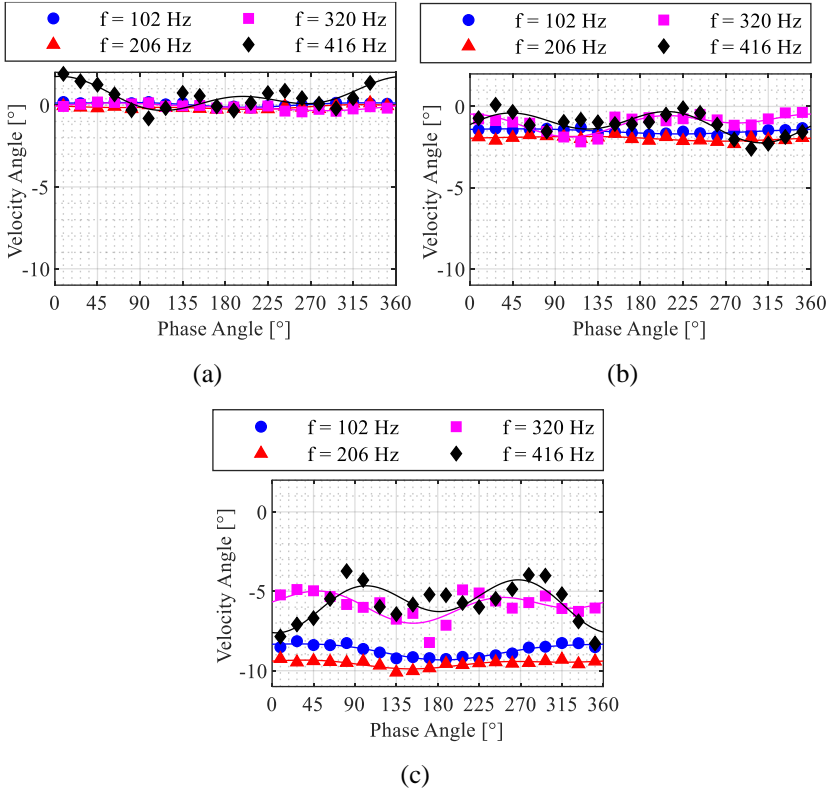
Figure 4.39: Phase averaging of droplet velocity angle for a variety of excitation frequencies at Z = 40 mm and (a) X = 0 mm, (b) X = -5 mm, and (c) X = -10 mm.

A valuable characteristic measure of a spray is the SMD, and in this study, its variation in time is of particular interest. Figure 4.40 shows the periodic fluctuation of the SMD of the spray for the four frequencies examined. In all four cases at X = 0 mm, the influence of the air modulation is obvious; as the radial distance increases.

(a)

(b)

(c)
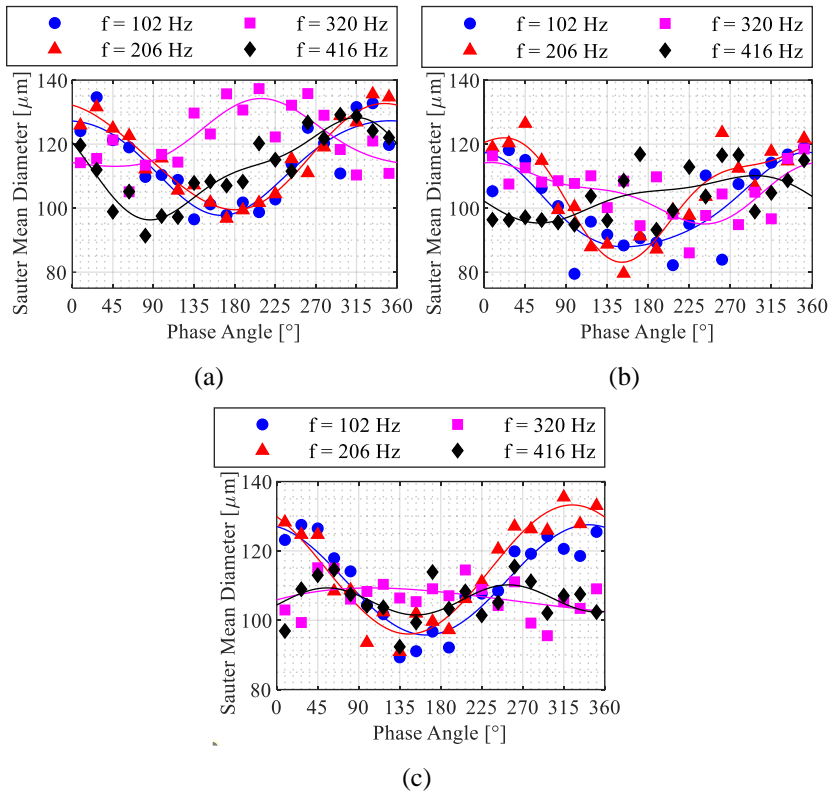
Figure 4.40: Phase averaging of SMD for a variety of excitation frequencies at Z = 40 mm and (a) X = 0 mm, (b) X = -5 mm, and (c) X = -10 mm.

However, the SMD becomes more unaffected by the excitation at the higher frequencies. In previous experiments on a similar model prefilmer using Shellsol D70 as a liquid, it was shown that the SMD tends to remain constant in time for excitation frequencies around 300-500 Hz with an average airflow velocity of 40 m/s [176].

Nevertheless, in this investigation where the average air velocity is significantly higher as shown in section 4.2, it is observed that even at 416 Hz the oscillation amplitude is similar to the lowest frequency case at the centre of the spray. Only at increased radial distances, in Figure 4.40(b) and especially Figure 4.40(c) does the SMD become unaffected by the excitation at the frequencies of 320 Hz and 416 Hz, leaning towards the observations of Müller. The slight drop of the SMD at X = -5 mm in Figure 4.40(b) compared to Figure 4.40(a) matches the observed behaviour from the previous investigations of subsections 4.1.2 and 4.3.2. Establishing the behaviour of the velocity components and the SMD under the influence of various excitation frequencies, the mass flux was the reasonable next step for the processing of the data. Following the same method as the analysis at the spray centre in 4.3.1, the total spray mass flux was calculated and presented in Figure 4.41 for the three selected locations along the X-axis. Despite a steady flow rate of water in the atomizer, the spray mass flux periodically fluctuates at all four excitation frequencies. This indicates that even at 416 Hz, the prefilmer accumulates liquid and releases it in waves as hypothesized in the previous sections. Nevertheless, spray mass flux or equivalence ratio oscillations can also be created by an oscillating airflow via convection by the mean flow [178,179]. When building and scaling the prefilmers for engine applications, this should be undoubtedly a factor to consider for jet engine safety.
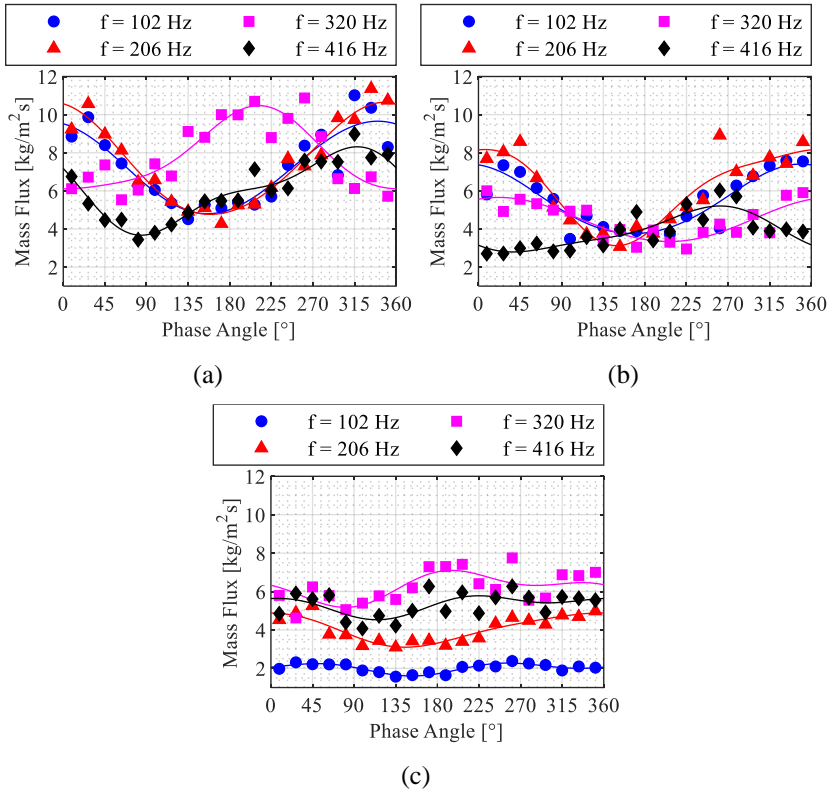
Figure 4.41: Phase averaging of spray mass flux for a variety of excitation frequencies at Z = 40 mm and (a) X = 0 mm, (b) X = -5 mm, and (c) X = -10 mm.

In Figure 4.41(b), and subsequently in Figure 4.41(c), the spray mass flux is smaller on average in all four cases compared to the centreline at X = 0 mm. This was expected, at least for the low frequencies, since the spray produced by this type of prefilmer is denser along the centreline as shown in the previous subsections. However, at the higher frequencies of 320 Hz and 416 Hz, the distribution of the mass flux along the radial direction is more uniform, as already noted in the discussion regarding Figure 4.37.

145
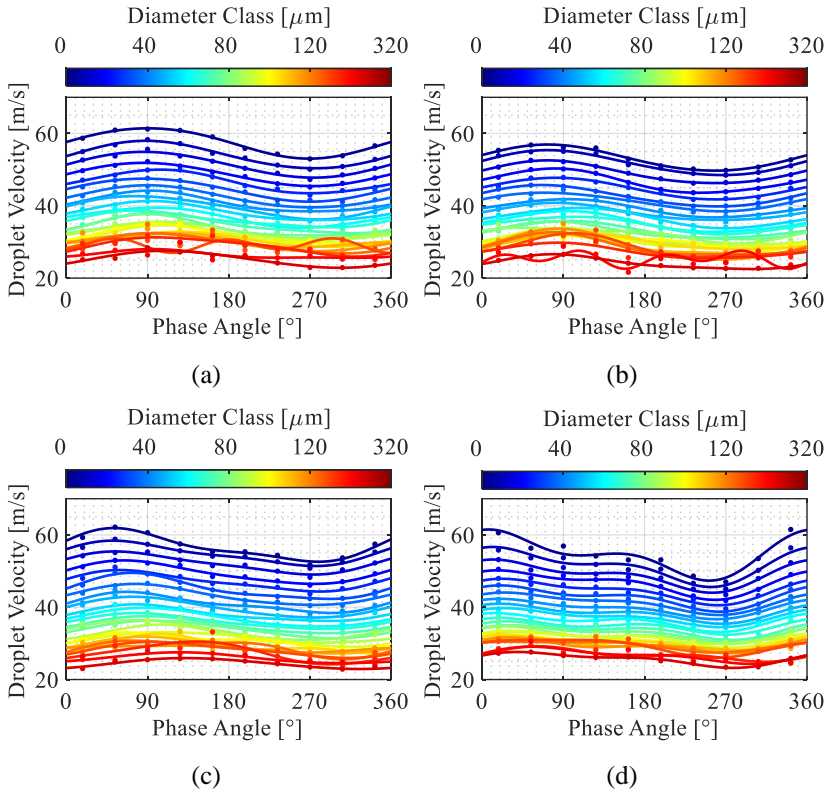
Figure 4.42: Mean droplet velocity of various diameter classes at Z = 40 mm and X = 0 mm for excitation frequency (a) 102 Hz, (b) 206 Hz, (c) 320 Hz and (d) 416 Hz.

Having established how the basic spray properties are affected by the excitation frequency, it is useful to examine the mean droplet velocity in more detail, considering the different size classes in a similar way to Figure 4.21. Figure 4.42(a) shows the size class separation of the mean droplet velocity for the excitation frequency of 102 Hz, at X = 0 mm. Each size class is represented by a single curve in a diagram. As also observed in Figure 4.21, the larger droplets have a smaller average velocity and the smaller droplets move faster.

In addition, a phase shift is visible between the smallest and the largest droplets, which was to be expected since large droplets cannot perfectly follow the rapidly changing flow field due to their inertia and corresponding Stokes number [149].

As the excitation frequency increases from the 102 Hz in Figure 4.42(a) to the 416 Hz in Figure 4.42(d), a number of outcomes arises. Naturally, the same behaviour is observed with respect to the average velocity for larger droplets. However, the phase shift between the different size classes is even bigger. This is explained by the fact that the velocity of the air changes approximately four times faster in the case of 416 Hz compared to the 102 Hz case. Therefore, the delay of the large droplets is even more pronounced due to their inertia. Moreover, the shape of the droplet velocity curve deviates even more from the sinusoidal shape at higher frequencies, as already observed in Figure 4.37.

4.4.2   Numerical Validation

The behaviour of the droplet velocity as a function of size class can be numerically validated by using the equation of motion for a single droplet, considering the forces acting on the droplet as it moves as shown in Figure 4.43. The drag force F_D acting on the droplet is caused by the airflow, F_W is the weight of the droplet and F_B is the buoyant force. Considering these three forces, the motion equation is derived as follows:

$$m\frac{\partial u_d(t,z)}{\partial t} = F_D\big(u_d(t,z)\big) + F_W - F_B \tag{4.8}$$

where m is the mass of the droplet, and u_d is its velocity as a function of time t and distance z.
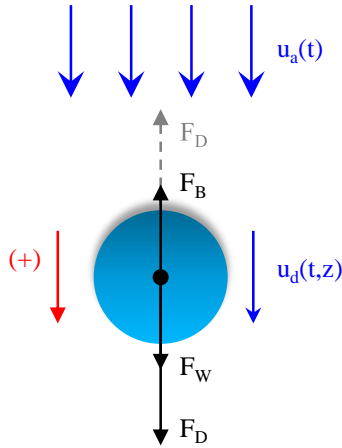
Figure 4.43: Forces acting on a moving droplet in one direction.

The forces of Eq.(4.8) are all dependent on the droplet's surface area A, mass m, or volume V:

$$F_D(t, z) = \frac{1}{2} \rho_A \big(u_A(t) - u_d(t, z)\big)^2 c_D A \tag{4.9}$$

$$F_W = m\,g \tag{4.10}$$

$$F_B = \rho_A V\,g \tag{4.11}$$

All three of m, A, and V can be expressed as a function of the droplet diameter d, while the density of the droplet ρ_d also emerges as a part of its mass definition. Therefore, the equation of motion for a single droplet is described as follows [180]:

$$\frac{\partial u_d}{\partial t} = \frac{3}{4} \frac{c_D}{d} \frac{\rho_A}{\rho_d} (u_A - u_d)|u_A - u_d| + g\left(1 - \frac{\rho_A}{\rho_d}\right) \tag{4.12}$$

For the air velocity $u_A(t)$, a fit on the experimental data of subsection 4.2.2 was considered in order to numerically solve Eq.(4.12) for $u_d(t)$, the droplet velocity. For the drag coefficient c_D, a function of the droplet Reynolds number was used, as modelled by Almedeij [181]. In solving the equation of motion of the droplet, of interest in this context is the velocity of the droplet at the downstream distance $Z = 40$ mm, which agrees with the experimentally measured position.
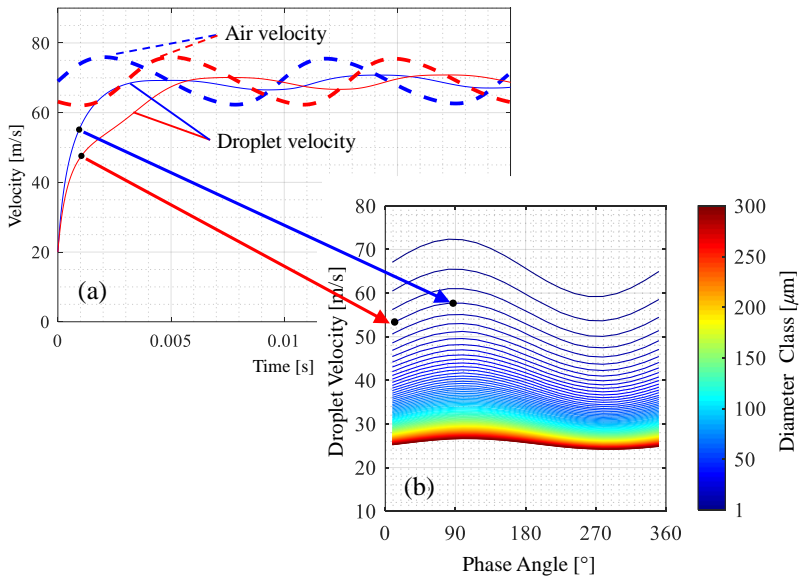
Figure 4.44: Numerical solution of droplet motion equation at $Z = 40$ mm for various air velocity initial conditions.

Figure 4.44(a) shows the numerical solution of Eq.(4.12) illustrated with the solid lines, i.e. the droplet velocity over time as the droplet moves. There are two solutions shown for two different initial conditions concerning the phase of the air velocity at $t = 0$ s, for a droplet of a determined diameter. Depending

on that initial phase shift of the air velocity, which is shown in dashed lines of red and blue colour, the corresponding solution for the droplet velocity is shown in solid lines with the respective colours. The black dots marked on the solution curves denote the instant at which the droplet reaches the $Z = 40$ mm milestone, which is the location of interest. Therefore, solving Eq.(4.12) for multiple initial conditions regarding the air velocity phase, the droplet velocity at $Z = 40$ mm is shown in Figure 4.44(b) as it changes over a period. The different lines on this diagram denote the numerical solution for various droplet diameters.

The equation of motion was solved for several droplet diameters from 1 μm to 300 μm and numerous phase angles as an initial condition. The outcome is represented in Figure 4.45, for the four excitation frequencies selected for the experimental campaign described in this section. In the case of 102 Hz in Figure 4.45(a), the phase shift between the different droplet sizes is definitely present, but rather small, as also observed in the corresponding experimental case of Figure 4.42(a). As the frequency increases from Figure 4.45(a) to Figure 4.45(d), this phase shift is more pronounced.

The exact match of the colour scale between the figures showing the experimental and the numerical results was not accomplished for technical reasons. Since the experimental data are limited and because of the typical droplet diameter distribution (e.g. Figure 4.24), the larger droplets are much fewer than the smaller droplets. Therefore, the separation in diameter classes for Figure 4.42 was done with a constant step of 5 μm until 140 μm, and then one final group containing the rest of the droplets with d > 140 μm.
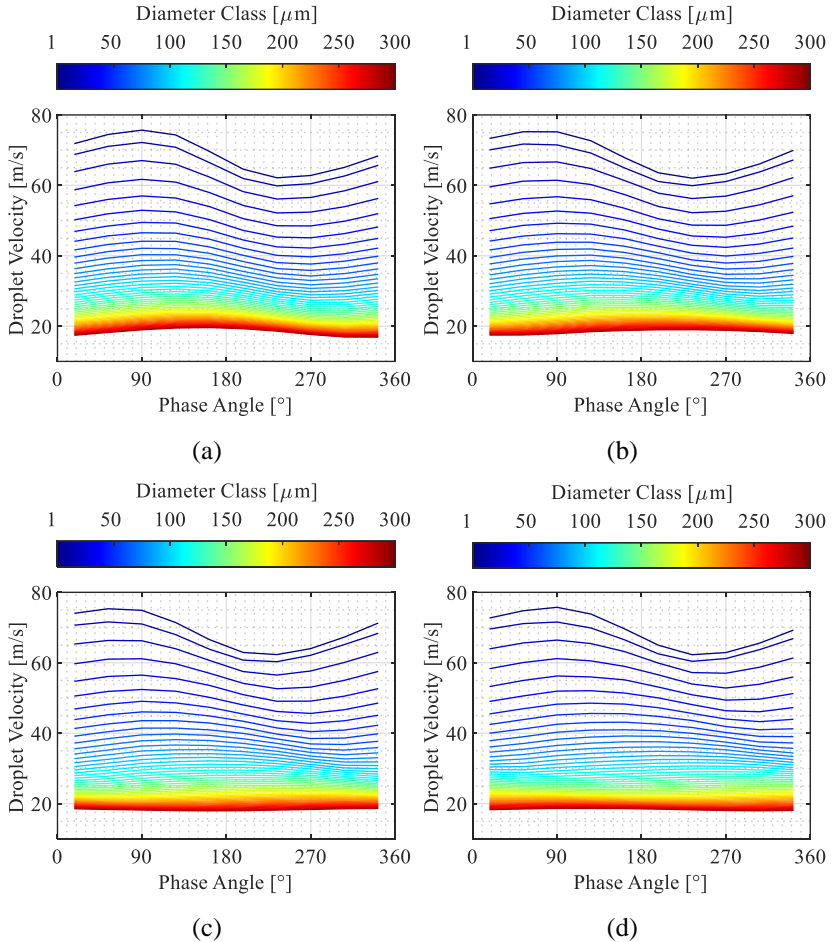
Figure 4.45: Numerical solution of droplet motion equation at Z = 40 mm of various diameters for excitation frequency (a) 102 Hz, (b) 206 Hz, (c) 320 Hz and (d) 416 Hz.

On the other hand, the calculations for the results of Figure 4.45 do not have such a restriction since Eq.(4.12) can be solved for multiple diameters; therefore, many more diameters are presented with a constant step from 1 μm

to 300 μm. It is worth mentioning that apart from confirming the trend of the experimental results, the velocity values also agree in most size classes when comparing the numerical (Figure 4.45) with the experimental (Figure 4.42) results.

Since a phase difference between the droplet velocities has been observed in the previous diagrams as the excitation frequency increases, an estimation of that phase difference was performed. This phase difference was calculated as the difference of the phase angles that resulted from a fast Fourier transform on the velocity curves of Figure 4.45. Because Eq.(4.12) can be solved for different initial droplet velocities, three different values were considered for the calculation of the phase difference. Figure 4.46 shows a polar diagram depicting the phase difference of the droplet velocities at $Z = 40$ mm calculated from Eq.(4.12) for a droplet velocity initial condition of $u_0 = 1$ m/s.

The radial axis represents the droplet diameter while the angular axis shows the calculated phase difference. Each point on the curves denotes the phase difference between the velocity of a droplet whose diameter corresponds to the radial coordinate of that point and the velocity of a reference droplet with $d = 0.01$ μm. The four curves represent the four different excitation frequencies studied in this section. Figure 4.46 quantifies the trend observed in Figure 4.42 and Figure 4.45, showing an increasing phase difference in the droplet velocity as the diameter increases, for all four excitation frequencies. Considering larger droplets, the increase of that phase difference as the frequency increases is more evident than that of the smaller droplets. For example, for droplets of 300 μm the phase difference at 102 Hz is 73° and at 206 Hz is almost double at 150°, at 320 Hz it is 273° and at 416 Hz it is 33°, surpassing the 360° reference.
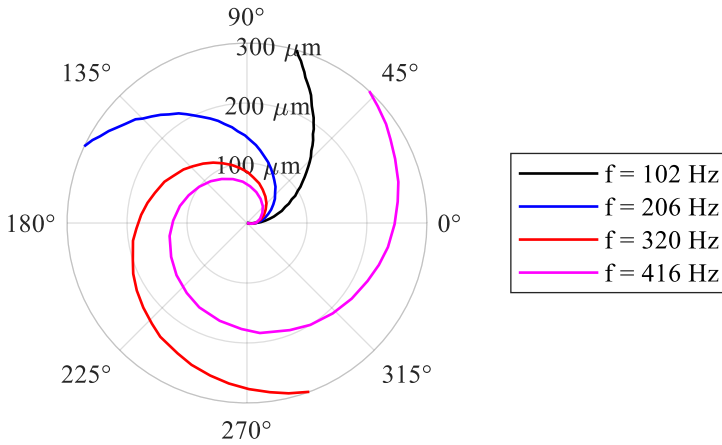
Figure 4.46: Phase difference of each diameter with the smallest (0.01 μm) for the four examined frequencies and initial velocity of 1 m/s.

Considering higher initial velocities when solving Eq.(4.12), the same phase difference is shown in Figure 4.47 and Figure 4.48, for $u_0 = 5$ m/s and $u_0 = 10$ m/s respectively. In both figures, the calculation was applied for all four excitation frequencies. As observed, the phase differences for the same diameters and frequencies are smaller as the initial velocity increases. This is explained due to the fact that especially larger droplets accelerate slower due to their inertia, so if they already travel with a higher velocity at $t = 0$ s, they will not lag behind the small droplets as much as if they had a low initial velocity. Comparing the curves of Figure 4.48 and Figure 4.46, this is indeed more pronounced for the big diameters, especially for the low-frequency case of 102 Hz. At lower droplet sizes, e.g. $d < 100$ μm, the difference in the result between the $u_0 = 1$ m/s and the $u_0 = 10$ m/s case is significantly smaller than considering droplet sizes in the range of 200 μm $< d < 300$ μm.
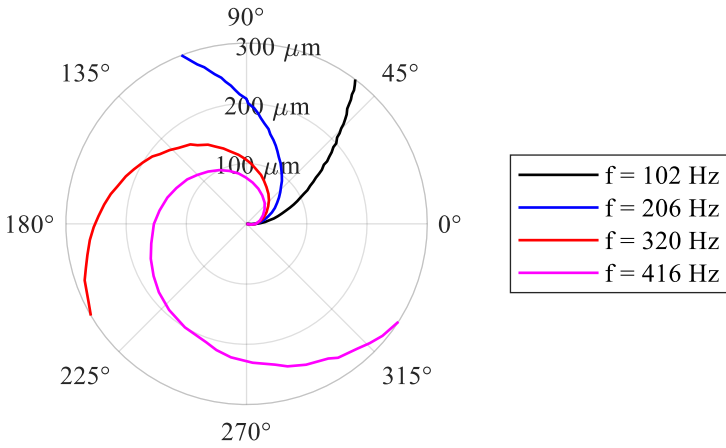
Figure 4.47: Phase difference of each diameter with the smallest (0.01 μm) for the four examined frequencies and initial velocity of 5 m/s.
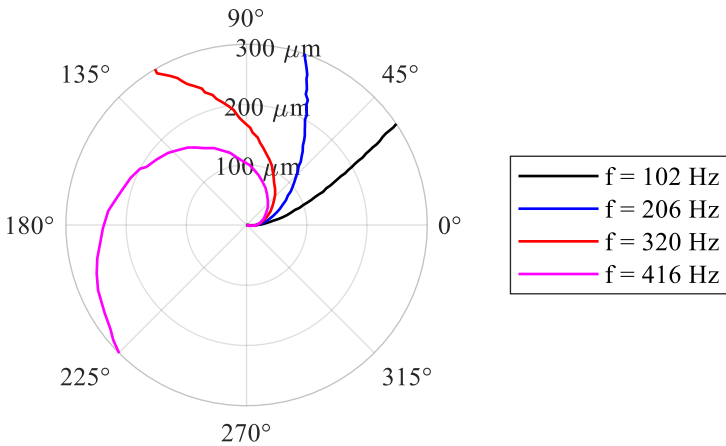
Figure 4.48: Phase difference of each diameter with the smallest (0.01 μm) for the four examined frequencies and initial velocity of 10 m/s.

Finally, considering the phase difference between a large droplet diameter of 300 μm and the reference of 0.01 μm, the polar diagram of Figure 4.49 illustrates the influence of the excitation frequency on the radial axis.
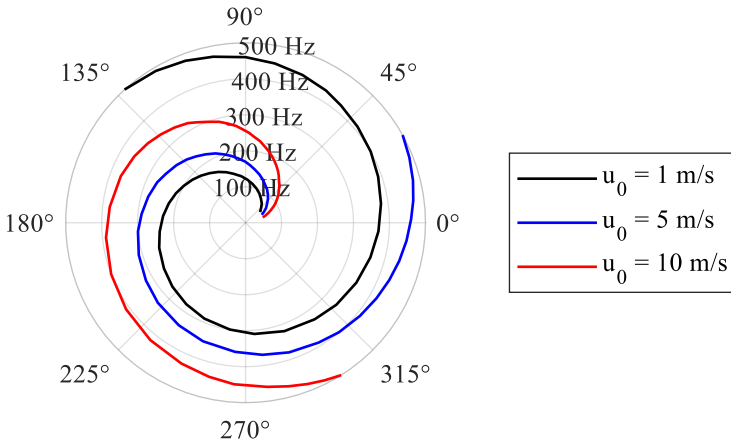
Figure 4.49: Phase difference of the largest diameter (300 μm) with the smallest (0.01 μm) for frequencies in the range of 50 to 500 Hz for three different initial velocities.

The three curves drawn represent the initial velocities of 1 m/s, 5 m/s and 10 m/s, to correlate this polar diagram with the previous three figures. This diagram shows frequencies from 50 Hz to 500 Hz, which was the range of interest, as explained already and investigated in subsection 4.2.2. It is evident that as the excitation frequency increases, the lag of the large droplets becomes significantly higher. This was expected due to the inertia of the very large droplets compared to the small ones as already mentioned. Especially when the initial velocity is low at 1 m/s, the phase difference crosses the 360° milestone at a much lower frequency at approximately 385 Hz compared to the 470 Hz of the 5 m/s case. In the case where the initial velocity is as high as

10 m/s, the large droplets of 300 μm never exceed the 360° phase difference with the reference small droplets as also observed in Figure 4.48.

Utilizing the data of Figure 4.49, a prediction model of the phase difference was created to account for both parameters of the excitation frequency and the initial velocity. Such a model for the phase delay of the velocity of a 300 μm droplet compared to a 0.01 μm droplet must include a power correlation for both variables, in order to satisfy their opposite trend where the phase difference increases with increasing frequency but decreases with increasing initial velocity.

$$\Delta\Phi_{300\mu m} = 17.34 + 7.155u_0^{-14.34} + 0.0871f^{1.393} - 0.0453u_0f \tag{4.13}$$

This model described in Eq.(4.13) is illustrated as a surface fit on the data of Figure 4.49 in Figure 4.50. This model is applicable only within the range of 50 to 500 Hz and 1 to 10 m/s, with a R² value for the fit of 0.9957.
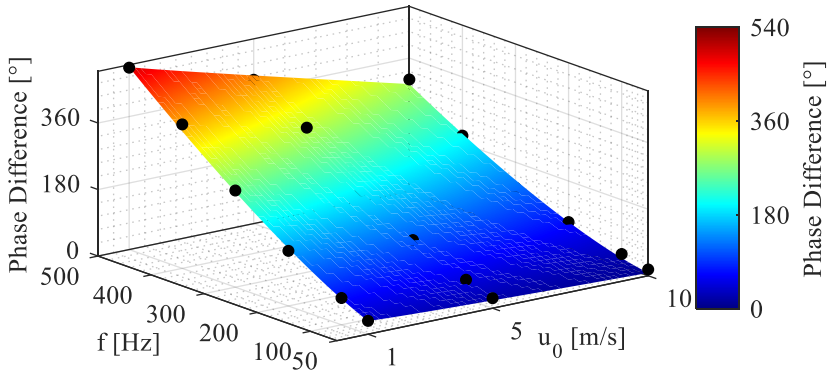
Figure 4.50: Phase difference of largest diameter with smaller as a function of excitation frequencies and initial velocities in the range of 50 to 500 Hz and 1 to 10 m/s respectively.

4.4.3   Influence of ALR on the Spray Characteristics

Having analysed the influence of the excitation frequency on the spray characteristics, the variation of the average global ALR is of interest for a more complete systematic variation. Table 8 shows the operating conditions for the spray tests conducted at the three selected water flow rates. In all three cases, the average pressure drop across the nozzle was constant, as well as the excitation frequency.

Table 8: Operating conditions for the average ALR variation tests.

Case	f [Hz]	X [mm]	Y [mm]	Z [mm]	$\overline{\Delta p / p}$ [%]	$\dot{V}/b$ [mm²/s]	$\overline{GALR}$ [-]
A						55.67	38
B	102	0	0	40	3	83.5	26
C						111.3	19

By increasing the film load from 55.67 mm²/s to 111.3 mm²/s, the average global ALR is reduced by half. These tests are presented at X = 0 mm in this section; since the spray angle changes with different water flow rates, the analysis at further radial positions would not provide a fair comparison between the three cases.

The phase-averaged droplet velocity at the three different water flow rates studied is shown in Figure 4.51. With increasing liquid supply, the mean velocity reduces due to the inertia of the droplets. This is expected from a macroscopic point of view considering the conservation of momentum since the air mass flow rate is the same but the liquid mass flow rate is reduced as the ALR increases. The three cases show a similar phase angle without major

differences from reference case B, indicating that the phase-averaged mean droplet velocity does not lag behind in phase due to the variation of the total liquid supply in the atomizer.
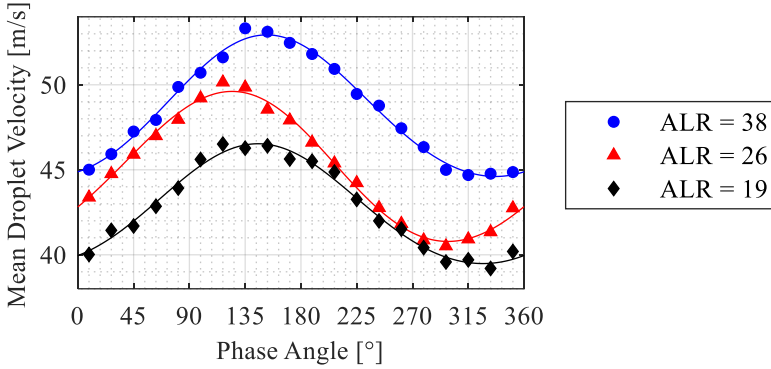
Figure 4.51: Phase-averaged droplet velocity for a variety of ALR.
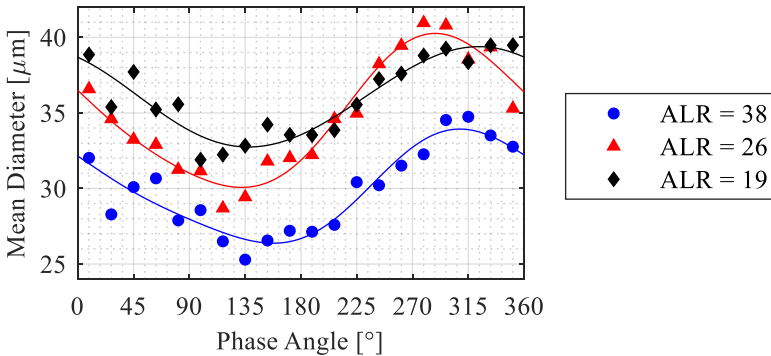
Figure 4.52: Phase-averaged droplet diameter for a variety of ALR.

Figure 4.52 shows the mean diameter and Figure 4.53 the SMD for the three examined cases with a varying ALR. In all cases, the mean diameter and the

SMD fluctuate periodically and show similar behaviour, with a slightly lower oscillation amplitude as the water flow rate increases. The mean diameter shows a distinct change on its average, with an opposite trend to the mean velocity. This is expected due to the already established inverse proportionality between the spray velocity and its sizes; the same trend remains as the global ALR of the system varies.
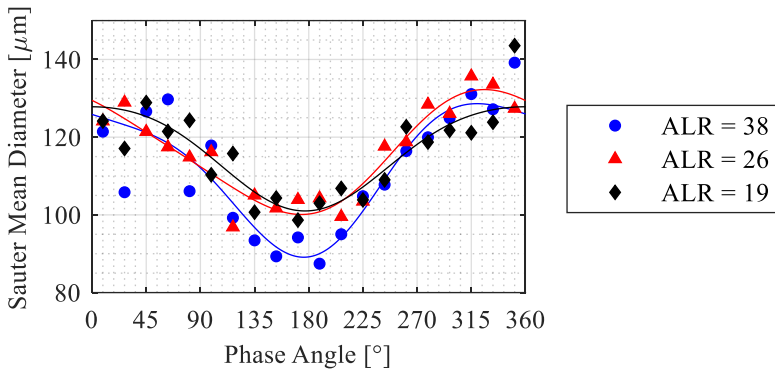
Figure 4.53: Phase-averaged SMD for a variety of ALR.

Nevertheless, no significant difference is observed in Figure 4.53 for the average SMD between the three cases. The small increase of the SMD with an increased liquid flow rate at constant airflow pressure was already observed in the literature, whereas a more significant increase in the SMD occurs with a decreased ALR but under a constant liquid flow rate [182,183]. This relationship between the SMD and the liquid flow rate may be explained due to the difference in the spray structure and its spatial distribution when the liquid mass flow rate changes substantially.

Finally, the spray mass flux is shown in Figure 4.54. In all three cases, the resulting mass flux periodically oscillates based on the excitation frequency imposed, similar to the reference case B of Table 8 which is identical to the first case of Table 7 referring to section 4.4. As expected, with increasing water flow rate, the local mass flux also rises. This increase, however, is not as significant, due to similar reasons explaining the SMD behaviour, namely the difference in the spray structure.
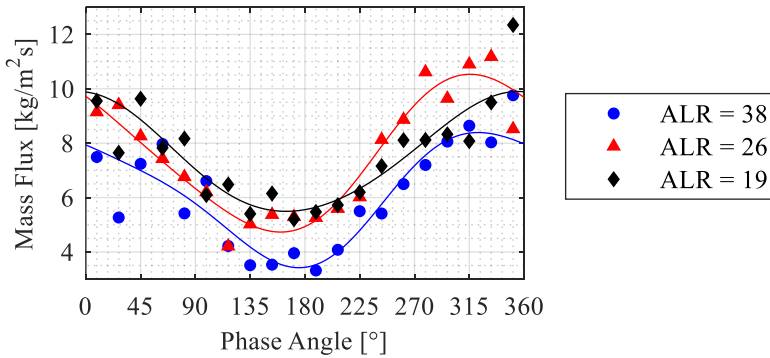
Figure 4.54: Phase-averaged spray mass flux for a variety of ALR.

5   Summary and Outlook

The focus of the investigations carried out in this work was the experimental characterization of the behaviour of an airblast prefilming atomizer under the influence of a periodically oscillating airflow. The investigations were accomplished in a setup without a reacting flow, studying the response of the spray characteristics and hence the ALR as a separate phenomenon. The purpose of these investigations was to provide insight into the instability phenomena usually occurring in jet engine combustors operating under the LPP premise at high pressures.

Due to the high complexity of the interpretation of the phenomenon in a 3D flow of a swirling airblast atomizer, an airblast prefilming atomizer with a two-dimensional flow was developed for this purpose. The liquid film was located between two air ducts, which led into a free jet. A pulsation device was implemented on the experimental setup, which was able to produce an airflow of an almost ideal sinusoidal velocity. The excitation frequency of this modulation was dependent on the rotational speed of the attached servomotor, controlled via computer software, while the average air velocity and its amplitude were dependent on the total system airflow and the percentage of the air flowing through the siren respectively.

To first establish the model prefilmer's performance and the produced spray quality under non-oscillating conditions, experiments were accomplished without the operation of the pulsating device. The measurement techniques used for this experimental campaign spray under steady conditions were

shadowgraphy imaging and Phase Doppler Anemometry. With shadowgraphy, the primary breakup was initially investigated under various air-to-liquid ratio conditions, showing a decreasing breakup length with increasing ALR under constant pressure drop across the nozzle. Furthermore, the spray was analysed in its whole extent along the axial and radial direction, showing a symmetrical behaviour around its centreline at $X = 0$ mm. Across the radial direction (i.e. across the X-axis) the mean droplet velocity was increasing until reaching a local maximum, the SMD was decreasing until reaching a plateau, while the spray density was constantly decreasing until the edge of the spray limits. The same trend on the spray characteristics was observed in the PDA measurements as well, where the mass flux was also calculated and the outcome was verified with the mass flow rate supplied in the atomizer. The correlation between the droplet velocity and diameter considering the whole spray was analysed and an inverse proportionality was observed.

The subsequent experimental campaign was planned to investigate the performance of the pulsating device in order to determine the operating conditions for the following spray characterization experiments. The air velocity was measured via a hot-wire Constant Temperature Anemometer, a technique able to detect with great accuracy the oscillations of the flow. A range of low excitation frequencies was initially examined, maximizing the oscillation amplitude in order to trigger a distinct influence on the spray. The frequency of 120 Hz was selected as an optimum case between the examined options, combining a high amplitude and a negligible presence of harmonics. The second part of this campaign intended to investigate a larger spectrum of frequencies from 50 to 500 Hz, in order to find four different excitation frequencies with a difference of approximately 100 Hz from one another at a

constant amplitude so that the frequency influence on the spray could be studied. The selected cases were at 102 Hz, 206 Hz, 320 Hz, and 416 Hz.

The spray characteristics were measured under atmospheric conditions by means of PDA under oscillating flow conditions at 120 Hz. The discussion of the experimental results can be summarized in the following conclusions:

- The mean diameter, SMD, and mean droplet velocity indeed oscillate at the same frequency as the air velocity.

- The SMD measured for the average air velocity in a non-forced flow experiment matches the corresponding average SMD, indicating a spray of similar quality between the two cases.

- The SMD could also be calculated from the correlation proposed by Gepperth et al. [103], using the experimentally measured oscillating air velocity as an input. Its average value is slightly higher than the SMD of the average air velocity calculated from the equation, replicating the experimental observations and strengthening the aforementioned argument.

- The SMD and the mean diameter of the droplets have a natural shift of approximately 180° compared to the droplet velocity.

- The inverse proportionality of the droplet velocity and diameter was once more established, by dividing the spray into various size classes and observing the mean velocity of each size class.

- The main spray characteristics behave quasi-steady along the radial axis, all showing a comparable trend to the non-forced case.

- The droplet diameter distribution of the spray also undergoes a periodic oscillation. This was quantified using the Rosin-Rammler distribution and its calculated parameters showed a distinct fluctuation.

- The mass flux and the local ALR of the spray, which are major operating characteristics for the combustor of the jet engine, strongly oscillate, underlying the importance of predicting these instabilities.

Establishing the response of the spray under low-frequency forcing, the following experimental campaign revolved around the investigation of the frequency influence on this response. The spray was studied at the four aforementioned frequencies examined with the hot-wire CTA analysis, along the radial direction. The major conclusion can be summarized in the following points:

- The fundamental spray properties, such as mean velocity, SMD, and mass flux, oscillated periodically matching each experiment's excitation frequency, similar to the case of the low-frequency investigations.

- Regardless of the excitation frequency, the average value and amplitude of their variation were comparable in all cases. This suggested that constant amplitude stimulation had no effect on the average or amplitude of the oscillation on droplet properties in the frequency range studied at the spray's centre.

- With increasing distance along the radial direction, at the two highest frequencies of 320 Hz and 416 Hz the SMD became almost unaffected by the forcing while the mass flux distribution became more uniform, indicating a change in the spray structure.

- Separating into size classes, similar to the prior experimental campaigns, in order to analyse how it is impacted by the various frequencies, the bigger droplets showed a distinct delay relative to the smaller ones as the excitation frequency increased. This was to be anticipated given their inertia.

To further support the experimental observations, the mean droplet velocity for the different size classes was also numerically computed by analysing the motion equation of a droplet in one dimension. A result that matches the experimental observations was obtained by solving the differential equation for various initial conditions and diameters. Using the resulting droplet velocity of the motion equation, the phase difference was also calculated, quantifying the lag between the larger droplets compared to the small ones for the various excitation frequencies.

Finally, the influence of the air-to-liquid ratio on the spray characteristics at the excitation frequency of 102 Hz was investigated. By varying the water mass flow rate supplied in the model atomizer, the phase-averaged mean droplet velocity, mean diameter, SMD, and spray mass flux were measured and the ALR influence on their periodic fluctuation was evident.

Summarizing the aforementioned outcomes of this study, it is evident that the spray characteristics, and especially the SMD and the spray mass flux, oscillate with a relatively high amplitude when the airflow is forced in frequencies of similar amplitude up to approximately 500 Hz. The oscillation amplitude was high in all examined cases of varying excitation frequencies, as well as the cases with varying air-to-liquid ratios.

In conclusion, the cause of the ALR oscillation cannot be declared as definitely identified. In case the liquid is accumulating at the lip of the nozzle, leading to the spray mass flux oscillation, then a shorter prefilming length would result in smaller oscillation amplitudes, since less liquid would then be able to accumulate. To further study the hypothesis of liquid accumulation at the atomizer edge or the droplet temporal separation, a CFD study would enlighten this research. In any case, the resulting response of the spray characteristics can be exploited in models of thermoacoustic phenomena using machine learning in order to predict the instabilities in the combustion chamber of a real aircraft engine. Since this response is evident on the tested frequencies, further research activities would provide a better overview of the phenomenon and a larger database for the prediction models. A comparison with other liquids, in more positions in the radial direction, as well as a variation in the mean pressure drop at a constant liquid flow rate, would provide more insight on the observations of this dissertation. For even further relevance with realistic jet engine combustor conditions, future spray investigations on a closed chamber under a high-pressure air supply would be necessary. Overall, the demand for more experimental data to validate the models that predict thermoacoustic instabilities remains essential for further research and development of jet engines for reduced emissions.

References

[1]   European Environment Agency, "European Aviation Environmental Report", 2019.

[2]   Federal Aviation Administration, "Aviation Emissions, Impacts & Mitigation. A Primer", 2015.

[3]   Olivier Penanhoat, "Low Emissions Combustor Technology Developments in the European Programmes LOPOCOTEP and TLC". 25th International Congress of the Aeronautical Sciences. Hamburg, Germany. September 3-8, 2006.

[4]   Michel Cazalens, Olivier Penanhoat, "Environmental Constraints and Appropriate R&T Strategy for Combustor Technology". 24th International Congress of the Aeronautical Sciences. Yokohama, Japan. August 29 - September 3, 2004.

[5]   H. Ritchie, M. Roser, "CO_2 and Greenhouse Gas Emissions", Our World in Data, 2020, https://ourworldindata.org/co2-and-other-greenhouse-gas-emissions.

[6]   J.E. Penner, D.H. Lister, D.J. Griggs, D.J. Dokken, M. McFarland, "Aviation and the Global Atmosphere". Intergovernmental Panel on Climate Change, 1999.

[7]   C.K. Gilmore, S.R.H. Barrett, J. Koo, Q. Wang, "Temporal and spatial variability in the aviation NOx-related O3 impact", Environmental Research Letters, 8(3), (2013), pp. 1–8, doi:10.1088/1748-9326/8/3/034027.

[8]   A.H. Lefebvre, D.R. Ballal, "Gas Turbine Combustion. Alternative Fuels and Emissions", CRC Press Taylor & Francis Group, LLC, Boca Raton, 2010.

[9]   J. Zhang, Y. Wei, Z. Fang, "Ozone Pollution: A Major Health Hazard Worldwide", Frontiers in Immunology, 10, (2019), pp. 1–10, doi:10.3389/fimmu.2019.02518.

[10]   F. Anwar, F.N. Chaudhry, S. Nazeer, N. Zaman, S. Azam, "Causes of Ozone Layer Depletion and Its Effects on Human: Review", Atmospheric and Climate Sciences, 6(1), (2016), pp. 129–134, doi:10.4236/acs.2016.61011.

[11]   Rainer Fink, "Untersuchungen zu LPP-Flugtriebwerksbrennkammern unter erhöhtem Druck", PhD Dissertation, Technische Universität München. Lehrstuhl für Flugantriebe, Munich, Germany, 2001.

[12]   Ralf v. d. Bank, Thomas Schilling, "Development of an Ultra-Low NOx LP(P) Burner". Proceedings of ASME Turbo Expo 2004. Vienna, Austria. June 14-17, 2004.

[13]   P. Gokulakrishnan, M.J. Ramotowski, G. Gaines, C. Fuller, R. Joklik, L.D. Eskin, M.S. Klassen, R.J. Roby, "A novel low NOx lean, premixed, and prevaporized combustion system for liquid fuels", Journal of Engineering for Gas Turbines and Power, 130(5), (2008), pp. 1–7, doi:10.1115/1.2904889.

[14]   T.C. Lieuwen, V. Yang, "Combustion Instabilities in Gas Turbine Engines. Operational Experience, Fundamental Mechanisms, and Modeling", American Institute of Aeronautics and Astronautics, Inc., Reston, 2005.

[15]   T. Poinsot, D. Veynante, "Theoretical and Numerical Combustion", R.T. Edwards, Inc., Philadelphia, 2001.

[16]   J.C. DeLaat, D.E. Paxson, "Characterization and simulation of the thermoacoustic instability behavior of an advanced, low emissions combustor prototype". 44th AIAA/ASME/SAE/ASEE Joint Propulsion Conference & Exhibit. Hartford, CT, USA. July 21-23, 2008.

[17]   J.C. Oefelein, V. Yang, "Comprehensive Review of Liquid-Propellant Combustion Instabilities in F-1 Engines", Journal of Propulsion and Power, 9(5), (1993), pp. 657–677, doi:10.2514/3.23674.

[18]   T. Poinsot, "Prediction and Control of Combustion Instabilities in Real Engines", Proceedings of the Combustion Institute, 36(1), (2017), pp. 1–28, doi:10.1016/j.proci.2016.05.007.

[19]   A.H. Lefebvre, "Airblast Atomization", Progress in Energy and Combustion Science, 6(3), (1980), pp. 233–261, doi:10.1016/0360-1285(80)90017-9.

[20]   J. Su, A. Barker, A. Garmory, J. Carrotte, "Spray Response to Acoustic Forcing of a Multi-Passage Lean-Burn Aero-Engine Fuel Injector". Proceedings of ASME Turbo Expo 2018. Oslo, Norway. June 11-15, 2018.

[21]   R.I. Sujith, "An Experimental Investigation of Interaction of Sprays with Acoustic Fields", Experiments in Fluids, 38(5), (2005), pp. 576–587, doi:10.1007/s00348-004-0912-1.

[22]   R.I. Sujith, G.A. Waldherr, J.I. Jagoda, B.T. Zinn, "An Experimental Investigation of the Behavior of Droplets in Axial Acoustic Fields", Journal of Vibration and Acoustics, 119(3), (1997), pp. 285–292, doi:10.1115/1.2889722.

[23]   R.I. Sujith, G.A. Waldherr, J.I. Jagoda, B.T. Zinn, "A Theoretical Investigation of the Behavior of Droplets in Axial Acoustic Fields",

Journal of Vibration and Acoustics, 121(3), (1999), pp. 286–294, doi:10.1115/1.2893978.

[24]   A. Müller, "Experimentelle Untersuchung des Zerstäubungsverhaltens luftgestützter Brennstoffdüsen bei oszillierenden Strömungen", PhD Dissertation, Karlsruhe Institute of Technology. Institut für Thermische Strömungsmaschinen, Karlsruhe, Germany, 2014.

[25]   B. Déjean, P. Berthoumieu, P. Gajan, "Experimental study on the influence of the liquid and air thicknesses on a planar air-blasted liquid sheet". 25th European Conference on Liquid Atomization and Spray Systems. Chania, Greece. September 1-4, 2013.

[26]   V.G. Fernandez, P. Berthoumie, G. Lavergne, "Liquid sheet disintegration at high pressure: An experimental approach", Combustion for aerospace propulsion, 337(6-7), (2009), pp. 481–491, doi:10.1016/j.crme.2009.06.026.

[27]   S. Gepperth, D. Guildenbecher, R. Koch, H. Bauer, "Pre-filming primary atomization: Experiments and modeling". 23rd Annual Conference on Liquid Atomization and Spray Systems. Brno, Czech Republic. September 6-9, 2010.

[28]   U. Bhayaraju, "Analysis of Liquid Sheet Breakup and Characterisation of Plane Prefilming and Nonprefilming Airblast Atomisers", PhD Dissertation, Technische Universität Darmstadt. Fachbereich Maschinenbau, Darmstadt, Germany, 2007.

[29]   G. Chaussonnet, A. Müller, S. Holz, R. Koch, H.-J. Bauer, "Time-Response of Recent Prefilming Airblast Atomization Models in an Oscillating Air Flow Field", Journal of Engineering for Gas Turbines and Power, 139(12), (2017), pp. 121501 1-9, doi:10.1115/1.4037325.

[30]   U. Sengupta, C.E. Rasmussen, M. Juniper, "Bayesian Machine Learning for the Prognosis of Combustion Instabilities from Noise". Proceedings of ASME Turbo Expo 2020. London, UK. June 22-26, 2020.

[31]   Francesco Garita, Hans Yu, Matthew P. Juniper, "Assimilation of Experimental Data to Create a Quantitatively Accurate Reduced-Order Thermoacoustic Model", Journal of Engineering for Gas Turbines and Power, 143(2), (2021), pp. 1–9, doi:10.1115/1.4048569.

[32]   M. McCartney, M. Haeringer, W. Polifke, "Comparison of Machine Learning Algorithms in the Interpolation and Extrapolation of Flame Describing Functions", Journal of Engineering for Gas Turbines and Power, 142(6), (2020), pp. 1–10, doi:10.1115/1.4045516.

[33]   G. Bonciolini, A. Faure-Beaulieu, C. Bourquard, N. Noiray, "Low order modelling of thermoacoustic instabilities and intermittency: Flame response delay and nonlinearity", Combustion and Flame, 226, (2021), pp. 396–411, doi:10.1016/j.combustflame.2020.12.034.

[34]   H. Cohen, H.I.H. Saravanamuttoo, P.V. Straznicky, G.F.C. Rogers, "Gas Turbine Theory", 5th ed., Pearson Education, Ltd, 2001.

[35]   S.L. Dixon, C.A. Hall, "Fluid Mechanics and Thermodynamics of Turbomachinery", Butterworth-Heinemann, Oxford, UK, 2014.

[36]   S.J. Moyes, "Principles of Jet Propulsion and Gas Turbines", Nature, 164(4162), (1949), pp. 202–203, doi:10.1038/164202b0.

[37]   Rolls-Royce plc, "The Jet Engine", Wiley, Chichester, 2015.

[38]   S.M. Correa, "A Review of NOx Formation Under Gas-Turbine Combustion Conditions", Combustion Science and Technology, 87(1-6), (1993), pp. 329–362, doi:10.1080/00102209208947221.

[39]   M. Blomeyer, B. Krautkremer, D.K. Hennecke, T. Doerr, "Mixing Zone Optimization of a Rich-Burn/Quick-Mix/Lean-Burn Combustor", Journal of Propulsion and Power, 15(2), (1999), pp. 288–295, doi:10.2514/2.5425.

[40]   C. Hassa, M. Carl, M. Frodermann, T. Behrendt, J. Heinze, I. Röhle, N. Brehm, T. Schilling, T. Doerr, "Experimental Investigations of an Axially Staged Combustor Sector with Optical Diagnostics at Realistic Operating Conditions". RTO AVT Symposium on Gas Turbine Engine Combustion, Emissions and Alternative Fuels. Lisbon, Portugal. October 12-16, 1998.

[41]   R. McKinney, A. Cheung, W. Sowa, D. Sepulveda, "The Pratt & Whitney TALON X Low Emissions Combustor: Revolutionary Results with Evolutionary Technology". 45th AIAA Aerospace Sciences Meeting and Exhibit. Reno, Nevada. January 8-11, 2007.

[42]   Y. Liu, X. Sun, V. Sethi, D. Nalianda, Y.-G. Li, L. Wang, "Review of Modern Low Emissions Combustion Technologies for Aero Gas Turbine Engines", Progress in Aerospace Sciences, 94, (2017), pp. 12–45, doi:10.1016/j.paerosci.2017.08.001.

[43]   N. Zarzalis, "NOx-Emissionminderung bei Flugtriebwerksbrennkammern nach dem Konzept der Fett-Mager-Verbrennung. Von der Grundlagenforschung zum industriellen Einsatz". DGLR-Jahrestagung, 1997.

[44]   A.S. Feitelberg, M.A. Lacey, "The GE Rich-Quench-Lean Gas Turbine Combustor". e International Gas Turbine & Aeroengine Congress & Exhibition. Orlando, Florida. June 2-5, 1997.

[45]   G. Poeschl, W. Ruhkamp, H. Pfost, "Combustion with Low Pollutant Emissions of Liquid Fuels in Gas Turbines by Premixing and

Prevaporization". ASME International Gas Turbine and Aeroengine Congress end Exposition. The Hague, Netherlands. June 13-16, 1994.

[46]   H.C. Mongia, "TAPS: A Fourth Generation Propulsion Combustor Technology for Low Emissions". AIAA International Air and Space Symposium and Exposition: The Next 100 Years. Dayton, Ohio, USA. July 14-17, 2003.

[47]   N. Spyra, "Entwicklung und Untersuchung eines neuartigen Brennstoffaufbereitungssystems für kleine Gasturbinen", PhD Dissertation, Technische Universität München. Lehrstuhl für Flugantriebe, Munich, Germany, 2010.

[48]   W. Lazik, T. Doerr, S. Bake, R. v. d. Bank, L. Rackwitz, "Development of Lean-Burn Low-NOx Combustion Technology at Rolls-Royce Deutschland". Proceedings of ASME Turbo Expo 2008. Berlin, Germany. June 9–13, 2008.

[49]   M. Foust, T. Doug, R. Stickles, C. Clayton, W. Dodds, "Development of the GE Aviation Low Emissions TAPS Combustor for Next Generation Aircraft Engines". 50th AIAA Aerospace Sciences Meeting including the New Horizons Forum and Aerospace Exposition. Nashville, Tennessee, USA. January 9-12, 2012.

[50]   C. Hassa, in: T.C. Lieuwen, V. Yang (Eds.), Gas Turbine Emissions, Cambridge University Press, Cambridge, 2013, pp. 237–289.

[51]   T.J. Poinsot, A.C. Trouve, D.P. Veynante, S.M. Candel, E.J. Esposito, "Vortex-Driven Acoustically Coupled Combustion Instabilities", Journal of Fluid Mechanics, 177, (1987), pp. 265–292, doi:10.1017/S0022112087000958.

[52]   S.M. Candel, "Combustion instabilities coupled by pressure waves and their active control", Symposium (International) on Combustion, 24(1), (1992), pp. 1277–1296, doi:10.1016/S0082-0784(06)80150-5.

[53]   T. Poinsot, "Simulation Methodologies and Open Questions for Acoustic Combustion Instability Studies". CTR Annual Research Briefs, 2013.

[54]   W. Krebs, P. Flohr, B. Prade, S. Hoffmann, "Thermoacoustic Stability Chart for High-Intensity Gas Turbine Combustion Systems", Combustion Science and Technology, 174(7), (2002), pp. 99–128, doi:10.1080/00102200208984089.

[55]   A.P. Dowling, "Modeling and control of combustion oscillations". Proceedings of ASME Turbo Expo 2005. Reno-Tahoe, Nevada, USA. June 6-9, 2005.

[56]   E. Truckenbrodt, "Fluidmechanik Band 2. Elementare Strömungsvorgänge dichteveränderlicher Fluide sowie Potential- und Grenzschichtströmungen", Springer, Berlin, 2008.

[57]   A.D. Pierce, "Acoustics. An Introduction to Its Physical Principles and Applications", Springer International Publishing, Cham, Switzerland, 2019.

[58]   L. Crocco, J. Grey, D.T. Harrje, "Theory of Liquid Propellant Rocket Combustion Instability and Its Experimental Verification", ARS Journal, 30(2), (1960), pp. 159–168, doi:10.2514/8.5020.

[59]   L. Rayleigh, "The Explanation of Certain Acoustical Phenomena", Nature, 18, (1878), pp. 319–321, doi:10.1038/018319a0.

[60]   H.J. Merk, "Analysis of heat-driven oscillations of gas flows", Applied Scientific Research, Section A, 6(4), (1957), pp. 317–336, doi:10.1007/BF03184653.

[61]   A. Andreini, B. Facchini, A. Giusti, F. Turrini, "Assessment of Flame Transfer Function Formulations for the Thermoacoustic Analysis of Lean Burn Aero-engine Combustors", Energy Procedia, 45, (2014), pp. 1422–1431, doi:10.1016/j.egypro.2014.01.149.

[62]   A. Fischer, "Hybride, thermoakustische Charakterisierung von Drallbrennern", PhD Dissertation, Technische Universität München. Lehrstuhl fur Thermodynamik, Munich, Germany, 2003.

[63]   D. Ronneberger, C.D. Ahrens, "Wall Shear Stress Caused by Small Amplitude Perturbations of Turbulent Boundary-Layer Flow. An Experimental Investigation", Journal of Fluid Mechanics, 83(3), (1977), pp. 433–464, doi:10.1017/S0022112077001281.

[64]   M.C. Peters, A. Hirschberg, A.J. Reijnen, A.P. Wijnands, "Damping and Reflection Coefficient Measurements for an Open Pipe at Low Mach and Low Helmholtz Numbers", Journal of Fluid Mechanics, 256, (1993), pp. 499–534, doi:10.1017/S0022112093002861.

[65]   C.O. Paschereit, B. Schuermans, W. Polifke, O. Mattson, "Measurement of Transfer Matrices and Source Terms of Premixed Flames". Proceedings of ASME Turbo Expo 1999. Indianapolis, Indiana, USA. June 7-10, 1999.

[66]   A.H. Lefebvre, V.G. Mcdonell, "Atomization and Sprays", CRC Press Taylor & Francis Group, LLC, Boca Raton, 2017.

[67]   A.H. Lefebvre, "Fuel Effects on Gas Turbine Combustion - Ignition, Stability, and Combustion Efficiency", Journal of Engineering for Gas Turbines and Power, 107(1), (1985), pp. 24–37, doi:10.1115/1.3239693.

[68]   K.K. Rink, A.H. Lefebvre, "Influence of Fuel Drop Size and Combustor Operating Conditions on Pollutant Emissions". 1986 SAE International

Fall Fuels and Lubricants Meeting and Exhibition. Philadelphia. October 6-9, 1986.

[69]   C.M. Reeves, A.H. Lefebvre, "Fuel Effects on Aircraft Combustor Emissions". Proceedings of ASME Turbo Expo 1986. Düsseldorf, West Germany. June 8-12, 1986.

[70]   G.A.E. Godsave, "Studies of the combustion of drops in a fuel spray - the burning of single drops of fuel", Symposium (International) on Combustion, 4(1), (1953), pp. 818–830, doi:10.1016/S0082-0784(53)80107-4.

[71]   M. Goldsmith, S.S. Penner, "On the Burning of Single Drops of Fuel in an Oxidizing Atmosphere", Journal of Jet Propulsion, 24(4), (1954), pp. 245–251, doi:10.2514/8.6508.

[72]   W.R. Lane, "Shatter of Drops in Streams of Air", Ind. Eng. Chem., 43(6), (1951), pp. 1312–1317.

[73]   J. Zierep, K. Bühler, "Grundzüge der Strömungslehre. Grundlagen, Statik und Dynamik der Fluide", 7th ed., B.G. Teubner Verlag, Wiesbaden, 2008.

[74]   F.M. White, "Fluid Mechanics", McGraw-Hill, Inc., New York, 2011.

[75]   J.R. Joyce, "The Atomisation of Liquid Fuels. Prof. E. Giffen and Dr. A. Muraszew. Chapman & Hall, London 1953. 246 pp. Diagrams. 36s. net", The Journal of the Royal Aeronautical Society, 58(518), (1954), pp. 146, doi:10.1017/S0368393100097832.

[76]   J.O. Hinze, "Fundamentals of the Hydrodynamic Mechanism of Splitting in Dispersion Processes", AIChE Journal, 1(3), (1955), pp. 289–295, doi:10.1002/aic.690010303.

[77]   D.G. Gordon, "Mechanism and Speed of Breakup of Drops", Journal of Applied Physics, 30(11), (1959), pp. 1759-1761.

[78]   C. Weber, "Zum Zerfall eines Flussigkeitsstrahles", Journal of Applied Mathematics and Mechanics, 11(2), (1931), pp. 136–154, doi:10.1002/zamm.19310110207.

[79]   A.A. Rizkalla, "The Influence of Air and Liquid Properties on Airblast Atomization", PhD Dissertation, Cranfield Institute of Technology. School of Mechanical Engineering, Cranfield, UK, 1974.

[80]   W.V. Ohnesorge, "The Formation of Drops by Nozzles and the Breakup of Liquid Jets", Journal of Applied Mathematics and Mechanics, 16(6), (1936), pp. 355–358, doi:10.1002/zamm.19360160611.

[81]   G.H. McKinley, M. Renardy, "Wolfgang von Ohnesorge", Physics of Fluids, 23(12), (2011), pp. 1–17, doi:10.1063/1.3663616.

[82]   L.-P. Hsiang, G.M. Faeth, "Drop Deformation and Breakup due to Shock Wave and Steady Disturbances", International Journal of Multiphase Flow, 21(4), (1995), pp. 545–560, doi:10.1016/0301-9322(94)00095-2.

[83]   M. Pilch, C.A. Erdman, "Use of Breakup Time Data and Velocity History Data to Predict the Maximum Size of Stable Fragments for Acceleration-Induced Breakup of a Liquid Drop", International Journal of Multiphase Flow, 13(6), (1987), pp. 741–757, doi:10.1016/0301-9322(87)90063-2.

[84]   R.D. Reitz, "Atomization and Other Breakup Regimes of a Liquid Jet", PhD Dissertation, Princeton University, Princeton, USA, 1978.

[85]   R.D. Reitz, F.V. Bracco, "Mechanism of Atomization of a Liquid Jet", Physics of Fluids, 25(10), (1982), pp. 1730–1742, doi:10.1063/1.863650.

[86]   G. Wozniak, "Zerstäubungstechnik. Prinzipien, Verfahren, Geräte", Springer-Verlag, Berlin, 2003.

[87]   S.P. Lin, Z.W. Lian, "Mechanisms of the Breakup of Liquid Jets", AIAA Journal, 28(1), (1990), pp. 120–126, doi:10.2514/3.10361.

[88]   L. Rayleigh, "On the instability of jets", Proceedings of the London Mathematical Society, s1-10(1), (1878), pp. 4–13, doi:10.1112/plms/s1-10.1.4.

[89]   N. Dombrowski, W.R. Johns, "The Aerodynamic Instability and Disintegration of Viscous Liquid Sheets", Chemical Engineering Science, 18(3), (1963), pp. 203–214, doi:10.1016/0009-2509(63)85005-8.

[90]   R.H. Rangel, W.A. Sirignano, "The Linear and Nonlinear Shear Instability of a Fluid Sheet", Physics of Fluids A: Fluid Dynamics, 3(10), (1991), pp. 2392–2400, doi:10.1063/1.858177.

[91]   C. Mehring, W.A. Sirignano, "Capillary Stability of Modulated Swirling Liquid Sheets", Atomization and Sprays, 14(5), (2004), doi:10.1615/AtomizSpr.v14.i5.10.

[92]   Q. Xue, M. Battistoni, C.F. Powell, D.E. Longman, S.P. Quan, E. Pomraning, P.K. Senecal, D.P. Schmidt, S. Som, "An Eulerian CFD Model and X-Ray Radiography for Coupled Nozzle Flow and Spray in Internal Combustion Engines", International Journal of Multiphase Flow, 70, (2015), pp. 77–88, doi:10.1016/j.ijmultiphaseflow.2014.11.012.

[93]   W.W. Hagerty, J.F. Shea, "A Study of the Stability of Plane Fluid Sheets", Journal of Applied Mechanics, 22(4), (1955), pp. 509–514, doi:10.1115/1.4011145.

[94]   L. Qin, R. Yi, L. Yang, "Theoretical breakup model in the planar liquid sheets exposed to high-speed gas and droplet size prediction",

International Journal of Multiphase Flow**,** 98, (2018), pp. 158–167, doi:10.1016/j.ijmultiphaseflow.2017.09.010.

[95]   N. Dombrowski, R.P. Fraser, "A Photographic Investigation into the Disintegration of Liquid Sheets", Philosophical Transactions of the Royal Society of London. Series A, Mathematical and Physical Sciences**,** 247(924), (1954), pp. 101–130, doi:10.1098/rsta.1954.0014.

[96]   G.D. Crapper, N. Dombrowski, W.P. Jepson, G.A.D. Pyott, "A Note on the Growth of Kelvin-Helmholtz Waves on Thin Liquid Sheets", Journal of Fluid Mechanics**,** 57(4), (1973), pp. 671–672, doi:10.1017/S0022112073001941.

[97]   G.D. Crapper, N. Dombrowski, "A Note on the Effect of Forced Disturbances on the Stability of Thin Liquid Sheets and on the Resulting Drop Size", International Journal of Multiphase Flow**,** 10(6), (1984), pp. 731–736, doi:10.1016/0301-9322(84)90009-0.

[98]   T. Arai, H. Hashimoto, "Behavior of Gas-Liquid Interface on a Liquid Film Jet. Instability of a Liquid Film Jet in a Co-Current Gas Stream", Bulletin of JSME**,** 28(245), (1985), pp. 2652–2659, doi:10.1299/jsme1958.28.2652.

[99]   P. Berthoumieu, G. Lavergne, "Video Techniques Applied to the Characterization of Liquid Sheet Breakup", Journal of Visualization**,** 4(3), (2001), pp. 267–275, doi:10.1007/BF03182587.

[100]   B.E. Stapper, G.S. Samuelsen, "An Experimental Study of the Breakup of a Two-Dimensional Liquid Sheet in the Presence of Co-Flow Air Shear". 28th Aerospace Sciences Meeting. Reno, NV, U.S.A. January 8-11, 1990.

[101]   L. Bayvel, Z. Orzechowski, "Liquid Atomization", Taylor & Francis, Boca Raton, 2013.

[102] N.K. Rizk, A.H. Lefebvre, "The Influence of Liquid Film Thickness on Airblast Atomization", Journal of Engineering for Gas Turbines and Power, 102(3), (1980), pp. 706–710, doi:10.1115/1.3230329.

[103] S. Gepperth, A. Müller, R. Koch, H. Bauer, "Ligament and Droplet Characteristics in Prefilming Airblast Atomization". 12th Triennial International Conference on Liquid Atomization and Spray Systems. Heidelberg, Germany. September 2-6, 2012.

[104] H.H. Chiu, "Advances and Challenges in Droplet and Spray Combustion. I. Toward a Unified Theory of Droplet Aerothermochemistry", Progress in Energy and Combustion Science, 26(4-6), (2000), pp. 381–416, doi:10.1016/S0360-1285(00)00016-2.

[105] G.M. Faeth, "Evaporation and Combustion of Sprays", Progress in Energy and Combustion Science, 9(1-2), (1983), pp. 1–76, doi:10.1016/0360-1285(83)90005-9.

[106] G.M. Faeth, "Mixing, Transport and Combustion in Sprays", Progress in Energy and Combustion Science, 13(4), (1987), pp. 293–345, doi:10.1016/0360-1285(87)90002-5.

[107] E. Babinsky, P.E. Sojka, "Modeling Drop Size Distributions", Progress in Energy and Combustion Science, 28(4), (2002), pp. 303–329, doi:10.1016/S0360-1285(02)00004-7.

[108] R.A. Mugele, H.D. Evans, "Droplet Size Distribution in Sprays", Industrial & Engineering Chemistry, 43(6), (1951), pp. 1317–1324, doi:10.1021/ie50498a023.

[109] H. Liu, "Science and Engineering of Droplets. Fundamentals and Applications", William Andrew Inc., 1999.

[110] J. Sauter, "Die Grössenbestimmung der im Gemischnebel von Verbrennungskraftmaschinen vorhandenen Brennstoffteilchen", VDI-Verlag, Berlin, 1926.

[111] M. Alderliesten, "Mean Particle Diameters. From Statistical Definition to Physical Understanding", PhD Dissertation, Delft University of Technology. Faculty of Applied Sciences, Delft, Netherlands, 2008.

[112] E. Giffen, A. Muraszew, "The Atomization of Liquid Fuels", Chapman & Hall, New York, 1953.

[113] D.Y.F.K.L.A.Y.V.I. Borodin V. A., "Atomization of Liquids", Defense Technical Information Center, Moscow, 1967.

[114] N. Ashgriz, "Handbook of Atomization and Sprays. Theory and Applications", Springer Science+Business Media, LLC, Boston, 2011.

[115] G.E. Lorenzetto, A.H. Lefebvre, "Measurements of Drop Size on a Plain-Jet Airblast Atomizer", AIAA Journal, 15(7), (1977), pp. 1006–1010, doi:10.2514/3.60742.

[116] N.K. Rizk, A.H. Lefebvre, "Influence of Atomizer Design Features on Mean Drop Aize", AIAA Journal, 21(8), (1983), pp. 1139–1142, doi:10.2514/3.8217.

[117] T. Inamura, M. Shirota, M. Tsushima, M. Kato, S. Hamajima, A. Sato, "Spray Characteristics of Prefiling Type of Airblast Atomizer". 12th Triennial International Conference on Liquid Atomization and Spray Systems. Heidelberg, Germany. September 2-6, 2012.

[118] G. Chaussonnet, E. Riber, O. Vermorel, B. Cuenot, S. Gepperth, R. Koch, "Large Eddy Simulation of a prefiling airblast atomizer". 25th European Conference on Liquid Atomization and Spray Systems. Chania, Greece. September 1-4, September 1-4.

[119] J.M. Cohen, T.J. Rosfjord, "Influences on the Sprays Formed by High-Shear Fuel Nozzle/Swirler Assemblies", Journal of Propulsion and Power, 9(1), (1993), pp. 16–27, doi:10.2514/3.51351.

[120] M. Budakli, T. Gambaryan-Roisman, P. Stephan, "Influence of Surface Topography on Heat Transfer in Shear-Driven Liquid Films", Journal of Physics: Conference Series, 395(1), (2012), pp. 1–9, doi:10.1088/1742-6596/395/1/012164.

[121] A.H. Lefebvre, D.C. Miller, "The Development of an Air Blast Atomizer for Gas Turbine Application", College of Aeronautics Report, (1966).

[122] A.A. Rizkalla, A.H. Lefebvre, "The Influence of Air and Liquid Properties on Airblast Atoiization", Journal of Fluids Engineering, 97(3), (1975), pp. 316–320, doi:10.1115/1.3447309.

[123] L. Qian, J. Lin, H. Xiong, T. Leung Chan, "Theoretical Investigation of the Influence of Liquid Physical Properties on Effervescent Atomization Performance", Journal of Fluids Engineering, 133, (2011), pp. 101205 1-11, doi:10.1115/1.4004256.

[124] T. Christou, B. Stelzner, N. Zarzalis, "Influence of an Oscillating Airflow on the Prefilming Airblast Atomization Process", Atomization and Sprays, 31(3), (2021), pp. 1–14, doi:10.1615/AtomizSpr.2021034553.

[125] J. Eckstein, E. Freitag, C. Hirsch, T. Sattelmayer, R. von der Bank, T. Schilling, "Forced Low-Frequency Spray Characteristics of a Generic Airblast Swirl Diffusion Burner", Journal of Engineering for Gas Turbines and Power, 127(2), (2005), pp. 301–306, doi:10.1115/1.1789515.

[126] J. Eckstein, "On the Mechanisms of Combustion Driven Low-Frequency Oscillations in Aero-Engines", PhD Dissertation, Technische Universität München. Lehrstuhl fur Thermodynamik, Munich, Germany, 2004.

[127] A.P. Dowling, S.R. Stow, "Acoustic Analysis of Gas Turbine Combustors", Journal of Propulsion and Power, 19(5), (2003), doi:10.2514/2.6192.

[128] M.R. Bothien, N. Noiray, B. Schuermans, "A Novel Damping Device for Broadband Attenuation of Low-Frequency Combustion Pulsations in Gas Turbines", Journal of Engineering for Gas Turbines and Power, 136(4), (2014), doi:10.1115/1.4025761.

[129] H.H. Bruun, "Hot-Wire Anemometry: Principles and Signal Analysis", Measurement Science and Technology, 7(10), (1996), doi:10.1088/0957-0233/7/10/024.

[130] E.O. Doebelin, "Measurement Systems. Application and Design", McGraw-Hill, Inc., USA, 1990.

[131] L.V. King, "On the convection of heat from small cylinders in a stream of fluid. Determination of the convection constants of small platinum wires, with applications to hot-wire anemometry", Proceedings of the Royal Society, 90(622), (1914), pp. 563–570, doi:10.1098/rspa.1914.0089.

[132] X. Grandchamp, Y. Fujiso, B. Wu, A. van Hirtum, "Steady Laminar Axisymmetrical Nozzle Flow at Moderate Reynolds Numbers: Modeling and Experiment", Journal of Fluids Engineering, 134, (2012), pp. 1–13, doi:10.1115/1.4005690.

[133] T. Morel, "Comprehensive Design of Axisymmetric Wind Tunnel Contractions", Journal of Fluids Engineering, 97, (1975), pp. 225–233.

[134] Philip J. Pritchard, John C. Leylegian, Robert Were Fox, A. T. Mcdonald, "Fox and McDonald's Introduction to Fluid Mechanics", Wiley, New Jersey, 2011.

[135] TSI Inc., "IFA 300 Constant Temperature Anemometer System Operation Manual", TSI Incorporated, USA, 2015.

[136] T. Butz, "Fouriertransformation für Fußgänger", 7th ed., Vieweg+Teubner Verlag, Leipzig, 2011.

[137] E.O. Brigham, "The Fast Fourier Transform And Its Applications", Prentice-Hall, Inc., New Jersey, 1988.

[138] S.M. Kuo, B.H. Lee, "Real Time Digital Signal Processing", John Wiley & Sons, Ltd, Chichester, UK, 2001.

[139] F. Durst, M. Zaré, "Laser-Doppler Measurements in Two-Phase Flows". Proceedings of the LDA-Symposium. Copenhagen, Denmark. August 25-28, 1975.

[140] B. Ruck, "Laser-Doppler-Anemometrie", AT-Fachverlag GmbH, Stuttgart, 1987.

[141] H.-E. Albrecht, M. Borys, N. Damaschke, C. Tropea, "Laser Doppler and Phase Doppler Measurement Techniques", Springer-Verlag, Berlin, 2003.

[142] H.A. Radi, J.O. Rasmussen, "Principles of Physics. For Scientists and Engineers", Springer-Verlag, Berlin, 2013.

[143] M. Saffman, "Automatic calibration of LDA measurement volume size", Applied Optics, 26(13), (1987), pp. 2592–2597, doi:10.1364/ao.26.002592.

[144] R. Hooke, "Of a New Property in the Air". Micrographia, Observation LVIII. London, 1665.

[145] G.S. Settles, "Schlieren and Shadowgraph Techniques. Visualizing Phenomena in Transparent Media", Springer Science+Business Media, Berlin, Heidelberg, 2001.

[146] LaVision GmbH, "ParticleMaster Shadow. Product Manual", Göttingen, 2017.

[147] N. Otsu, "A Threshold Selection Method from Gray-Level Histograms", IEEE Transactions on Systems, Man, and Cybernetics, 9(1), (1979), pp. 62–66, doi:10.1109/TSMC.1979.4310076.

[148] Q. Cao, L. Qingge, P. Yang, H. Lv, "Performance Analysis of Otsu-Based Thresholding Algorithms: A Comparative Study", Journal of Sensors, 2021, (2021), pp. 1–14, doi:10.1155/2021/4896853.

[149] M. Raffel, C.E. Willert, S.T. Wereley, J. Kompenhans, "Particle Image Velocimetry. A Practical Guide", 2nd ed., Springer, Berlin, 2007.

[150] Dantec Dynamics, "BSA Flow Software. User Guide", Dantec Dynamics A/S, 2016.

[151] E. Bechhoefer, M. Kinglsey, "A Review of Time Synchronous Average Algorithms". Annual Conference of the Prognostics and Health Management Society. San Diego. September 27 - October 10, 2009.

[152] P. Wernert, D. Favier, "Considerations about the phase averaging method with application to ELDV and PIV measurements over pitching airfoils", Experiments in Fluids, 27(6), (1999), pp. 473–483, doi:10.1007/s003480050372.

[153] F. Ostermann, R. Woszidlo, S. Gaertlein, C. Nayeri, C.O. Paschereit, "Phase-Averaging Methods for a Naturally Oscillating Flow Field". 52nd Aerospace Sciences Meeting. National Harbor, Maryland. January 13-17, 2014.

[154] A. Kumar, S. Sahu, "Optical Visualization of Liquid Jet in the Presence of Swirling Air", Journal of Flow Visualization & Image Processing, 25(3-4), (2018), pp. 229–244, doi:10.1615/JFlowVisImageProc.2018027766.

[155] E. Rostami, H. Mahdavy Moghaddam, "The Velocity and Viscosity Impact on the Annular Spray Atomisation of Different Fuels", Combustion Theory and Modelling, 25(1), (2021), pp. 158–192, doi:10.1080/13647830.2020.1845399.

[156] B. Befrui, M. D'Onofrio, L.E. Markle, P. Spiekermann, "Coupled LES Jet Primary Breakup - Lagrangian Spray Simulation of a GDi Multi-Hole Fuel Injector", SAE International Journal of Fuels and Lubricants, 8(1), (2015), pp. 179–189, doi:10.4271/2015-01-0943.

[157] A.H. Lefebvre, M.S. El-Shanawany, "Airblast Atomization. Effect of Linear Scale on Mean Drop Size", Journal of Energy, 4(6), (1980), pp. 184-189, doi:10.2514/3.62472.

[158] S.K. Soni, P.S. Kolhe, "Liquid Jet Breakup and Spray Formation with Annular Swirl Air", International Journal of Multiphase Flow, 134, (2021), pp. 103474, doi:10.1016/j.ijmultiphaseflow.2020.103474.

[159] G. Charalampous, C. Hadjiyiannis, Y. Hardalupas, "Comparative Measurement of the Breakup Length of Liquid Jets in Airblast Atomisers Using Optical Connectivity, Electrical Connectivity and Shadowgraphy", Measurement, 89, (2016), pp. 288–299, doi:10.1016/j.measurement.2016.03.062.

[160] J. Chahed, V. Roig, L. Masbernat, "Eulerian–Eulerian Two-Fluid Model for Turbulent Gas–Liquid Bubbly Flows", International Journal of Multiphase Flow, 29(1), (2003), pp. 23–49, doi:10.1016/S0301-9322(02)00123-4.

186

[161] M. Wörner, "A Compact Introduction to the Numerical Modeling of Multiphase Flows", Karlsruhe, 2003.

[162] Y. Liu, "Two-Fluid Modeling of Gas-Solid and Gas-Liquid Flows. Solver Development and Application", PhD Dissertation, Technische Universität München. Lehrstuhl I fur Technische Chemie, Munich, Germany, 2014.

[163] C. Tropea, "Optical Particle Characterization in Flows", Annual Review of Fluid Mechanics, 43(1), (2011), pp. 399–426, doi:10.1146/annurev-fluid-122109-160721.

[164] S. Gepperth, "Experimentelle Untersuchung des Primärzerfalls an generischen luftgestützten Zerstäubern unter Hochdruckbedingungen", Master Thesis, Karlsruher Institut für Technologie (KIT). Institut für Thermische Strömungsmaschinen (ITS), Karlsruhe, 2019.

[165] S. Hoffmann, S. Holz, R. Koch, H.-J. Bauer, "Euler–Lagrangian Simulation of the Fuel Spray of a Planar Prefilming Airblast Atomizer", CEAS Aeronautical Journal, 12(2), (2021), pp. 245–259, doi:10.1007/s13272-021-00493-y.

[166] G. Chaussonnet, "Modeling of Liquid Film and Breakup Phenomena in Large-Eddy Simulations of Aeroengines Fueled by Airblast Atomizers", PhD Dissertation, Université de Toulouse. Institut National Polytechnique de Toulouse (INP), Toulouse, France, 2014.

[167] D.C. Montgomery, G.C. Runger, "Applied statistics and probability for engineers", 3rd ed., Wiley, New York, 2003.

[168] B. Efron, R.J. Tibshirani, "An Introduction to the Bootstrap", Springer Science+Business Media, Dordrecht, 1993.

[169] G. Chaussonnet, S. Gepperth, S. Holz, R. Koch, H.-J. Bauer, "Influence of the Ambient Pressure on the Liquid Accumulation and on the

Primary Spray in Prefilming Airblast Atomization", International Journal of Multiphase Flow, 125(1), (2020), doi:10.1016/j.ijmultiphaseflow.2020.103229.

[170] L.R. Collins, A. Keswani, "Reynolds number scaling of particle clustering in turbulent aerosols", New Journal of Physics, 6(119), (2004), pp. 1-17, doi:10.1088/1367-2630/6/1/119.

[171] T.C.W. Lau, G.J. Nathan, "The Effect of Stokes Number on Particle Velocity and Concentration Distributions in a Well-Characterised, Turbulent, Co-Flowing Two-Phase Jet", Journal of Fluid Mechanics, 809, (2016), pp. 72–110, doi:10.1017/jfm.2016.666.

[172] M. Roudini, G. Wozniak, "Investigation of the Secondary Atomization in Prefilming Air-Blast Atomizers", International Journal of Chemical Engineering and Applications, 10(5), (2019), pp. 138–143, doi:10.18178/ijcea.2019.10.5.757.

[173] H.-H. Qiu, M. Sommerfeld, "A Reliable Method for Determining the Measurement Volume Size and Particle Mass Fluxes using Phase-Doppler Anemometry", Experiments in Fluids, 13(6), (1992), pp. 393–404, doi:10.1007/bf00223247.

[174] T. Christou, B. Stelzner, N. Zarzalis, "Influence of Acoustically Excited Airflows on a Planar Airblast Prefilmer". Proceedings of ASME Turbo Expo 2021. Virtual, Online. June 7-11, 2021.

[175] J.E. Temme, P.M. Allison, J.F. Driscoll, "Combustion instability of a lean premixed prevaporized gas turbine combustor studied using phase-averaged PIV", Combustion and Flame, 161(4), (2014), pp. 958–970, doi:10.1016/j.combustflame.2013.09.021.

[176] A. Müller, R. Koch, H.-J. Bauer, M. Hehle, O. Schafer, "Performance of Prefilming Airblast Atomizers in Unsteady Flow Conditions".

Proceedings of ASME Turbo Expo 2006. Barcelona, Spain. May 8-11, 2006.

[177] T. Christou, B. Stelzner, N. Zarzalis, "Spray Response on a Model Prefilmer under Unsteady Airflows of Various Frequencies", International Journal of Spray and Combustion Dynamics, (2022), pp. 1-9, doi:10.1177/17568277221092987.

[178] T. Sattelmayer, "Influence of the Combustor Aerodynamics on Combustion Instabilities From Equivalence Ratio Fluctuations", Journal of Engineering for Gas Turbines and Power, 125(1), (2003), pp. 11–19, doi:10.1115/1.1365159.

[179] T.C. Lieuwen, B.T. Zinn, "The Role of Equivalence Ratio Oscillations in Driving Combustion Instabilities in Low NOx Gas Turbines", Symposium (International) on Combustion, 27(2), (1998), pp. 1809–1816, doi:10.1016/S0082-0784(98)80022-2.

[180] J. Achury, W. Polifke, "Theoretical Investigation of the Particle Response to an Acoustic Field", International Journal of Spray and Combustion Dynamics, 8(4), (2016), pp. 262–270, doi:10.1177/1756827716641118.

[181] J. Almedeij, "Drag Coefficient of Flow Around a Sphere: Matching Asymptotically the Wide Trend", Powder Technology, 186(3), (2008), pp. 218–223, doi:10.1016/j.powtec.2007.12.006.

[182] M. Roudini, G. Wozniak, "Experimental Investigation of Spray Characteristics of Pre-filming Air-blast Atomizers", Journal of Applied Fluid Mechanics, 11(6), (2018), pp. 1455–1469, doi:10.29252/jafm.11.06.28115.

[183] M. Roudini, "Experimentelle Untersuchung der Sprüheigenschaften von Prefilming-Airblast-Zerstäubern", PhD Dissertation, Technische

Universität Chemnitz. Fakultät für Maschinenbau, Chemnitz, Germany, 2019.

A   Algorithm for Spray Mass Flux Calculation

A particle trajectory is shown in Figure 3.25(a) as an example. With the assumption that only signals of a sufficient burst length above the threshold (L_{min}) are accepted, the effective measurement volume diameter d_e can be defined. Burst length validation therefore rejects signals that have not traversed this minimum measurement volume length. The length for the i-th particle is determined as:

$$L_i = \Delta t \cdot \sqrt{u^2 + v^2}$$

(A.1)

where u and v are the measured velocity components of the drop and Δt is the transient time measured by the PDA processor. The effective measurement volume diameter can be therefore calculated as follows:

$$d_e = \sqrt{\frac{3}{2} L_i^2}$$

(A.2)

where N is the number of all measured particles. Depending on the trajectory of each droplet, the angle γ is considered. If:

$$\tan \gamma_i = \frac{u}{v} = 0$$

(A.3)

then the cross-sectional areas for each particle are calculated as:

$$A_z = d_e \frac{L_S}{\sin \varphi} \tag{A.4}$$

$$A_y = d_e \frac{L_S}{\sin \varphi} + \frac{\pi}{4} d_e \cot \varphi \tag{A.5}$$

In any other case, the cross-sectional areas would be:

$$A_z = d_e \frac{L_S}{\sin \varphi \cdot \cos \gamma} \tag{A.6}$$

$$A_y = d_e \frac{L_S}{\sin \varphi \cdot \sin \gamma} + \frac{\pi}{4} \frac{d_e^2}{\sin^2 \gamma} \cot \varphi \tag{A.7}$$

Finally, the volume flux is calculated:

$$\dot{V}_z'' = \frac{\pi}{6 \Delta t} \sum_{i=1}^{N} \frac{d_i^3}{A_z} \tag{A.8}$$

$$\dot{V}_y'' = \frac{\pi}{6 \Delta t} \sum_{i=1}^{N} \frac{d_i^3}{A_y} \tag{A.9}$$

Including the density, the mass flux becomes:

$$\dot{m}_z'' = \rho_p \frac{\pi}{6 \Delta t} \sum_{i=1}^{N} \frac{d_i^3}{A_z} \tag{A.10}$$

$$\dot{m}_y'' = \rho_p \frac{\pi}{6 \Delta t} \sum_{i=1}^{N} \frac{d_i^3}{A_y} \tag{A.11}$$

B   DPSS Laser Configuration

As mentioned in section 3.3.3, a 2D Fiber PDA setup was utilized for carrying out the current investigation. For this, a DPSS laser was employed with a green (532 nm) and a yellow (561 nm) set of beams. The maximum power output for each of the laser beams was 150 mW.

For the laser beams to reach the sending optic and eventually form the measurement volume as described in section 3.3.1, they undergo a complex course. Entering the transmitter box, the laser beam crosses the bragg cell and a beam splitter, where the beams are separated and a shift of 40 MHz is imposed on half of them. Via a configuration of mirrors, the beams then get reflected and reach the manipulators attached on the transmitter box, an arrangement with more internal adjustable mirrors to guide the laser properly at the output. An optical fiber serves as a medium for the four now laser beams to travel from the transmitter box to the sending optic. There, a set of lenses guide the four laser beams in the proper direction in order to properly form an intersection volume (Figure 3.23).

This configuration is illustrated in Figure B.1. Naturally, through all these reflections on the various mirrors and the trajectory of the beams through the optical fiber and the lenses, a power loss is inevitable. However, the power of the laser beams at the exit of the sending optic can be optimized, by minimizing these losses.
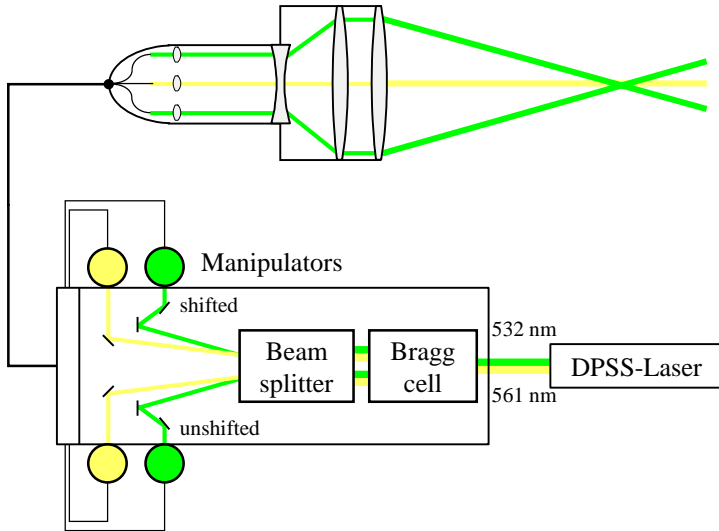
Figure B.1: Laser and sending optic configuration.

For this purpose, a laser power meter (COHERENT FieldMaxII-TOP^{TM}) was employed to measure the power of each laser beam at the output of the sending optic and namely at the measurement volume where all four beams meet. By adjusting the mirrors inside the manipulators using control screws, the output power measured with the power meter was optimized for each of the four beams. Figure B.2 shows the output power measured with the meter for various input power values at the source. The procedure was carefully accomplished so that the shifted and unshifted beams of each colour have approximately the same power at the measurement point.
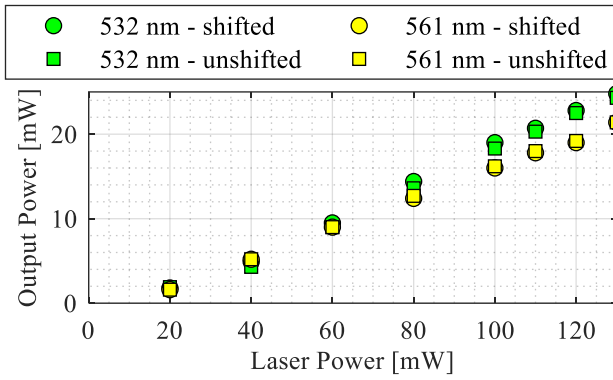
Figure B.2: Measured laser power output at the beam intersection.

C   PDA System Data

Table 9: PDA system data.

Property	Laser 1	Laser 2	Units
Wavelength	532	561	Nm
Focal length	500	500	mm
Beam diameter	2.2	2.2	mm
Expander ratio	1	1	-
Beam spacing	58	58	mm
Frequency shift	40	40	MHz
Number of fringes	33	33	-
Fringe spacing	4.594	4.844	µm
Beam half-angle	3.319	3.319	°
Measurement volume dx	2.659	2.804	mm
Measurement volume dy	0.1539	0.1623	mm
Measurement volume dz	0.1542	0.1626	mm
Receiver type	Fiber PDA	Fiber PDA	
Scattering angle	30	30	°
Receiver focal length	500	500	mm
Receiver expander ratio	1	1	-
Fringe direction	Negative	Negative	
Scattering mode	Refraction	Refraction	
Phase ratio validation	15	15	%
Phase factor P12	2.212	2.212	° µm^{-1}
Phase factor P13	0.8679	0.8679	° µm^{-1}
Eff. spatial filter width	400	400	µm

D   Siren Motor Operation Data

Table 10: Operation data of the 6SM 37S-6000 motor.

Property		Units
Ambient temperature	5…+40	°C
Permissible humidity	85	%
Operating voltage	24	V
Standstill torque	0.5	Nm
Standstill current	0.8	A
Motor pole number	6	-
Resolver pole number	2	-
Rated speed	6,000	RPM
Rated power	0.25	kW
Rated torque	0.4	Nm
Rotational speed range	10 - 8,000	RPM